

JAERI-M

8 1 3 8

STUDY OF ANALYTICAL METHOD FOR SODIUM VOID
REACTIVITY IN FAST CRITICAL ASSEMBLIES

January 1979

Masayuki NAKAGAWA

この報告書は、日本原子力研究所が JAERI-M レポートとして、不定期に刊行している研究報告書です。入手、複製などのお問い合わせは、日本原子力研究所技術情報部（茨城県那珂郡東海村）あて、お申しこしてください。

JAERI-M reports, issued irregularly, describe the results of research works carried out in JAERI. Inquiries about the availability of reports and their reproduction should be addressed to Division of Technical Information, Japan Atomic Energy Research Institute, Tokai-mura, Naka-gun, Ibaraki-ken, Japan.

Study of Analytical Method for Sodium Void Reactivity
in Fast Critical Assemblies

Masayuki NAKAGAWA

Division of Reactor Engineering, Tokai Research Establishment

JAERI

(Received January 31, 1979)

Calculational methods have been developed to analyze neutronics parameters of fast critical assemblies with heterogeneous arrangements of cells. These methods have been applied to analysis of sodium void experiments. The analysis was first made using the broad group constant set. For the heterogeneity calculations, SLAROM code has been developed. The integral transport equations are solved for a unit cell by the collision probability method. On the other hand, the fine group spectrum and multi-group cross section calculation code ESELEM 5 has been developed to examine adequacy of the broad group constant method and also to make detailed analysis. To solve the integral transport equations in a fine group structure, effective methods have been contrived and incorporated in the code. Sodium void reactivity worths were calculated on the basis of the first order and the exact perturbation theory. Calculations of the sodium void reactivity worths and the related neutronics parameters were made for FCAV-1, MZA, MZB, ZPPR-2 and ZPPR-3 assemblies, using the JAERI Fast sets. The JAERI Fast version 2 set is found to give better agreement with the measurements than the other versions, especially for the core center. Calculations show that the heterogeneity effect and the neutron streaming effect significantly influence the sodium void worths in plate environment. The deviations of the worth from measurement are nearly same in the respective assemblies. For ZPPR-3, the three-dimensional calculations were made to treat the real complex configuration with control rods and control rod positions, i.e. to examine how CR and CRP influence the sodium void worth in their neighbouring regions. The fine group method has been used for the analysis of MZA and ZPPR-2 assemblies.

This method was shown to give 10% - 20% more positive worths than the broad group method. The sample worth distribution of sodium, central reactivity worths and neutron spectrum in ZPPR-2 were calculated and compared with the measurements. The discrepancies between the fine group and the broad group methods could be made clear. The self-shielding factors of elastic removal cross sections of light and medium nuclei in the broad group set have been investigated and improved in accuracy within the concept of the conventional set. The set thus revised predicts the neutronics parameters with higher accuracy than the conventional set.

Keywords : Sodium Void Reactivity, Fast Critical Assembly, Heterogeneity, Collision Probability Method, Group Constant Set, Fine Group Spectrum, Neutron Streaming Effect, Exact Perturbation Method, Recurrence Formula, Elastic Removal Cross Section, Computer Calculation

臨界集合体におけるナトリウムボイド反応度の
解析法の研究

日本原子力研究所東海研究所原子炉工学部

中 川 正 幸

(1979年1月31日受理)

非均質格子から構成される高速臨界集合体の核的パラメータを計算する手法を開発し、ナトリウムボイド実験の解析に応用した。まず解析は、群定数セットを用いて行ったが、このために SLAROM コードを作成した。一方、詳細群スペクトルと多群実効断面積の計算のため、ESELEM5を作成し、群定数法の妥当性を検討すると共に、詳細解析に用いた。本コードは、詳細群で積分型輸送方程式を解くために種々の工夫がなされ、取り入れられている。

ナトリウムボイド反応度及び他の核的パラメータの計算を、FCAV-1, MZA, MZB, ZPPR-2 及び ZPPR-3 の炉心に対し、JAERI Fast セットを用いて行った。その結果 JAERI Fast セット第2版が最もよく実験と一致することが分った。特に、炉心中心での実験と計算の一致は良い。また非均質効果と、中性子ストリーミング効果は、平板系では、ナトリウムボイド反応度に重要な影響を与えることがわかった。実験からのずれは、各集合体共にほぼ一定である。ZPPR-3 集合体は、制御棒等を含む複雑な体系なので三次元計算を行い、制御棒等がナトリウムボイド反応度に与える効果について検討した。

詳細群法による解析を、MZAとZPPR-2 集合体について行ったが、その結果群定数による場合よりも10~20パーセント正の反応度を与えることがわかった。その他ナトリウムのサンプル反応度分布や、中心反応度値、中性子スペクトル等の解析も行った。そして群定数セットの精度について検討した。

また、中重核種の弾性除去断面積に対する遮蔽因子の精度を検討し改良する方法を示した。そしてこの結果を取り入れたセットが、従来のセットより精度よく核的パラメータを予測することを示めた。

TABLE OF CONTENTS

1. Introduction	1
2. Analytical Method of Heterogeneous System with Use of Integral Transport Solution by Collision Probability Method	9
2.1 Introduction	9
2.2 Multi-group Integral Transport Equation	11
2.3 Solution by Collision Probability Method	17
2.4 Effective Cross Sections for Cell Calculations	26
2.5 Brief Description of SLAROM Code	30
3. Multi-group Cross Section Generation Method by Using Fine Group Fundamental Mode Spectrum in Slab Cell	32
3.1 Introduction	32
3.2 Recurrence Formula for Slowing Down Equation	36
3.3 Nuclear Data Treatment	46
4. Analysis of Sodium Void Reactivity Measurements in Fast Critical Assemblies with Broad Group Constant Sets	50
4.1 Analysis of FCA V-1 Assembly	50
4.1.1 Introduction	50
4.1.2 Summary of Measurements	52
4.1.3 Calculational Methods	52
4.1.4 Results and Discussions	56
4.1.5 Concluding Remarks	61
4.2 Analysis of MZA and MZB Assemblies	70
4.2.1 Description of Assemblies	70
4.2.2 Method of Analysis	71
4.2.3 Results and Discussions on MZA	73
4.2.4 Neutron Cross Section Evaluation of Sodium	74

4.2.5	Results and Discussions on MZB	75
4.3	Analysis of ZPPR-2 and ZPPR-3 Assemblies	94
4.3.1	Description of Assemblies and Void Configurations	94
4.3.2	Methods of Analysis	96
4.3.3	Results and Discussions on ZPPR-2	98
4.3.4	Results and Discussions on ZPPR-3	100
4.4	Calculation of Sodium Void Worth Distribution in Proto-Type Fast Breeder Reactor	126
4.4.1	Calculational Method and Model	126
4.4.2	Void Worth Distribution and Maximum Worth	127
4.4.3	Comparison between Results by Version 1R and 2	129
5.	Analysis with Use of Multi-group Cross Sections Produced by ESELEM 5	145
5.1	Cross Section Preparation	145
5.2	Intercomparison Calculation for MZA	146
5.3	Intercomparison Calculation for ZPPR-2	147
6.	Improvement of Elastic Removal Cross Sections in Broad Group Constant Set	160
6.1	Introduction	160
6.2	Numerical Method	163
6.3	Comparison with Conventional Set	167
7.	Summary and Conclusions	176
Appendix 1.	SLAROM Code	182
Appendix 2.	ESELEM 5 Code	185
	ACKNOWLEDGMENTS	192
	REFERENCES	193

目 次

1. 序 論	1
2. 積分型輸送方程式の衝突確率法による解を用いた非均質系の 解析法	9
2.1 序	9
2.2 多群積分型輸送方程式	11
2.3 衝突確率法による解	17
2.4 格子計算用実効断面積	26
2.5 SLAROM コードの概要	30
3. 平板系格子における詳細群基本モードスペクトルを用いた多群実効断面積の 作成法	32
3.1 序	32
3.2 減速方程式に対する逐次解法	36
3.3 核データの扱い方	46
4. 群定数セットによる高速臨界集合体中のナトリウムボイド反応度実験の 解析	50
4.1 FCAV-1 集合体の解析	50
4.2 MZA, MZB 集合体の解析	70
4.3 ZPPR-2, ZPPR-3 集合体の解析	94
4.4 原型炉におけるナトリウムボイド反応度の空間分布の計算	126
5. ESELEM5により作成した多群実効断面積による解析	145
6. 群定数セットにおける弾性除去断面積の改良	160
6.1 序	160
6.2 数値計算法	163
6.3 従来のセットとの比較	167
7. まとめと結論	176
付 録 1. SLAROM コード	182
付 録 2. ESELEM5 コード	185
謝 辞	192
参考文献	193

LIST OF FIGURES

<u>Number</u>	<u>Title</u>	<u>Page</u>
2.1	SLAROM calculation flow	31
3.1	Interpolation scheme of point cross section	49
4.1.1	Sodium voided zones in FCA V-1	69
4.1.2	Unit cell structure	68
4.1.3	Parallel directional diffusion coefficient	68
4.1.4	Dependence of anisotropy on sodium plate thickness	69
4.1.5	Space dependence of leakage component	69
4.2.1	Calculation model and void configuration of MZA	90
4.2.2	Calculation model and void configuration of MZB	91
4.2.3	Comparison of elastic scattering cross sections of ²³ Na among ENDF/B-4, UKNDL and KEDAK files	92
4.2.4	Sodium cross section at 2.85 keV resonance	93
4.3.1	Interface view of ZPPR 2 and location of off-central voided regions	111
4.3.2	Cell structure of ZPPR 2	112
4.3.3	Dimension of structure matrix	112
4.3.4	Reference loading of ZPPR 3, Phase 3	113
4.3.5	Stages of sodium voiding experiment in ZPPR 3, Phase 3	114
4.3.6	Cylindrical model of ZPPR 2	115
4.3.7	Sample worth distribution of sodium in ZPPR 2	115
4.3.8	R-θ model of ZPPR 3, Phase 3	119
4.3.9	Sample worth distribution of sodium in ZPPR 3, Phase 3	120
4.3.10	Cumulative sodium void worth in ZPPR 3, Phase 3	121
4.3.11	Neutron flux in inner core of ZPPR 3, Phase 3	122
4.3.12	Adjoint flux in inner core of ZPPR 3, Phase 3	123

4.3.13	Adjoint flux at Fuel and F/CR in inner core of ZPPR 3, Phase 3	124
4.3.14	Neutron flux at Fuel and F/CR in inner core of ZPPR 3, Phase 3	125
4.4.1	Cross sectional view of proto-type fast breeder reactor...	141
4.4.2	Calculation model of proto-type fast breeder reactor.....	141
4.4.3	Spatial dependence of specific sodium void reactivity.....	142
4.4.4	Cumulative net sodium void reactivity.....	143
4.4.5	Comparison of real and adjoint flux between JFS-1R and JFS-V2	144
5.1	Fundamental mode neutron spectrum for normal and voided cell in inner core of ZPPR 2	156
5.2	Comparison of sample worth distribution of sodium in ZPPR 2	157
5.3	Comparison of neutron spectrum at core center of ZPPR 2...	159
6.1	Self-shielding factor for sodium in 22, 23, 33 and 34 groups	174
6.2	Comparison of neutron spectrum in iron	174
6.3	Comparison of fundamental mode neutron flux in core of FBR	175
A.1	Overlay structure of SLAROM	183
A.2	Calculation flow of ESELEM 5	188
A.3	Overlay structure of ESELEM 5	189
A.4	Structure of PRESM	186

LIST OF TABLES

<u>Number</u>	<u>Title</u>	<u>Page</u>
4.1.1	Comparison of measurements and calculations for channel void	63
4.1.2	Space dependence of spectrum component.....	64
4.1.3	Central void reactivities	64
4.1.4	Heterogeneity effects on C-1 and central void	65
4.1.5	Group contributions from heterogeneity effect	65
4.1.6	Dependence of components on spectrum for (0-10.16 cm) region	66
4.1.7	Ratio of effective elastic removal cross sections of sodium (R= fine group calculation/JAERI set)	66
4.2.1	Comparison of effective multiplication factor of MZA and MZB	80
4.2.2	Sodium void reactivity worth in MZA	81
4.2.3	Components of sodium void reactivity worth by exact perturbation in MZA	81
4.2.4	Resonance parameters of ^{23}Na at 2.85 keV	82
4.2.5	Comparison of infinite group cross sections of ^{23}Na	83
4.2.6	Sodium void reactivity worth for plate cells in MZB	84
4.2.7	Comparison of specific sodium void worth and neutron streaming effect for plate cells in MZB	85
4.2.8	Comparison of one-dimensional perturbation calculation with 70 groups for central sodium void reactivity	86
4.2.9	Anisotropy of diffusion coefficient in normal and void state $[(D_{//}/D_{\perp})_{\text{void}} - (D_{//}/D_{\perp})_{\text{normal}}] \times 100$	87
4.2.10	Sodium void reactivity worth for pin cell in MZB	88
4.2.11	Comparison of sodium void reactivity worth for central pin cell in MZB	89

4.2.12	Comparison of reactivity component by perturbation calculation for central region	89
4.3.1	Sodium void worth at core center of ZPPR 2	106
4.3.2	Sodium void worth at off-center of ZPPR 2	107
4.3.3	Comparison of effective multiplication factor.....	107
4.3.4	Comparison between calculation and measurement for sodium void worth in step at ZPPR 3, Phase 3	108
4.3.5	Comparison between calculation and measurement for cumulative voiding worth at ZPPR 3, Phase 3	109
4.3.6	Comparison between calculation and measurement for large scale sodium void worth in ZPPR 3	109
4.3.7	Comparison of sodium void worth at Na-CRP, CR and neighbouring fuel regions	110
4.4.1	Group independent buckling values	132
4.4.2	Comparison of sodium void reactivity worth distribution by JAERI Fast set version 1R and version 2	133
4.4.3	Specific sodium void reactivity distribution	134
4.4.4	Maximum sodium void reactivity worth by first order perturbation	135
4.4.5	Fission term of sodium void reactivity worth by first order perturbation	136
4.4.6	Absorption term of sodium void reactivity worth by first order perturbation	137
4.4.7	Scattering term of sodium void reactivity worth by first order perturbation	138
4.4.8	Leakage term of sodium void reactivity worth by first order perturbation	139
4.4.9	Comparison between group-wise contributions of scattering terms by JFS-V2 and 1R	140

5.1	Comparison of sodium void worth in MZB between measurement and fine group calculation	151
5.2	Component of exact perturbation in MZA calculated by broad and fine group method	152
5.3	Comparison of sodium void worth in ZPPR 2 between measurement and fine group calculation	153
5.4	Component of exact perturbation in ZPPR 2 calculated by broad and fine group method	154
5.5	Central reactivity worth in reference and voided core of ZPPR 2	155
6.1	Sample core composition and background cross sections.....	170
6.2	Self-shielding factor of elastic removal cross section for oxygen	170
6.3	Comparison of macroscopic elastic removal cross section.....	171
6.4	Comparison of self-shielding factor of iron obtained from various background masses	171
6.5	Anisotropic effect on elastic removal cross section of oxygen	172
6.6	Comparison of multiplication factor, Doppler effect and central reactivity worth in prototype FBR.....	173
A.1	Nuclide in JAERI Fast version 2 library	189

I. Introduction

Many fast-reactor critical assemblies have been built to provide physics data necessary for the design of fast power reactors. As the power reactor consists of uniform-composition rods or pins, the core is close to be homogeneous in a neutronic sense. On the other hand, most fast critical assemblies consist of heterogeneous plate cells including plates of metallic fuel. Thus, although the average compositions of the power reactor core and its simulated critical assembly may be identical, there are significant differences in the internal arrangement of the component elements. Consequently, experimental data obtained in the various heterogeneous environment should be transformed into the power reactor condition. A comparison between the experiments performed in the plate and the rod configurations has been a useful approach though the rod region is limited to a partial zone. In order to improve the ability of design method, it becomes a principal purpose to develop the calculational method to evaluate directly the experimental data obtained in the heterogeneous environments. Among many reactor parameters, the sodium void reactivity is sensitive to the local heterogeneous environment. In other words, the sodium void reactivity is an important physics parameter to assess the adequacy of calculational method though its neutronics is very complex.

As well known, the sodium void reactivity coefficient is also one of the main concerns in the safety related reactor physics since the value becomes positive in large plutonium fueled fast reactors as pointed out first by Nims and Zweifel,⁽¹⁾ and extensively studied by Ohta and Nishihara.⁽²⁾ The maximum positive sodium void reactivity may be beyond several dollars in a large commercial type reactor with a conventional two-zone core. Thus, an accurate prediction of the sodium void reactivity

will be essential to increase a confidence in calculational methods used in the design work of power reactors.

The sodium void reactivity coefficient can be resolved by the perturbation theory into capture, fission, spectral and leakage components. The spectral component is defined as the reactivity change due to the change of elastic and inelastic scattering cross sections caused by the removal of sodium. This component is sensitive to an energy variation of the adjoint spectrum. The capture and fission components are defined as the reactivity changes accompanied by the changes of macroscopic capture and fission cross sections, respectively. The removal of sodium, of course, decreases the capture cross section and the resulting spectrum hardening plays an important role for this component. The leakage component corresponds to the change in reactivity caused by the change in macroscopic transport cross section. Because of the heterogeneity arrangement of fuel, sodium and moderator plates, the neutron streaming effect is enhanced when sodium is removed. As a result, the leakage becomes more anisotropic depending on the direction of plate surfaces. Large corrections for this effect will be necessary in order to obtain an accurate prediction of sodium void reactivities measured in critical assemblies.

Usually, for large plutonium fueled fast reactors, the capture and spectral components are positive and take the maximum values at the center of core, but the fission and leakage components are negative. Consequently, the total reactivity is determined through the cancellation of large positive and negative components, so it sometimes has a relatively large uncertainty. These components are sensitive to the cross sections, the calculational method and the model.

The standard analytical model adopted here is a two-dimensional rz diffusion calculation. The reactivity has been obtained also by the first

order or the exact perturbation calculations. The perturbation theory is helpful to investigate the contribution from each cross section type or energy group. For a more complex geometry with distributed control rods or a sodium voiding pattern in off-central region, three-dimensional calculations have been required for a completely satisfactory description. Although two-dimensional xy calculations are not so time-consuming, it is not so easy to determine the space and energy dependent transverse bucklings with and without sodium.

The plate heterogeneity effect can be taken into account in course of producing multi-group cross sections or in the use of a group constant set. The heterogeneity effect in fast critical assemblies results from the spatial variation of the fission source and from the resonance self-shielding effect of heavy elements. The spatial distribution of the neutron flux is usually obtained by solving the transport equation. The discrete ordinates (S_n) method and the collision probability method are well known as a solution method. The latter method is superior to the S_n method for the cell calculation in a view point of computation economy, and hence has been often used for the lattice calculation^{(3),(4)} in a thermal reactor. To the calculation of fast critical assemblies, the integral transport perturbation method was applied in the CALHET⁽⁵⁾ code. In the present work the SLAROM code has been developed for the analysis of the heterogeneous system in fast critical facilities. This code solves the multi-group integral transport equation by the collision probability method and edits the cell averaged effective cross sections. The SLAROM code is programmed to be able to calculate the anisotropic diffusion coefficients based on the Benoist's formula.⁽⁶⁾ It has been applied to estimate the neutron streaming effect when sodium is removed.⁽⁷⁾ Its contribution to the sodium void reactivity has been obtained by the

CIPER code⁽⁸⁾ which has been developed for the perturbation calculation in two- or three-dimensions. We use the JAERI Fast set^{(9), (10)} in the present analysis of sodium void reactivity. The reactivity coefficients depend not only on the basic nuclear data but also on the processing method of group cross sections. We have intended to assess the capability of the JAERI Fast set in the prediction of sodium void reactivity as one of the objects of the present work.

At first, we have analysed the sodium void reactivity measurements to examine the adequacy or limitations of the calculational models and methods, and to assess the accuracy of each version of the JAERI Fast set. In the course of the revisions of this set, many benchmark cores have been analysed and their results were successively reflected to the revisions. The comparative study has been performed among these versions in this work.

The critical assemblies selected for the present sodium void analysis were FCA V-1, MZA, MZB, ZPPR 2 and ZPPR 3. All of them are plutonium fueled assemblies. FCA V-1⁽¹¹⁾ was a physical mock-up of Japan Experimental Reactor "JOYO"⁽¹²⁾ at JAERI, MZA and MZB⁽¹³⁾ were constructed at ZEBRA in U.K. Winfrith for the simulation of Japan proto-type fast breeder reactor "MONJU",⁽¹⁴⁾ ZPPR assembly 2⁽¹⁵⁾ was a benchmark assembly for a demonstration reactor, and ZPPR assembly 3⁽¹⁶⁾ had the same core volume as assembly 2 but the complicated control rods and control rod positions were added. ZPPR 2 and 3 were constructed at ANL.

Many analyses have been made for the sodium void reactivities measured in fast critical assemblies. Greebler and Pflasterer⁽¹⁷⁾ reviewed for the early works, and Hummel and Okrent⁽¹⁸⁾ gave an extensive discussion in their monograph, Pitterle et al.⁽¹⁹⁾ analysed ZPR III assembly 48 and 49, and ZPR IV assembly 2 and 3 and discussed about

nuclear data and calculational methods adopted for the sodium void calculations. They used the MC² code⁽²⁰⁾ to obtain multi-group cross sections from the ENDF/B-1 data. The analysis of MZA and MZB assemblies was made with use of the MURAL code and the FGL 5 data by Stevenson et al.⁽²¹⁾ The neutronics properties related to the sodium loss in ZPPR 2 were measured and analysed by Davey et al.⁽²²⁾ In their analysis, the MC² code was used to calculate the multi-group cross sections and the fine structure flux within the cell was calculated by the CALHET code. The ENDF/B-1 data were adopted as the nuclear data.

Though the use of group constant set is convenient for its simplicity and economy in computation time, some shortages have been pointed out^{(23), (24)} especially in the calculation of sodium void reactivity. The more accurate multi-group cross sections have been produced by a fine spectrum method. The MC² - 2⁽²⁵⁾ and MURALB codes⁽²⁶⁾ are well known for it. Another object of the present work is to develop the calculation method for fine spectrum and multi-group cross sections in the heterogeneous system and to apply it to the analysis of sodium void reactivities. The ESELEM code series⁽²⁷⁾ have been developed to examine the adequacy of the method to produce the group constant set. The ESELEM 5 code is the latest version of them. In this code, the fine structure flux in the cell is obtained by solving the integral transport equation with use of the collision probability method and the slowing down source is calculated with use of a recurrence formula for elastic and inelastic scattering. Therefore, the heterogeneity effect can be taken into account directly in the stage of the fine group structure. Some devices have been incorporated in the program of ESELEM 5. By using this code, we analysed the sodium void reactivities measured at MZA and ZPPR assembly 2. The results are compared with those obtained by the group

constant set and examined about their difference in each component.

In the following, we have attempted to improve the conventional group constant set with regard for its merits. One of the most serious defects was that the elastic removal cross sections of light and intermediate nuclei were considerably inaccurate in the vicinity of the large resonances. This causes errors in the spectrum component of sodium void reactivity through the adjoint neutron spectrum and the change of elastic removal cross sections of sodium. The more accurate self-shielding factors were obtained for the elastic removal cross section of light and intermediate nuclei and incorporated into the JAERI Fast set, version 2. The comparative study of neutron spectrum and some reactor parameters have been made among the original set, the revised set and the fine group method.

This thesis consists of six chapters and two appendices. The introductory remarks are given at the first part of each chapter. The reviews and scopes will be mentioned there. In Chapter 2 explained is the analytical method of heterogeneous fast reactor system. The multi-group integral transport equation is derived and its solution method using the collision probability method is described. Then, the cell averaged effective cross sections and the anisotropic diffusion coefficient are obtained. These functions are incorporated in the SLAROM code. This code includes the one-dimensional diffusion calculation and perturbation calculation routines. Chapter 3 describes the calculation method of fine neutron spectrum and multi-group cross sections. The heterogeneous cell calculation is performed with use of the collision probability method. The heterogeneity effect on resonance self-shielding factors is taken into consideration based on the rational approximation for multi-region cell. The slowing-down equation is solved by deriving the

recurrence relations for elastic and inelastic scatterings. The anisotropy of elastic scattering is considered up to the P_1 order of Legendre coefficients. The fine group cross section library is produced from the nuclear data file with ENDF/A or /B type format by the PRESM code. The broad group macroscopic or microscopic cross sections can be collapsed with an arbitrary group structure from the fine group data.

Chapter 4 is devoted to describe the calculational results of sodium void reactivity. All the calculations have been performed with use of the broad group constant sets, the JAERI Fast set: versions 1 and 2. In the analysis of FCA V-1 assembly, it is shown that the neutron streaming effect plays a very important role for the consistent explanation of the sodium void reactivity measurements.

ZPPR assembly 3 had the control rods and the control rod channels in complicated patterns, so the three-dimensional diffusion calculations have been performed to exclude an ambiguity accompanied by the rz or xy models. The control rod effect on the sodium void reactivity is also discussed in this chapter. The spatial distribution of sodium void reactivity coefficient is calculated for a real proto-type fast breeder reactor and the maximum positive worth is predicted. In this calculation, the results by two versions of the JAERI Fast sets are compared and discussed in detail about their differences.

In Chapter 5, the calculational results by using the ESELEM 5 code are presented for MZA and ZPPR 2 assemblies. Some neutronics parameters of ZPPR 2 are also calculated and compared with measurements. These results show more positive values than those obtained in Chapter 4 especially in the spectrum component. The calculational results⁽²⁸⁾ of various neutronics parameters obtained by the JAERI Fast set with 25 group structure and by ESELEM 5 was submitted for an international comparison

of the benchmark problem on the large liquid metal cooled fast breeder reactor proposed by NEACRP.⁽²⁹⁾ While this reactor is composed of homogeneous regions, we could draw substantially general conclusions from the comparison of these results.

In Chapter 6, the accuracy of elastic removal cross sections of light and intermediate nuclei is investigated for a typical reactor composition. The self-shielding factors for elastic removal cross sections are calculated and used for the revision of the JAERI Fast set. Neutron spectra and some neutronics parameters are calculated with the revised and the conventional sets. The results are discussed there.

Descriptions of computer codes, SLAROM and ESELEM 5 developed in this study are given in Appendices 1 and 2, respectively. More detailed informations about these codes have been published in (30), (31).

2. Analytical Method of Heterogeneous System with Use of Integral Transport Solution by Collision Probability Method

2.1. Introduction

The heterogeneity effect affects significantly the neutronics of fast critical assemblies differing from the case of power reactors. Generally power reactors consist of bundles of uniform composition rods or pins clad with stainless steel and cooled with sodium. Accordingly the neutronics of power reactors can be fairly well predicted with the homogeneous model. On the other hand, the critical assemblies may contain, for example, plates of plutonium metal, uranium metal or their alloy, together with plates of uranium oxide, stainless steel and sodium-filled cans. Thus, although the average compositions of a power reactor and its simulated critical assembly may be identical, there are significant differences in the internal arrangement of the component elements. In the analysis of the experiments performed in the critical assemblies, therefore, we should take account of the plate heterogeneity effect adequately.

The heterogeneity effect arises mainly from two energy regions. One is due to the heterogeneity distribution of a fission source above a few hundreds keV. This results in a remarkable flux variation through the material regions of a cell. Hence, we should obtain the accurate spatial distribution of the neutron flux. The other is due to the heterogeneity arrangement of the fuel and moderator, which affects the effective resonance absorption by heavy nuclides as well known. Consequently, this heterogeneity effect should be taken into account in the calculation of effective cross sections for each fuel region, as the correction for resonance shielding factors.

To obtain the neutron flux distribution, we should solve the transport

equation since the optical thickness of each region in the unit cell is small compared with the mean free path of neutrons. The S_n and collision probability methods are frequently used for obtaining the solution.

The SLAROM code has been developed for the analysis of fast facilities consisting of the heterogeneous cells. This code solves the integral transport equation by using the collision probability method for the plate and pin geometries. The heterogeneity resonance shielding effect can be taken into consideration based on the rational approximation for the multi-region cell. The SLAROM code used the JAERI Fast set as a standard group constant library. This is the multi-group constant set which is popularly used in Japan, so many computer codes have been developed to use this set. However, most of them perform the diffusion calculation for the homogeneous system. The development of the transport code for the heterogeneous calculation will extend the availability of the JAERI Fast set.

To analyse fast critical assemblies, we must perform at first the cell calculations to obtain the averaged effective cross sections for all the types of cell patterns of the core and blanket. Then the one dimensional diffusion calculations are usually performed with these cross sections to obtain the condensed cross sections which are used in the multi-dimensional calculations. Since the number of the cell patterns is, sometimes, more than ten, the data management becomes complicated and causes easily errors if the cell and diffusion calculations are performed by using respectively independent computer codes. The SLAROM code is therefore designed to be able to calculate them without any intermediate hand treatment. Moreover the usage of the free format to input data will be helpful to decrease the input errors.

In the following sections, the method of solution, content of edit, and brief calculation flow are described. The detailed structure of code is shown in Appendix 1.

2.2. Multi-group Integral Transport Equation

The neutron flux in a reactor is thought to be determined by the superposition of the fine structure in the cell and the global distribution over the whole reactor. To obtain such a neutron flux at once, a large number of mesh points would be required, so it is not a realistic method. We usually assume the separability of the fine structure distribution from the global one and calculate the neutron flux according to the following steps. At first, the cell calculation is performed in order to introduce the fine structure effect into the cell averaged cross sections under the assumption that the global distribution is described by the fundamental mode and the leakage of neutrons from the reactor is represented by the pseudo-absorption, DB^2 . After that, the homogeneous reactor calculation is carried out for the whole reactor with use of the effective cross sections thus obtained. This approach has generally been used in the analysis of thermal reactors. The cell averaged cross sections are defined as follows.

The general integro-differential Boltzman transport equation for neutrons is written as

$$\bar{\Omega} \cdot \text{grad } \psi(\bar{r}, E, \bar{\Omega}) + \Sigma_t(\bar{r}, E) \psi(\bar{r}, E, \bar{\Omega}) = q(\bar{r}, E, \bar{\Omega}) \quad (2.1)$$

with

$$q(\bar{r}, E, \bar{\Omega}) = \int_E dE' \int_{\bar{\Omega}'} d\bar{\Omega}' \{ \Sigma_s(\bar{r}, E' \rightarrow E, \bar{\Omega}' \rightarrow \bar{\Omega}) + \chi(E, \bar{\Omega}) \nu \Sigma_f(\bar{r}, E') \} \psi(\bar{r}, E', \bar{\Omega}')$$

By assuming that the neutron flux $\psi(\bar{r}, E, \bar{\Omega})$ in the reactor consisting of

the periodic cell is separable into the global flux $\phi_h(\bar{r}, E, \bar{\Omega})$ and the fine structure flux $\psi_c(\bar{r}, E, \bar{\Omega})$, Eq.(2.1) is rewritten as follows:

$$\begin{aligned} \bar{\Omega} \cdot \text{grad } \phi_h(\bar{r}, \bar{\Omega}) \psi_c(\bar{r}, \bar{\Omega}) + \Sigma_t(\bar{r}) \phi_h(\bar{r}, \bar{\Omega}) \psi_c(\bar{r}, \bar{\Omega}) \\ = q_h(\bar{r}, \bar{\Omega}) q_c(\bar{r}, \bar{\Omega}) \end{aligned} \quad (2.2)$$

where the energy variable E is suppressed for simplicity.

We define the effective cross section of the reaction x so as to conserve the reaction rate in the unit cell:

$$\langle \Sigma_x \rangle = \frac{\int_{V_c} d\bar{r} \int d\bar{\Omega} \Sigma_x(\bar{r}) \psi(\bar{r}, \bar{\Omega})}{\int_{V_c} d\bar{r} \int d\bar{\Omega} \psi(\bar{r}, \bar{\Omega})} \quad (2.3)$$

Integrating Eq.(2.2) over space and angle, the first term on the left hand side is written, by introducing the cell averaged value $\bar{\psi}_c$ which is the same for all the cells, as follows:

$$\begin{aligned} \int d\bar{r} \int d\bar{\Omega} \bar{\Omega} \cdot \text{grad} \{ \phi_h(\bar{r}, \bar{\Omega}) \psi_c(\bar{r}, \bar{\Omega}) \} \\ = \int d\bar{r} \int d\bar{\Omega} \{ \bar{\Omega} \cdot \psi_c(\bar{r}, \bar{\Omega}) \text{grad} \phi_h(\bar{r}, \bar{\Omega}) + \bar{\Omega} \cdot \phi_h(\bar{r}, \bar{\Omega}) \text{grad} \psi_c(\bar{r}, \bar{\Omega}) \} \\ = \bar{\psi}_c \int d\bar{r} \int d\bar{\Omega} \bar{\Omega} \cdot \text{grad} \phi_h(\bar{r}, \bar{\Omega}) + \overline{\bar{\Omega} \cdot \text{grad} \psi_c(\bar{r}, \bar{\Omega})} \int d\bar{r} \int d\bar{\Omega} \phi_h(\bar{r}, \bar{\Omega}) \end{aligned} \quad (2.4)$$

The second term on the right hand side of Eq.(2.4) can be evaluated as follows:

$$\begin{aligned} \overline{\bar{\Omega} \cdot \text{grad} \psi_c(\bar{r}, \bar{\Omega})} &= \frac{1}{4\pi V_c} \int_{V_c} d\bar{r} \int d\bar{\Omega} \bar{\Omega} \cdot \text{grad} \psi_c(\bar{r}, \bar{\Omega}) \\ &= \frac{1}{4\pi V_c} \int_{V_c} ds \int d\bar{\Omega} \bar{\Omega} \psi_c(\bar{r}, \bar{\Omega}) \\ &= 0 \end{aligned}$$

where ds is the surface element of V_c . Since the above equation represents the total leakage from a unit cell, it is zero from the boundary condition. Integrating the second term of Eq.(2.2), we have

$$\int d\bar{r} \int d\bar{\Omega} \Sigma_t(\bar{r}) \phi_h(\bar{r}, \bar{\Omega}) \psi_c(\bar{r}, \bar{\Omega}) = \overline{\Sigma_t \psi_c} \int d\bar{r} \int d\bar{\Omega} \phi_h(\bar{r}, \bar{\Omega}) \quad , \quad (2.5)$$

$$\overline{\Sigma_t \psi_c} = \frac{1}{4\pi V_c} \int_{V_c} d\bar{r} \int d\bar{\Omega} \Sigma_t(\bar{r}) \psi_c(\bar{r}, \bar{\Omega}) \quad .$$

In the same manner, the scattering and the fission terms of Eq.(2.1) are also rewritten as

$$\begin{aligned} \int d\bar{r} \int d\bar{\Omega} \Sigma_s(\bar{r}) \phi_h(\bar{r}, \bar{\Omega}) \psi_c(\bar{r}, \bar{\Omega}) \\ = \overline{\Sigma_s \psi_c} \int d\bar{r} \int d\bar{\Omega} \phi_h(\bar{r}, \bar{\Omega}) \end{aligned} \quad (2.6)$$

$$\begin{aligned} \int d\bar{r} \int d\bar{\Omega} \nu \Sigma_f(\bar{r}) \phi_h(\bar{r}, \bar{\Omega}) \psi_c(\bar{r}, \bar{\Omega}) \\ = \overline{\nu \Sigma_f \psi_c} \int d\bar{r} \int d\bar{\Omega} \phi_h(\bar{r}, \bar{\Omega}) \quad . \end{aligned} \quad (2.7)$$

From the definition (2.3), the effective cross sections can be obtained by dividing Eqs.(2.5) ~ (2.7) by $\int \psi(\bar{r}, \bar{\Omega}) d\bar{r} d\bar{\Omega}$. With use of the relation:

$$\int d\bar{r} \int d\bar{\Omega} \psi(\bar{r}, \bar{\Omega}) = \bar{\psi}_c \int d\bar{r} \int d\bar{\Omega} \phi_h(\bar{r}, \bar{\Omega}) \quad ,$$

the effective cross sections can be defined as follows:

$$\begin{aligned} \langle \Sigma_t \rangle &= \overline{\Sigma_t \psi_c} / \bar{\psi}_c \quad , \\ \langle \Sigma_s \rangle &= \overline{\Sigma_s \psi_c} / \bar{\psi}_c \quad , \\ \langle \nu \Sigma_f \rangle &= \overline{\nu \Sigma_f \psi_c} / \bar{\psi}_c \quad , \end{aligned} \quad (2.8)$$

In order to obtain the neutron flux in the cell we should solve the transport equation since the thickness of each material in the cell is smaller than the mean free path of fast neutrons and the diffusion approximation is inadequate. For solving the transport equation, the P_ℓ method and S_n method are frequently used to the integro-differential transport equation and the collision probability method, as well known, to the integral transport equation. The S_n method is useful for treating the anisotropic scattering but it requires the relatively large computation time. On the other hand, the collision probability method is accurate and not time-consuming if the scattering is almost isotropic and the flux distribution can be assumed to be flat as in the case of the cell. Therefore, the latter method has been adopted in the SLAROM code.

We treat the multi-group transport equation in this code. The multi-group form of the integral transport equation is easily derived from that of the integro-differential equation as follows.

Let the multi-group integro-differential transport equation write as

$$\begin{aligned} \bar{\Omega} \cdot \text{grad } \phi_g(\bar{r}, \bar{\Omega}) + \Sigma_{t,g}(\bar{r}) \phi_g(\bar{r}, \bar{\Omega}) \\ = \int d\bar{\Omega}' \sum_{g'} \{ \Sigma_{g' \rightarrow g}(\bar{r}, \bar{\Omega}' \rightarrow \bar{\Omega}) + \frac{1}{4\pi} \chi_g v \Sigma_{f,g}(\bar{r}) \} \phi_{g'}(\bar{r}, \bar{\Omega}') \\ = Q_g(\bar{r}, \bar{\Omega}) \quad , \end{aligned} \quad (2.9)$$

where g is the group suffix and $\Sigma_{g' \rightarrow g}$ the scattering transfer cross section from g' to g .

Expressing the gradient term in the spatial variable R , which relates a fixed point \bar{r} to an arbitrary point \bar{r}' along the direction $\bar{\Omega}$,

$$\bar{\Omega} \cdot \text{grad} = - \frac{d}{dR} \quad ,$$

then Eq.(2.9) is rewritten as

$$-\frac{\partial}{\partial R} \phi_g(\bar{r}-R\bar{\Omega}, \bar{\Omega}) + \Sigma_{t,g}(\bar{r}-R\bar{\Omega}) \phi_g(\bar{r}-R\bar{\Omega}, \bar{\Omega}) = Q_g(\bar{r}-R\bar{\Omega}, \bar{\Omega}) \quad (2.10)$$

When the source term Q_g is known, the solution is given by

$$\begin{aligned} \phi_g(\bar{r}-R\bar{\Omega}, \bar{\Omega}) &= \phi_g(\bar{r}-R_0\bar{\Omega}, \bar{\Omega}) \exp\left[-\int_0^{R_0} \Sigma_{t,g}(\bar{r}-R'\bar{\Omega}) dR'\right] \\ &+ \int_0^{R_0} dR' Q_g(\bar{r}-R'\bar{\Omega}, \bar{\Omega}) \exp\left[-\int_0^{R_0} \Sigma_{t,g}(\bar{r}-R''\bar{\Omega}) dR''\right], \end{aligned}$$

where R_0 is the distance from \bar{r} to the outer boundary in the direction $-\bar{\Omega}$. When the external source does not exist, ϕ_g in the direction $-\bar{\Omega}$ becomes zero at the boundary. As a result, the multi-group integral transport equation is obtained as follows:

$$\phi_g(\bar{r}-R\bar{\Omega}, \bar{\Omega}) = \int_0^{R_0} dR' Q_g(\bar{r}-R'\bar{\Omega}, \bar{\Omega}) \exp\left[-\int_0^{R_0} \Sigma_{t,g}(\bar{r}-R''\bar{\Omega}) dR''\right], \quad (2.11)$$

or, using the relations

$$\bar{r}' = \bar{r} - R\bar{\Omega}_R, \quad R = |\bar{r} - \bar{r}'|,$$

it can be written as

$$\begin{aligned} \phi_g(\bar{r}, \bar{\Omega}) &= \int_V \frac{d\bar{r}'}{|\bar{r}-\bar{r}'|^2} \delta(\bar{\Omega}, \bar{\Omega}_R) Q_g(\bar{r}', \bar{\Omega}) \\ &\cdot \exp\left[-\int_0^{|\bar{r}-\bar{r}'|} \Sigma_{t,g}(\bar{r}-\bar{R}' \frac{(\bar{r}-\bar{r}')}{|\bar{r}-\bar{r}'|}) dR'\right] \end{aligned} \quad (2.12)$$

By integrating this equation over $\bar{\Omega}$, we have the following equation for the total flux $\psi_g(\bar{r})$,

$$\psi_g(\bar{r}) = \int_V \frac{dr'}{|\bar{r}-\bar{r}'|^2} Q_g(\bar{r}') \exp[-\lambda_g(\bar{r},\bar{r}')] , \quad (2.13)$$

where we introduce the optical path length $\lambda_g(\bar{r},\bar{r}')$ defined by

$$\lambda_g(\bar{r},\bar{r}') = \int_0^{|\bar{r}-\bar{r}'|} dR' \Sigma_{t,g}(\bar{r}-R' \frac{(\bar{r}-\bar{r}')}{|\bar{r}-\bar{r}'|}) . \quad (2.14)$$

2.3. Solution by Collision Probability Method

To explain the collision probability method, we start with Eq.(2.13) with energy variable E for use in Chapter 3:

$$\Sigma(\bar{r}, E)\phi(\bar{r}, E) = \int_V d\bar{r}' P(\bar{r}, \bar{r}', E) [\int dE' \Sigma_s(E' \rightarrow E, r')\phi(r', E') + S(\bar{r}', E)], \quad (2.15)$$

where

$$P(\bar{r}, \bar{r}', E) = \frac{\Sigma(\bar{r}, E)}{4\pi|\bar{r}-\bar{r}'|^2} \exp[-\lambda(\bar{r}, \bar{r}', E)] \quad . \quad (2.16)$$

The collision probability will be derived at first for one dimensional slab geometry and then for cylindrical geometry.

(1) Derivation of matrix equation

The integral transport equation in one dimensional slab geometry is obtained by integrating Eq.(2.15) over y and z coordinates as follows: (*)

$$\Sigma(x, E)\phi(x, E) = \int_V dx' \frac{1}{2} \Sigma(x, E) E_1[\lambda(x, x', E)] [Q(x', E) + S(x', E)] \quad , \quad (2.17)$$

$$\begin{aligned} (*) \quad \int_V d\bar{r}' P(\bar{r}, \bar{r}', E) &= \int_V \frac{\Sigma(\bar{r}, E)}{4\pi} \frac{\exp[-\int_0^{\bar{R}} \Sigma(s) ds]}{|\bar{r} - \bar{r}'|^2} d\bar{r}' \\ &= \frac{\Sigma(x, E)}{4\pi} \int_V dx' \int_0^\infty 2\pi r' dr' \cdot \frac{\exp(-\bar{\Sigma R})}{R^2} \\ &= \frac{\Sigma(x, E)}{2} \int_V dx' \int_x^\infty \frac{\exp(-\bar{\Sigma R})}{R} dR \quad , \end{aligned}$$

where $\bar{\Sigma R}$ denotes the optical path length and we have changed the integral variables by making use of the relation $R^2 = r'^2 + x^2$.

where $E_1[\lambda(x, x', E)]$ is the exponential integral function defined by

$$E_n(x) = \int_1^{\infty} \frac{e^{-xu}}{u^n} du \quad ,$$

and

$$Q(x', E) = \int_0^{\infty} dE' [\Sigma_e(E' \rightarrow E, x') + \Sigma_{in}(E' \rightarrow E, x')] \phi(x', E') \quad ,$$

$$S(x', E) = \int_0^{\infty} dE' \chi(E) \nu \Sigma_f(x', E') \phi(x', E') + s(x', E) \quad ,$$

in which Σ_e , Σ_{in} and $\nu \Sigma_f$ are macroscopic elastic scattering, inelastic scattering and ν times fission cross sections, respectively.

When the region V consists of M unit cells and each cell has N regions, the balance equation for the region ℓ of the cell j is written by using the neutron flux $\phi_{\ell}^{(j)}$, as follows:

$$\Sigma_{\ell}^{(j)} \phi_{\ell}^{(j)}(x, E) = \sum_{i=1}^M \sum_{k=1}^N \int_{V_k^{(i)}} dx' \frac{1}{2} \Sigma_{\ell}^{(j)}(E) E_1[\lambda(x, x', E)] \cdot [Q_k^{(i)}(x', E) + S_k^{(i)}(x', E)] \quad , \quad (2.18)$$

where the suffices of the cross section show the cell and region numbers and $V_k^{(i)}$ is the volume of the region k in the cell i . The average neutron flux and source in the region ℓ of the cell j are given by the following equations:

$$\bar{\phi}_{\ell}^{(j)}(E) = \frac{1}{V_{\ell}^{(j)}} \int_{V_{\ell}^{(j)}} dx \phi_{\ell}^{(j)}(x, E) \quad ,$$

$$\bar{S}_{\ell}^{(j)}(E) = \frac{1}{V_{\ell}^{(j)}} \int_{V_{\ell}^{(j)}} dx S_{\ell}^{(j)}(x, E) \quad .$$

By integrating both the sides of Eq.(2.18) over the region ℓ in the cell j and performing the integration over the volume $V_k^{(i)}$ on the right hand side, we obtain

$$\Sigma_{\ell}^{(j)} V_{\ell}^{(j)} \bar{\phi}_{\ell}^{(j)}(E) = \sum_{i=1}^M \sum_{k=1}^N V_k^{(i)} P_{ij}^{k \rightarrow \ell} [\bar{Q}_k^{(i)}(E) + \bar{S}_k^{(i)}(E)] . \quad (2.19)$$

The first flight collision probability is defined by using the collision density as the weighting function:

$$P_{ij}^{k \rightarrow \ell} = \frac{\Sigma_{\ell}^{(j)}(E) \int dx' \int dx \frac{1}{2} E_1 [\lambda(x, x', E)] \Sigma_k^{(i)} \phi_k^{(i)}(x', E)}{\int dx' \Sigma_k^{(i)} \phi_k^{(i)}(x', E)} .$$

By assuming that the cross sections are constant and the neutron flux and source are flat over each region, we have

$$P_{ij}^{k \rightarrow \ell} = \frac{\Sigma_{\ell}^{(j)}(E)}{2 V_k^{(i)}} \int_{V_k^{(i)}} dx' \int_{V_{\ell}^{(j)}} dx E_1 [\lambda(x, x', E)] . \quad (2.20)$$

Thus, suppressing variable E , Eq.(2.19) becomes

$$\Sigma_{\ell}^{(j)} V_{\ell}^{(j)} \bar{\phi}_{\ell}^{(j)} = \sum_{i=1}^M \sum_{k=1}^N V_k^{(i)} P_{ij}^{k \rightarrow \ell} [\bar{Q}_k^{(i)} + \bar{S}_k^{(i)}] . \quad (2.21)$$

For the case where the unit cell is infinitely repeated, the value of the neutron flux of the region ℓ is the same for all the cells. Hence, dropping the suffix of cell j , Eq.(2.21) is rewritten as

$$\Sigma_{\ell} V_{\ell} \bar{\phi}_{\ell} = \sum_{i=1}^{\infty} \sum_{k=1}^N V_k^{(i)} P_i^{k \rightarrow \ell} [\bar{Q}_k^{(i)} + \bar{S}_k^{(i)}] .$$

Suppressing the summation over the suffix i for the infinitely repeated cells, this equation is further reduced to

$$\sum_{\ell} V_{\ell} \bar{\phi}_{\ell} = \sum_{k=1}^N V_k P^{k \rightarrow \ell} [\bar{Q}_k + \bar{S}_k] \quad (2.22)$$

The neutron conservation law requires the following relation:

$$\sum_{\ell=1}^N P^{k \rightarrow \ell} = 1 \quad (2.23)$$

In addition, the following reciprocity relation can be derived directly from Eq.(2.20) for the use of the calculation of collision probability:

$$\sum_k V_k P^{k \rightarrow \ell} = \sum_{\ell} V_{\ell} P^{\ell \rightarrow k} \quad (2.24)$$

We now write Eq.(2.22) in the matrix form for the volume integrated flux and source as follows:

$$\underline{\Sigma} \underline{\phi} = P (\underline{Q} + \underline{S}) \quad (2.25)$$

where $\underline{\Sigma}, \underline{\phi}, \underline{Q}$, and \underline{S} are N dimensional vectors and P is N x N matrix:

$$\begin{pmatrix} \Sigma_1 \phi_1 \\ \Sigma_2 \phi_2 \\ \vdots \\ \Sigma_n \phi_n \end{pmatrix} = \begin{pmatrix} P_{11} & P_{21} & \dots & P_{N1} \\ P_{12} & & & \\ \vdots & & & \\ P_{1N} & & & P_{NN} \end{pmatrix} \times \left\{ \begin{pmatrix} Q_1 \\ Q_2 \\ \vdots \\ Q_N \end{pmatrix} + \begin{pmatrix} S_1 \\ S_2 \\ \vdots \\ S_N \end{pmatrix} \right\}$$

In the multi-group notation, Q_{kg} is calculated by

$$Q_{kg} = \sum_{g'=1}^{g-1} \Sigma_{k,g' \rightarrow g} \phi_{k,g'} \quad ,$$

where the right hand term is equal to $(\Sigma_{t,k,g} - \Sigma_{k,g \rightarrow g})\phi_{k,g}$.

The flux ϕ can easily be calculated from Eq.(2.25) by direct matrix inversion method if P is factorized. Since Eq.(2.25) is given at each energy point or energy group, the neutron flux can be obtained by solving these equations successively, from the highest energy group to lower groups, where the slowing down source is calculated from the solution for the higher energy groups.

When the system is finite, the neutron leakage from the cell should be considered. For a large system, the fundamental mode approximation may be used and the average leakage from the system is represented by $DB^2\phi$. Since, on the other hand, the average collision rate is given by $\Sigma_t\phi$, the non-leakage probability is $\Sigma_t/(\Sigma_t + DB^2)$. Therefore balance equation (2.22) is written on the basis of the conservation law as

$$\Sigma_{\ell} \phi_{\ell} = \frac{\Sigma_t}{\Sigma_t + DB^2} \sum_{k=1}^N P^{k \rightarrow \ell} [Q_k + S_k] ,$$

or by rewriting the sufficies k, ℓ by i,j, respectively, as a usual notation

$$(\Sigma_j + DB^2 \frac{\Sigma_j}{\Sigma_t})\phi_j = \sum_{i=1}^N P_{ij} [Q_i + S_i] , \quad (2.26)$$

where ϕ_j , Q_i and S_i are respectively the volume integrated values in the region j or i.

(2) Calculation of collision probability in slab geometry

The collision probability from the region i to j is calculated numerically, by integrating Eq.(2.20) over x and x', as follows:

$$P_{ij} = \frac{1}{2\lambda_i} [E_3(\lambda_o) - E_3(\lambda_o + \lambda_i) - E_3(\lambda_o + \lambda_j) + E_3(\lambda_o + \lambda_i + \lambda_j)] , \quad (2.27)$$

where λ_i and λ_j are the optical path lengths in the region i and j , respectively, and λ_0 is the value in between the regions i and j . In addition, we have used the recurrence relation for the exponential integral function:

$$E_n(x) = \int_x^\infty E_{n-1}(x) dx$$

Since Eq.(2.27) becomes numerically inaccurate when the optical path length of the region i or j is small, we use the following approximate equations: (3), (32)

a) $\lambda_j < 0.005$,

$$P_{ij} = \frac{\lambda_j}{2\lambda_i} [E_2(\lambda_0) - E_2(\lambda_0 + \lambda_i)] \quad (2.28)$$

b) $\lambda_i < 0.005$,

$$P_{ij} = \frac{1}{2} [E_2(\lambda_0) - E_2(\lambda_0 + \lambda_j)] \quad (2.28')$$

c) $\lambda_i < 0.005$ and $\lambda_j < 0.005$,

$$P_{ij} = \frac{1}{2} \lambda_j E_1(\lambda_0) \quad (2.28'')$$

(3) Boundary condition of cell calculation

Two types of boundary conditions should be given in the cell calculation. The first one determines the geometrical structure of cells. When the symmetric boundary condition is chosen, the unit cell including its image part is infinitely repeated. On the other hand, the periodic boundary condition means that the same cell pattern is infinitely repeated

on both the sides of the assigned cell.

The second boundary condition is concerned with the treatment of neutron paths crossing the outer boundary. An isotropic or perfect reflective condition can be chosen in the calculation of collision probability. When the perfect reflective condition is used, neutron passes straightly until it suffers a collision in the region j even if it crosses the cell boundary. In this case the collision probability is calculated by tracing over a number of cells. Under the isotropic condition, on the other hand, the neutron path is traced only in the unit cell, and the probability P_{io} that neutron, born in the region i , collides for the first time at the outside of the unit cell, is obtained from

$$P_{io} = \int_{V_i} dx' \frac{1}{2V_i} E_1[\lambda(x,s,E)] \quad . \quad (2.29)$$

On the other hand, by denoting the probability that the isotropically incident neutron collides for the first time in the region i as Q_{oi} , then the collision number in the region i is given by $\frac{S}{4}Q_{oi}$, because the current into the region is $\frac{S}{4}$ when the uniform flux ϕ is incident isotropically on the surface S of the cell. From the reciprocity theorem we get the following relation:

$$Q_{oi} = \frac{4V_i}{S} \sum_j P_{io} \quad . \quad (2.30)$$

Furthermore we represent the probability that the isotropically incident neutron escapes from the cell without suffering any collision as Q_{oo} :

$$Q_{oo} = 1 - \sum_{j=1}^N Q_{oj} \quad .$$

Consequently the collision probability P_{ij} is written by using the collision probability P_{ij}^* in the unit cell, as

$$P_{ij} = P_{ij}^* + P_{io} \frac{Q_{oi}}{1 - Q_{oo}} \quad (2.31)$$

The computation time is required much more for the perfect reflective condition. In this case, however, a sufficient accuracy will be achieved if neutron is traced over the six or seven mean free path lengths, because the collision probability decreases exponentially with the mean free path length.

(4) Collision probability in cylindrical geometry

In the case of the cylindrical cell (annular cell), the collision probability is given by⁽³³⁾

$$P_{ij} = \frac{2}{\pi(r_i^2 - r_{i-1}^2)} \left[\int_0^{\lambda_0} d\rho \{ K_{i3}(\lambda_0) - K_{i3}(\lambda_0 + \lambda_i) - K_{i3}(\lambda_0 + \lambda_j) + K_{i3}(\lambda_0 + \lambda_i + \lambda_j) \} \right], \quad i \neq j, \quad (2.32)$$

where λ_i and λ_j are the optical path lengths of the region i and j , respectively, λ_0 that between the regions i and j , and ρ the distance from the z -axis to the flight path. The $K_{i3}(\lambda)$ is the Bickley function defined by

$$K_{i3}(\lambda) = \int_0^{\frac{\pi}{2}} \sin^2 \theta \exp\left(-\frac{\lambda}{\sin \theta}\right) d\theta, \quad (2.33)$$

where θ is the angle between the flight path and the z -axis.

The collision probability for the case of $i=j$ is given by

$$P_{ii} = \frac{2}{\pi(r_i^2 - r_{i-1}^2)} \left[\int d\rho \{ \lambda_i - K_{i3}(0) + K_{i3}(\lambda_i) \} \right] . \quad (2.34)$$

For an isotropic boundary condition, the escape probability from the unit cell, P_{io} , corresponding to Eq.(2.29) for the slab cell, is written as follows:

$$P_{io} = \frac{2}{\pi(r_i^2 - r_{i-1}^2)} \left[\int d\rho \{ K_{i3}(\lambda_o) - K_{i3}(\lambda_o + \lambda_i) \} \right] . \quad (2.35)$$

2.4. Effective Cross Sections for Cell Calculations

The SLAROM code uses the JAERI Fast set with 70 group structure as the standard multi-group cross sections. This set gives effective cross sections from infinitely dilute cross sections and resonance shielding factors. For the homogeneous system, the effective cross sections are produced in the same manner as adopted in the EXPANDA 4 code.⁽³⁴⁾ In the resonance energy region of heavy mass nuclides, the resonance shielding factor is considerably influenced by the neighbouring materials or the cell geometry since there are usually several material regions in one mean free path length.

(1) Heterogeneity effect of resonance shielding factor

The heterogeneity effect on the resonance shielding can be considered by using the rational approximation. Theoretical works for this effect have recently been performed for multi-fuel region plate cells.⁽³⁵⁾ In the SLAROM code the approximate formula derived by Levine is adopted, where the effective admixture cross section (effective potential scattering cross section) σ_o^* is represented by

$$\sigma_o^* = \sigma_o + \frac{S_o}{4NV_o} \frac{(1-C)a}{1 + (a-1)C} \quad , \quad (2.36)$$

where a is the Levine factor, and S_o and V_o are the surface area and the volume of fuel region, respectively. The σ_o is the homogenized admixture cross section given by $\sigma_o = \sum_{j \neq i} \Sigma_t^j / N_i$. Though the Levine factor generally depends on the strength of each resonance, a constant value is usually adopted, that is, 1.20 ~ 1.25 for a plate cell and 1.30 for a pin cell.

For the Dancoff factor C , the following expression proposed by Meneghetti⁽³⁶⁾ is adopted:

$$C = E_3(\text{Sum}(\Sigma_t T)_k) + E_3(\text{sum}(\Sigma_t T)_\ell) , \quad (2.37)$$

where T is the thickness of the region k or ℓ . Each argument is the summation of the mean chord lengths over all the cell regions between the regions containing the nuclides of interest. Equation (2.37) has a convenient formula for neutron transport codes using the collision probability method, because such codes necessarily include the subroutine calculating the $E_n(x)$ function.

For the cylindrical cell, we use the Bell's approximation⁽³⁷⁾ for the Dancoff factor:

$$C = 1 - \gamma - \gamma^4(1 - \gamma)$$

$$\gamma = \frac{1}{1 + \Sigma_{e1}/\Sigma_1} , \quad \Sigma_{e1} = S_o / 4V_o , \quad (2.38)$$

where Σ_1 is the macroscopic cross section of the moderator.

In the fast reactor, the two-region (fuel and moderator) model may be satisfactory.

(2) Transport approximation

When the transport approximation is used, the mean chord length is calculated with use of the transport cross section Σ_{tr} , instead of Σ_t .

The transport cross section is defined as follows:

$$\Sigma_{tr}^i = \text{Sum}_j N_j \{ \bar{\sigma}_{a,j} + \bar{\sigma}_{in,j} + \bar{\sigma}_{n2n,j} + (1-\mu_j)\bar{\sigma}_{e,j} \} ,$$

$$\Sigma_{e,k \rightarrow k}^i = \text{Sum}_j N_j (1-\mu_j)\bar{\sigma}_{e,k \rightarrow k,j} , \quad (2.39)$$

where i stands for the region and j for nuclide. The $\Sigma_{e,k \rightarrow k}^i$ is the elastic scattering cross section from the group k to k . In other words, the above treatment corresponds to the diagonal transport approximation.

(3) Cell averaged effective cross section

The cell averaged effective cross sections are calculated by using the average neutron flux ϕ_i and the effective cross sections $\Sigma_{x,i}$ of each region, i.e.;

$$\langle \Sigma_x \rangle = \frac{\sum_i \Sigma_{x,i} V_i \phi_i}{\sum_i V_i \phi_i}, \quad (2.40)$$

where V_i is the volume of the region i , and the suffix X denotes the total, absorption, scattering or ν times fission reaction. The diffusion coefficient for the heterogeneous system is defined in different formulae by many workers. In SLAROM, we have adopted the definition by Benoist. (6) The isotropic diffusion coefficient is given by

$$D^I = \frac{1}{3} \frac{\sum_i \sum_j V_i \phi_i P_{ij} / \Sigma_{tj}}{\sum_i V_i \phi_i} \quad (2.41)$$

On the other hand, the anisotropic diffusion coefficient D_ℓ is represented as

$$D^\ell = \frac{1}{3} \frac{\sum_i \sum_j V_i \phi_i P_{ij}^\ell / \Sigma_{tj}}{\sum_i V_i \phi_i}, \quad (2.42)$$

and the average diffusion coefficient as

$$D^I = \frac{1}{3} \sum_\ell D^\ell, \quad (2.43)$$

where ℓ is the suffices for the coordinate axes. The P_{ij}^{ℓ} is the directional collision probability defined by

$$P_{ij}^{\ell} = \frac{3\Sigma_{tj}}{V_i} \int_{V_i} d\bar{r}' \int_{V_j} d\bar{r} \frac{e^{-\int_0^{|\bar{r}-\bar{r}'|} \Sigma_t(s) ds}}{4\pi |\bar{r}-\bar{r}'|^2} \Omega_{\ell}^2, \quad (2.44)$$

where Ω_{ℓ}^2 is explicitly given for the cylindrical coordinate

$$\Omega_r^2 = \frac{1}{2} \sin^2 \theta, \quad ,$$

$$\Omega_z^2 = \cos^2 \theta, \quad ,$$

and for the rectangular coordinate as

$$\Omega_x^2 = \sin^2 \theta \cos^2 \psi, \quad ,$$

$$\Omega_y^2 = \sin^2 \theta \sin^2 \psi, \quad ,$$

$$\Omega_z^2 = \cos^2 \theta. \quad .$$

For the transport approximation, the total cross section in Eqs.(2.41)

~ (2.44) should be replaced by the transport cross section.

2.5. Brief Description of SLAROM Code

The SLAROM code is programmed in FORTRAN 4 language for the FACOM 230/75 computer. The code includes eight segments in the overlay structure. The brief calculation flow is shown in Fig.2.1.

It may be divided into five steps between which data are transferred via temporary files. In each step, input data are read in the free format. At the first step (PREP), effective cross sections of each region are calculated and for the homogeneous case they are edited to the PDS file. In the second step (PATH), collision probabilities are computed and in the third step (PIJF), integral transport equation is solved. If the buckling search is required, the control returns to the PATH step and this loop continues until the convergence criteria are satisfied. With use of the converged flux, cell averaged effective cross sections and anisotropic diffusion coefficients are edited to the PDS file in the fourth step (EDIT). The final EIND step performs the one dimensional diffusion calculation and obtains collapsed multi-group cross sections for the multi-dimensional calculations if necessary.

These steps can be repeated for any times. At present, it is designed to use the EXTERMINATOR-2⁽³⁸⁾ or CITATION codes⁽³⁹⁾ for the multi-dimensional diffusion calculation, so the output formats of the collapsed cross sections are provided for them. The detailed description of SLAROM will be given in Appendix 1. We developed also the perturbation code, CIPER⁽⁸⁾ based on the 2 or 3-dimensional diffusion theory, which is devised to use the output flux and adjoint flux obtained from CITATION. The CIPER can treat the anisotropic diffusion as the perturbation and calculate the neutron streaming effect.

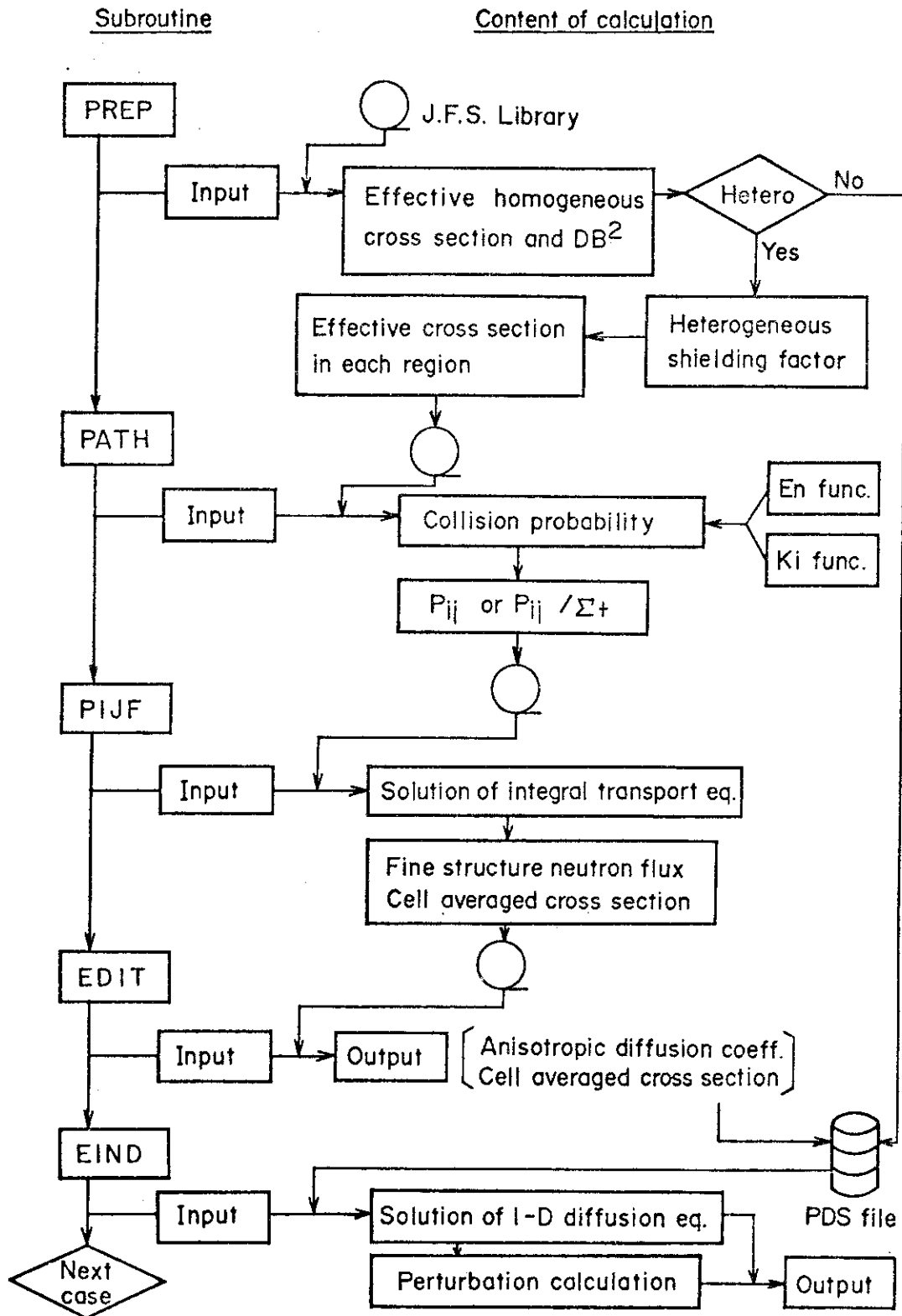


Fig.2.1 SLAROM calculation flow

3. Multi-group Cross Section Generation Method by Using Fine Group

Fundamental Mode Spectrum in Slab Cell

3.1. Introduction

The multi-group treatment has usually been used for transport or diffusion calculations in the design study of fast reactors and in the analysis of experiments at fast critical assemblies. The accuracy of these multi-group calculations strongly depends on the generating method of the multi-group cross sections. One typical type of the multi-group cross sections is the tabulated constant set such as the YOM⁽⁴⁰⁾ and ABBN⁽⁴¹⁾ sets. The JAERI Fast set^{(9),(10)} has been produced as this type of cross section set based on a more advanced concept. When the JAERI Fast set is produced, the fission plus 1/E spectrum is used as the weighting function for infinitely dilute media to average microscopic pointwise cross sections for light elements, and an exact ultra fine spectrum is used in the resonance energy region for heavy elements. The composition dependency of the group cross sections is taken into consideration by using a $1/(\sigma_t + \sigma_o)$ spectrum as the weighting function. The effective cross sections are then obtained from the tabulated infinitely dilute cross sections and the resonance shielding factors given as a function of temperature and admixture cross section σ_o . In this type of cross sections, the weighting spectrum used is not the true spectrum in a real reactor and hence the elastic scattering resonances are not adequately treated for light and medium weight elements. That is, the influence from the resonances of another elements can not be taken into consideration because of the assumption of the constant background cross section. Another defect comes from the fact that the self-shielding factors for elastic removal cross sections are assumed to have the same values as for elastic scattering cross sections of light and intermediate nuclei. This is known to cause a significant inaccuracy in

the calculation of elastic removal cross sections in the vicinity of the large resonance regions. The EXPANDA-75⁽⁴²⁾ code, which uses the JAERI Fast set library, is devised to treat analytically the resonance region near 2.85 keV of sodium to overcome this defect. However, the applicable range of this treatment is limited to that resonance.

The heterogeneity effect is significant in the analysis of experiments in fast critical assemblies. Among the codes utilizing the JAERI Fast set, the SLAROM⁽³⁰⁾ and EXPANDA-75 codes solve the integral transport equation for heterogeneous cell to obtain the cell averaged cross sections and perform diffusion calculations. However, since these codes essentially start from a broad group cross section set, the defects mentioned above can not be overcome. Consequently, a computer code is required to obtain a fine spectrum with composition dependency in heterogeneous systems and to generate accurate multi-group cross sections. In order to overcome such defects, the ESELEM⁽²⁷⁾ code series has been developed and used to study a suitable production method of group constant set. The ESELEM 4 code has been the first version developed for obtaining the effective cross sections weighted by the composition dependent fine spectrum with heterogeneity effects for a plate lattice. This code has a close relation with the JAERI Fast set concerning with the cross section data and hence supports the code system utilizing the JAERI Fast set. The latest version is ESELEM 5 which is improved in an accuracy and in a computation time.

Several codes have already been developed to calculate fine group neutron spectrum and to produce multi-group cross sections. ELMOE⁽⁴³⁾ is a representative code at the first stage to study the fine spectrum effect due to the scattering resonances of light elements. MC²⁽²⁰⁾ has a more general capability to produce the multi-group cross sections. In the revised version, MC²-2,⁽²⁵⁾ advanced methods are incorporated for the

calculation of unresolved resonance cross sections, heterogeneity effects and continuous slowing down process. These codes calculate the fundamental mode flux but do not treat explicitly the heterogeneity effects for multi-region cell. On the other hand, the MURALB⁽²⁶⁾ code solves multi-group transport equations for heterogeneous systems with 1/128 lethargy width. This code treats the resonance heterogeneity effect by the histogram method. However, MURALB is not available for us at present. The similar fine group spectrum code is incorporated in the DOYC code system⁽⁴⁴⁾ which is used to obtain the AGLI data library by adjusting cross sections so as to predict integral experiment data. The DOYC method for solving slowing down equations is based on that in the ESELEM 2⁽²⁷⁾ code and the resonance heterogeneity is treated on the basis of MURALB method.

In this chapter, the numerical formulation and the calculational algorithm are described for the ESELEM 5 code. This code computes the fine spectrum in the heterogeneous plate cell (including a homogeneous system) by solving the integral transport equation with the use of the collision probability method and generates the multi-group cross sections for an arbitrary group structure. The treatment of resonance heterogeneity effect in ESELEM 4 and 5 is different from the histogram method used in MURALB and DOYC. In our programme the heterogeneity effect is taken into account by using modified admixture cross sections with the Dancoff factors calculated for multi-region cells.

The reduction of computation time and core storage is an important problem for these fine group calculation programmes. In the ESELEM 4, 5 code the following devices are adopted for it. The very efficient recurrence formula is used in the calculation of elastic and inelastic slowing down sources for saving computation time and data storage. Moreover, the broad group treatment is adopted in ESELEM 4 above 2 MeV since the calculation

of inelastic slowing down source is very time consuming. As the cross section is comparatively smooth in this energy region, this treatment does not lead to serious errors. On the other hand the preparation of the library is slightly troublesome, so in ESELEM 5, the fine group treatment is adopted in all energy range at the expense of computation time. The broad group representation is used also for the resonance region, where the cross sections of the JAERI Fast set are adopted for heavy elements. These take into account self-overlapping and interference effects between resonances. For saving the computer core area the cross sections are compactly stored in the fast core memory. Therefore the data processing time becomes short and the flexibility is provided for the maximum numbers of cell regions and spacial meshes used for solving problems.

The nuclear cross section library is prepared by the PRESM code from the general nuclear data file with ENDF/A or ENDF/B type format. The same source nuclear data as for the JAERI Fast set is used at present.

The basic equation to be solved in ESELEM 4 and 5 is the integral transport equation as the same as the SLAROM code mentioned in Chapter 2. Though the group width is very narrow, the solution method is, essentially, based on the multi-group method. The spatial distribution of neutron flux is obtained by using the collision probability method, so its explanation is suppressed in this chapter. The slowing down source is calculated by using the scattering matrix in the broad group method, but in the ESELEM code more efficient method is adopted as explained in the following.

The detailed description of the ESELEM 5 code is given in Appendix 2 where its library preparation code, PRESM is explained.

3.2. Recurrence Formula for Slowing Down Equation

The slowing down source from higher energy groups comes both from the elastic and inelastic scattering at discrete and continuum levels. For the multigroup treatment the slowing down source is usually calculated with the use of scattering matrix or probability for elastic and inelastic scattering. If this method is used for the fine group calculation, large computer core memory is required for the inelastic scattering matrix in addition to a long computation time. If the recurrence formula is applied to the source calculation, the scattering matrix becomes unnecessary and hence the storage used for the scattering matrix is saved. As a result of this, the source calculation becomes very simple as explained below.

The recurrence formula is often adopted to solve an ultra-fine group problem in resonance energy region of heavy mass elements, as used in the RABBLE⁽⁴⁵⁾ and ERSE⁽⁴⁶⁾ codes. In these codes only the elastic slowing down with isotropic scattering in the center-of-mass system is calculated by the recurrence formula, since these codes are developed to treat the resonance energy region below several tens keV. The contribution from self-group scattering is negligible for so fine group width as to treat the resonance region. In the ESELEM 5 code we use recurrence relations for P_0 and P_1 component of elastic scattering, and also for inelastic scattering, where we take account approximately of the self-group scattering which should not be neglected except for the light mass nuclides, because the slowing down groups are only two or three groups for heavy mass nuclides.

1. Elastic Slowing Down

The slowing down source due to elastic scattering with mass number A at lethargy u can generally written, in infinite homogeneous medium, as

$$S^A(u) = \int_{u-\eta_A}^u \Sigma_S^A(u' \rightarrow u) \phi(u') du', \quad (3.1)$$

with

$$\eta_A = \ln 1/\alpha_A, \quad \alpha_A = \left(\frac{1-A}{1+A}\right)^2.$$

The scattering transfer cross section $\Sigma_S^A(u' \rightarrow u)$ can be expanded in a set of Legendre polynomials, i.e.,

$$\Sigma_S^A(u' \rightarrow u) = \frac{e^{u'-u}}{1-\alpha_A} \sum_{\ell=0}^{\infty} \Sigma_{\ell}^A(u') B_{\ell}(\mu_c^A) \quad (3.2)$$

with

$$\mu_c^A = 1 - \frac{(A+1)}{2A} (1 - e^{u'-u}) \quad (3.3)$$

The expansion of Eq.(3.2) are inserted into Eq.(3.1) and truncated after the first two terms, i.e., by making the P_1 approximation, it is found that

$$S^A(u) = \frac{1}{1-\alpha_A} \int_{u-\eta_A}^u e^{u'-u} (\Sigma_0^A(u') + \Sigma_1^A(u') \mu_c^A) \phi(u') du' \quad (3.4)$$

If the scattering is isotropic in the center-of-mass system (this assumption is good below about 100 keV), we have the equation:

$$S^A(u) = \frac{1}{1-\alpha_A} \int_{u-\eta_A}^u e^{u'-u} \Sigma_0^A(u') \phi(u') du' \quad (3.5)$$

The slowing down source in the group i is assumed to be the average of the values at the upper and lower group boundaries, that is,

$$S_i^A = \frac{S_i^A(u_U^i) + S_i^A(u_L^i)}{2}, \quad (3.6)$$

where u_U^i and u_L^i are the lethargies at the upper and lower boundaries of the group i , respectively. Then the contribution to $S_i^A(u_L^i)$ from the higher groups is obtained from Eq.(3.5) as

$$S_i^A(u_L^i) = \int_{u_L^{i-\eta_A}}^{u_L^i} \frac{e^{u'-u} \Sigma_0^A(u') \phi(u') du'}{1-\alpha_A}$$

$$= \sum_{\ell=1}^{L_A} P_{\ell,A} \Sigma_{0,i-\ell}^A \phi_{i-\ell} \quad , \quad (3.7)$$

where $P_{\ell,A}$ is defined by

$$P_{\ell,A} = \frac{1}{1-\alpha_A} e^{-(\ell-1)\Delta u} (1 - e^{-\Delta u}) \Delta u \quad (3.8)$$

which is the probability that a neutron is scattered down ℓ groups by elastic scattering collision with nucleus A. The $\Sigma_{0,i-\ell}^A$ is the macroscopic scattering cross section in group $(i-\ell)$, and L_A is the maximum number of slowing down groups. Here, the cross section and the flux has been assumed to be flat within the group with a lethargy width of Δu . By using the relation $P_{\ell,A} = e^{-\Delta u} P_{\ell-1,A}$, Eq.(3.7) can be transformed to the following recurrence formula:

$$S_i^A(u_L^i) = P_{1,A} \Sigma_{0,i-1}^A \phi_{i-1} + e^{-\Delta u} \{ S_{i-1}^A(u_L^i) - P_{L_A,A} \Sigma_{0,i-L_A-1}^A \phi_{i-L_A-1} \} \quad (3.9)$$

The calculation of $S_i^A(u_L^i)$ becomes much simpler with this equation than Eq.(3.7) when the mass number is smaller. When we take the summation over all nuclei contained in the medium, the total slowing down source $S_i(u_L^i)$

is obtained as follows:

$$S_i(u_L^i) = \sum_A P_{1,A} \Sigma_{0,i-1}^A \phi_{i-1} + e^{-\Delta u} [S_{i-1}(u_L^i) - \sum_A P_{L_A,A} \Sigma_{0,i-L_A-1}^A \phi_{i-L_A-1}] \quad (3.10)$$

The source $S_i(u_U^i)$ at the upper lethargy boundary can be written in the similar form by noting that the self-group scattering contributes it but not the $(i-L_A-1)$ th group:

$$S_i(u_U^i) = \sum_A P_{1,A} \Sigma_{0,i}^A \phi_i + e^{-\Delta u} [S_{i-1}(u_U^i) - \sum_A P_{L_A,A} \Sigma_{0,i-L_A}^A \phi_{i-L_A}] \quad (3.11)$$

Accordingly, the average elastic slowing down source into the group i is obtained from Eq.(3.6) as follows:

$$S_i = \frac{S_i(u_L^i) + S_i(u_U^i)}{2}$$

In the case of light mass nuclides, such as oxygen and sodium, the anisotropy of scattering in the center-of-mass system can not be neglected in the higher energy region. To reflect the anisotropic effect on neutron flux, we derive the recurrence formula for the P_1 term of Legendre expansion by the similar method used for the P_0 (isotropic) term.

Rearranging the integrand of Eq.(3.4) on the powers of $\exp(u'-u)$, the slowing down source due to the P_1 term, $S_1^A(u)$ can be written as

$$S_{1}^A(u) = \frac{1}{1-\alpha_A} \int_{u-\eta_A}^u e^{u'-u} \left[1 - \frac{(A+1)^2}{2A} \Sigma_1^A(u') \right] \phi(u') du' + \frac{2}{(1-\alpha_A)^2} \int_{u-\eta_A}^u e^{2(u'-u)} \Sigma_1^A(u') \phi(u') du' \quad (3.12)$$

Since the first term of Eq.(3.12) has the same form as Eq.(3.5) except the constant factor, it can be calculated with use of the same recurrence relation as the P_0 term. The second term is presented by the transfer probability, P_ℓ^1 , for the fine group i as,

$$S_{i,1}^A = \sum_{\ell=1}^{L_A} P_\ell^1 \Sigma_{1,i-\ell}^A \phi_{i-\ell} \quad (3.13)$$

The recurrence formula for $S_{i,1}^A$ can be derived as follows:

$$P_\ell^1 = \int_{u_0}^{u_0+\Delta u} du \int_{u_0-\ell\Delta u}^{u_0-(\ell-1)\Delta u} du' e^{2(u'-u)} \quad (3.14)$$

By performing integration, we obtain

$$P_\ell^1 = \frac{1}{4} (1 - e^{-2\Delta u})(1 - e^{-2\Delta u})e^{-2(\ell-1)\Delta u} \approx \frac{1}{2} \Delta u (1 - e^{-2\Delta u})e^{-2(\ell-1)\Delta u} \quad (3.15)$$

Therefore, the recurrence relation of P_ℓ^1 and $S_{i,1}^A$ can be written as

$$P_{\ell+1}^1 = e^{-2\Delta u} P_\ell^1, \quad (3.16)$$

$$S_{i,1}^A = P_1^1 \Sigma_{1,i-1}^A \phi_{i-1} + e^{-2\Delta u} \{ S_{i-1,1}^A - P_{L_A}^1 \Sigma_{i,i-L_A-1}^A \phi_{i-L_A-1} \}$$

Consequently, the slowing down equation including up to the P_1 term of scattering cross section can finally be written as follows:

$$\begin{aligned}\Sigma_{t,i}\phi_i &= S_{i,0} + S_{i,1} \\ S_{i,0} &= \sum_A P_1^0 \Sigma_{Q,i-1}^A \phi_{i-1} + e^{-\Delta u} \{ S_{i-1,0} - \sum_A P_{L_A}^0 \Sigma_{Q,i-L_A-1}^A \phi_{i-L_A-1} \} \\ S_{i,1} &= \sum_A P_1^1 \Sigma_{1,i-1}^A \phi_{i-1} + e^{-2\Delta u} \{ S_{i-1,1} - \sum_A P_{L_A}^1 \Sigma_{1,i-L_A-1}^A \phi_{i-L_A-1} \}\end{aligned}\quad (3.17)$$

with

$$\Sigma_{Q,i-1}^A = \Sigma_{0,i-1}^A + \Sigma_{1,i-1}^A \left[1 - \frac{(A+1)^2}{2A} \right]$$

Since the first term of Eq.(3.12) is as the same form as Eq.(3.7) except the constant factor, P_{ℓ}^0 is also given by Eq.(3.8). The above equations show that the neutron flux can be easily obtained by the similar algorithm used for Eq.(3.10) or (3.11) corresponding to the P_0 approximation.

2. Inelastic Slowing Down

(1) Discrete level contribution

When the isotropic scattering is assumed for the inelastic scattering, the energy transfer probability from E' to E is presented by the equation

$$P(E' \rightarrow E) dE' = \frac{dE'}{(E_{\max} - E_{\min})} \quad , \quad (3.18)$$

where E_{\max} and E_{\min} are respectively the maximum and minimum slowing down energy defined by

$$\begin{aligned}E_{\max} &= \frac{A^2+1}{(A+1)^2} E' - \frac{A}{A+1} \epsilon + \frac{2A}{(A+1)^2} \sqrt{E'^2 - \frac{A+1}{A} \epsilon E'} \quad , \\ E_{\min} &= \frac{A^2+1}{(A+1)^2} E' - \frac{A}{A+1} \epsilon - \frac{2A}{(A+1)^2} \sqrt{E'^2 - \frac{A+1}{A} \epsilon E'} \quad .\end{aligned}\quad (3.19)$$

In this equation, ϵ stands for the excitation energy of the discrete level of nucleus A, that is, ϵ is equal to $-Q$. Equation (3.18) can be discretized for the scattering from the group i to j as follows:

$$P(i \rightarrow j) = \frac{1-R}{1-R \frac{n_j^{-m_j+1}}{n_j^{-m_j}}} R^{(j-i-m_j)}, \quad (3.20)$$

where

$$m_j = \left[\ln \frac{E'}{E_{\max}} / \Delta u \right],$$

$$n_j = \left[\ln \frac{E'}{E_{\min}} / \Delta u \right],$$

$$R = e^{-\Delta u}, \quad \Delta E = E'(1-R).$$

Since the slowing down source to the group i consists of the contributions from all the discrete levels, we can write

$$S_j^A = \sum_{\text{level } i=j-m_j}^{\sum_j^{j-n_j} A} \frac{1-R}{1-R \frac{n_j^{-m_j+1}}{n_j^{-m_j}}} R^{j-i-m_j} \sum_i^A \phi_i, \quad (3.21)$$

where \sum_i^A is the macroscopic inelastic cross section of discrete levels in group i . If the m_j is zero, S_j^A includes the source due to the self-group scattering. From Eq.(3.21) the source at the group $j+1$ can be written in the following recurrence formula:

$$\begin{aligned} S_{j+1} &= \sum_{\text{level } i=j+1-m_j}^{\sum_j^{j-n_j+1}} \frac{1-R}{1-R \frac{n_j^{-m_j+1}}{n_j^{-m_j}}} R^{j+1-i-m_j} \sum_i \phi_i \\ &= \sum_{\text{level } j} (RS_j + \frac{1-R}{1-R \frac{n_j^{-m_j+1}}{n_j^{-m_j}}} \sum_{j+1-m_j} \phi_{j+1-m_j} \\ &\quad - \frac{1-R}{1-R \frac{n_j^{-m_j+1}}{n_j^{-m_j}}} R^{n_j^{-m_j}+1} \sum_{j-n_j} \phi_{j-n_j}) \end{aligned}$$

, where we suppressed the suffix A for convenience.

If we denote $\sum_{\text{level } j} S_j$ simply by S_j , we have

$$S_{j+1} = e^{-\Delta u} S_j + \sum_{\text{level } j} \frac{1-R}{1-R} \frac{n_j^{-m_j+1}}{n_j^{-m_j+1}} \sum_{j+1-m_j} \phi_{j+1-m_j} - \frac{1-R}{1-R} \frac{n_j^{-m_j+1}}{n_j^{-m_j+1}} R \sum_{j-n_j} \phi_{j-n_j} \quad (3.22)$$

(2) Continuum level contribution

The neutron energy distribution due to the scattering by the continuum level is assumed to be approximately given by using the evaporation model. That is, the transfer probability is presented by

$$P(E' \rightarrow E) = bE e^{-E/a\sqrt{E'}} \quad (3.23)$$

where b is a normalization factor and a is a constant. When the probability is normalized between E_0 and E_1 , we have

$$b = 1/a\sqrt{E'} \left\{ \exp\left(-\frac{E_0}{a\sqrt{E'}}\right) (a\sqrt{E'} + E_0) - \exp\left(-\frac{E_1}{a\sqrt{E'}}\right) (a\sqrt{E'} + E_1) \right\}^{-1}$$

In this case, the transfer probability from the group i to j is written in the discrete form:

$$P(i \rightarrow j) = bE_j e^{-E_j/a\sqrt{E_i}} \Delta E_j \Delta E_i$$

The recurrence relation is then obtained as follows:

$$P(i \rightarrow j+1) = P(i \rightarrow j) e^{-\Delta E_j/a\sqrt{E_i}} \frac{E_{j+1}}{E_j} \frac{\Delta E_{j+1}}{\Delta E_j} = P(i \rightarrow j) \frac{1+\Delta E_j/2T_i}{1-\Delta E_j/2T_i} R^2 \quad (3.24)$$

for which we have used the following approximations;

$$\frac{E_{j+1}}{E_j} \frac{\Delta E_{j+1}}{\Delta E_j} = \left(\frac{E_{j+1}}{E_j}\right)^2 = R^2$$

and, denoting $\sqrt{E_i}$ by T_i and using the relation $\Delta E_j \ll T_i$,

$$e^{-\Delta E_j/T_i} = 1 + \frac{\Delta E_j}{T_i} + \left(\frac{\Delta E_j}{T_i}\right)^2 + \dots \approx \left(1 + \frac{\Delta E_j}{2T_i}\right)^2$$

$$\approx \frac{1 + \Delta E_j/2T_i}{1 - \Delta E_j/2T_i}$$

Therefore, from Eq.(3.24) the slowing down source is obtained by

$$S_j = \sum_{i=j}^1 P(i \rightarrow j) \sum_i \phi_i$$

$$= \sum_{i=j-1}^1 P(i \rightarrow j-1) \frac{1 + \Delta E_{j-1}/2T_i}{1 - \Delta E_{j-1}/2T_i} R^2 \sum_i \phi_i, \quad (3.25)$$

where the summation over i is taken from the highest group to the threshold group when E_j is below the threshold energy. The self-scattering term is neglected in the calculation of S_j but it is considered after the flux ϕ_j is obtained for the use of the S_{j+1} calculation. As we have shown above, the transfer probability can be calculated with the use of recurrence formula but the slowing down source can not be represented by recurrence relation. Hence much computation time will be needed for the calculation of the slowing down source due to the continuum level.

(3) (n,2n) contribution

The secondary neutron energy distribution due to the (n,2n) reaction is also assumed to be given by using the evaporation model. Hence the

transfer probability is presented by Eq.(3.23) and the slowing down source, S_j^{2n} can be written by slightly modifying Eq.(3.25) as follows:

$$S_j^{2n} = 2 \sum_{i=j-1}^1 P(i \rightarrow j-1) \frac{1 + \Delta E_{j-1}/2T_i}{1 - \Delta E_{j-1}/2T_i} R_{\Sigma_i}^{2n} \phi_i, \quad (3.26)$$

where $P(i \rightarrow j-1)$ is defined in Eq.(3.24).

3.3. Nuclear Data Treatment

1. Fission spectrum and released fission neutron number

The fission spectrum is given by the Maxwell distribution function:

$$\chi(E) = \frac{2}{\sqrt{\pi}} \left(\frac{E}{T}\right)^{1/2} \frac{1}{T} \exp\left(-\frac{E}{T}\right), \quad (3.27)$$

where T denotes a nuclear temperature, which is given in the library data. The group averaged fission spectrum is calculated at the every fine group energy.

The released fission neutron number $\nu(E)$ is presented by the polynomial,

$$\nu(E) = b_0 + \sum_{\ell=1}^n b_{\ell} E^{\ell} \quad (3.28)$$

In the present code the coefficient b_{ℓ} can be given up to the fifth term for each fissionable nuclide.

2. Fine group data management

The fine group cross section in the library is arranged in the descending order of energy. The data include energy, elastic scattering, absorption, fission, (n,2n), inelastic scattering for each discrete level and inelastic scattering cross sections for a continuum level. As the fine group calculation proceeds, these data at the corresponding fine group are successively transferred to the core memory. The cross section of a fine group is obtained by averaging point-wise cross sections in the group width with an 1/E spectrum. The cross sections are then obtained by the linear interpolation in the log-log scale as explained below. We write the energy and cross section at the n-th point as (E_n, σ_n) . The gradient of the cross

section curve is presented in the log-log scale as

$$A_n = \ln (\sigma_n / \sigma_{n+1}) / (u_{n+1} - u_n) , \quad (3.29)$$

where u_n and u_{n+1} are the lethargies corresponding to energy E_n and E_{n+1} , respectively. Therefore the cross section at energy E is given by

$$\sigma(E) = \sigma_n \exp[A_n(u - u_n)] .$$

When the fine group i lies in the interval between E_n and E_{n+1} as shown in Fig.3.1(a), the average cross section of the group i is given by

$$\begin{aligned} \langle \sigma_i \rangle &= \frac{\int_{\Delta E_i} \sigma(E) \cdot 1/E \, dE}{\int_{\Delta E_i} 1/E \, dE} \\ &= \frac{1}{A_n \Delta u} \{ \sigma(u_{i-1}) - \sigma(u_i) \} , \end{aligned} \quad (3.30)$$

where Δu is the fine group lethargy width. When $|A_n|$ is very small, Eq.(3.30) can be approximated by

$$\langle \sigma_i \rangle = \sigma(u_i) \quad (3.31)$$

The criteria is set as $|A_n| < 0.01$ in the code. If k energy points are included in the fine group i as shown in Fig.3.1(b), the average cross section is represented by

$$\begin{aligned} \langle \sigma_i \rangle &= \left\{ \frac{\sigma(u_{i-1}) - \sigma(u_{n+1})}{A_n} + \sum_{j=1}^k \frac{\sigma(u_{n+j}) - \sigma(u_{n+j+1})}{A_{n+j}} \right. \\ &\quad \left. + \frac{\sigma(u_{n+k}) - \sigma(u_{n+k+1})}{A_{n+k+1}} \right\} / \Delta u \end{aligned} \quad (3.32)$$

In the resonance region of heavy mass nuclides the resonance self-shielding effect is very important. For example there exist several resonances of ^{238}U in the fine group lethargy width of 0.0084 about 10 keV and more for ^{235}U or ^{239}Pu . Therefore it should be necessary to use an ultra fine group structure of about 0.0001 lethargy width if we want to use infinitely dilute cross sections. However this method is very time consuming. In ESELEM 5 we, therefore, adopt the broad group cross sections and their shielding factors taken from the JAERI Fast set. As noted in Ref.(10), the broad group treatment for heavy mass nuclides is considerably good for the group width of 0.25. Moreover the resonance self-overlap and mutual-shielding effects have been taken into consideration in this set.

The heterogeneity effect on the resonance shielding is taken into consideration by using the rational approximation mentioned in Chapter 2. That is, the effective admixture cross section, σ_0^* is given by Eq.(2.36) and the Dancoff factor C for the plate cell is defined by Eq.(2.37).

When the broad group cross section is used, we should note that the discontinuities of the cross sections appear at the group boundaries. This sometimes causes sharp peaks or dips to the neutron spectrum. Especially, such a fact is remarkable in the resolved resonance region of heavy mass nuclides since the difference of cross sections between neighbouring broad groups is very large. To avoid such a defect, we use a linear interpolation of the cross sections, which interpolates the broad group values over a few fine group widths on both the sides of the broad group boundary. Since the discontinuities are large for fertile materials, this effect is noticeable in the blanket region. Nevertheless, it may not be a serious problem for fast reactors because such a problem appears below about 100 eV.

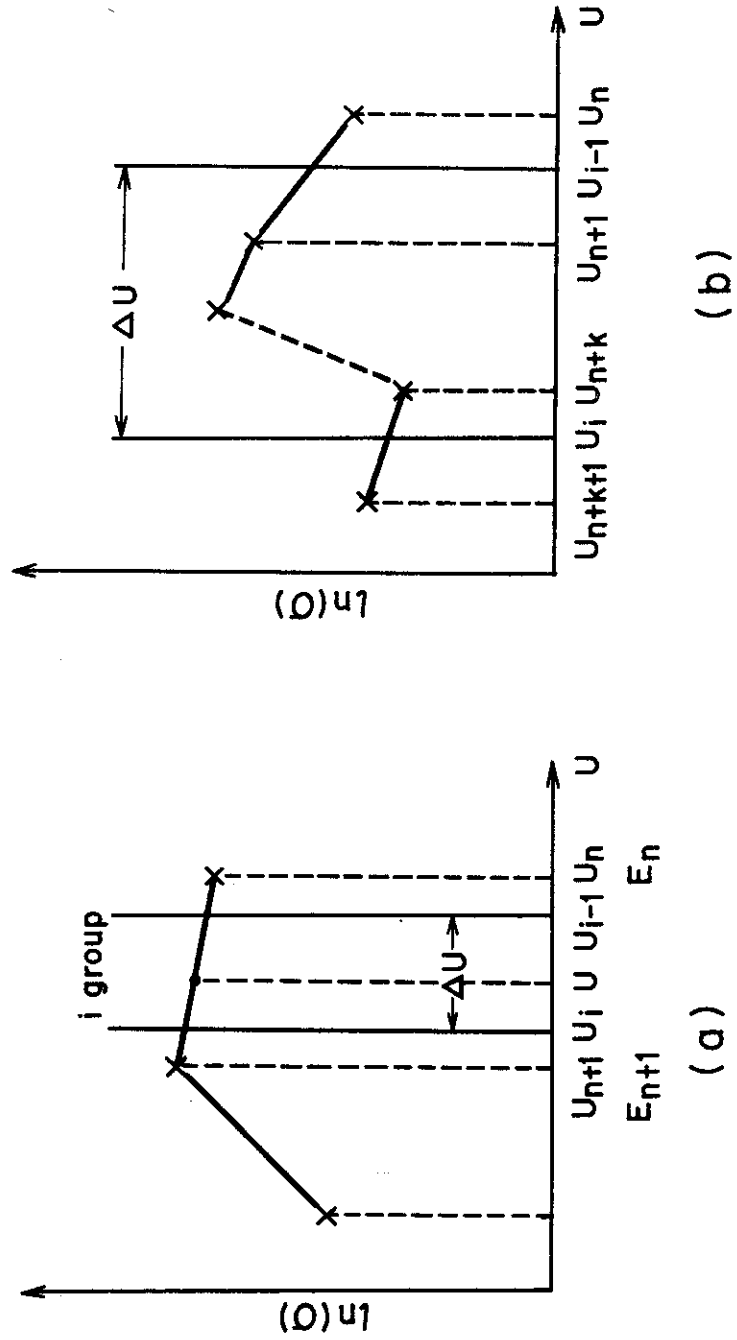


Fig.3.1 Interpolation scheme of point cross section

4. Analysis of Sodium Void Reactivity Measurements in Fast Critical Assemblies with Broad Group Constant Sets

4.1 Analysis of FCA V-1 Assembly

4.1.1 Introduction

The analysis of sodium void reactivity measurements has been performed. The measurements were made in FCA assembly V-1⁽¹¹⁾, which is a physics mock-up of the Japan Experimental Fast Reactor "JOYO".

Sodium void reactivity is the subject of main interest for measurements in a fast critical assembly, and various measurements⁽⁴⁷⁾ and analyses of the results⁽¹⁹⁾ have been performed in such assemblies as ZPR, ZEBRA and ZPPR. More recently, interest has been focused on measurements of dilute or soft spectrum systems. In the analysis of these soft spectrum systems the methods of calculation in resonance region become important. The FCA assembly V-1 has a small core volume and a hard neutron spectrum, so that the leakage will contribute the principal element in sodium void reactivity, and the treatment of the resonance region will not occasion significant inaccuracies. For example, the heterogeneity effect on resonance self-shielding factors will not affect the reactivity to any significant degree.

On the other hand, since the FCA assembly consists of a heterogeneous arrangement of plate type fuels and moderators, the streaming effect along the plate surface is considered very important. Sodium void measurements are necessarily affected by the streaming effects in the assemblies consisting of plate type fuels. Most loading patterns for sodium void measurements have been arranged to minimize the streaming effects since analysis of these effects is complicated. Measurements concerning streaming effect itself have been performed in ZPR and ZEBRA. The measurements in ZEBRA⁽⁴⁸⁾, yielded negative coefficients in vertical plate cells twice as large as in the horizontal plate cells in the region, 15.2 - 45.7 cm of the central channel. Some measurements were also made in ZPR-VI⁽⁴⁷⁾ with similar results

indicating the importance of the streaming effects.

However, the streaming effects have not yet been taken into considerations adequately in the analysis of sodium void reactivity, and thus has caused large and systematic discrepancies between calculations and measurements in the analysis of FCA V-1. A measurement has been performed in the central channel in the assembly V-1, which showed that the axial streaming effects contributes more than 17 percents of the total void reactivity. However, this measurement does not appear to represent properly the neutron streaming effect due to limitations imposed by the plate arrangements. It goes without saying that the radial dependence of the streaming effect should be considered in the range of large voids.

The heterogeneity effect in a hard spectrum core will be dominant in the high energy region, due to the heterogeneity of the fission source. When the spectrum component is relatively small, this effect may be unimportant, but in the central region it will become significant.

Another reason for the discrepancies between calculations and measurements comes from uncertainties in the cross sections used and in the methods used for group averaging. The elastic removal cross sections significantly affect the spectrum term of reactivity through the spectrum shift caused by sodium voiding, and these group cross sections, given for instance in the ABBN⁽⁴¹⁾ and JAERI Fast⁽⁹⁾ sets will no longer be accurate enough, particularly around the resonances of light and medium-weight elements^{(23), (24)}.

The analysis of sodium void reactivity is very complicated as already mentioned; better consistency in the results is difficult to obtain. If we can succeed in applying a better interpretation, the result will be profitable for considering the accuracy of cross sections in certain restricted energy ranges. In what follows, we will summarize our studies for obtaining better interpretation by considering the streaming effect and cell

heterogeneity.

4.1.2 Summary of measurements

The core of the FCA assembly V-1 is of cylindrical shape, 28.7 cm in radius and 61 cm high, surrounded by a natural uranium blanket 30 cm thick. The core consists of channel drawers and structural materials. The cross section of each channel is a square of 5.52 cm \times 5.52 cm. Plate-type fuel, sodium and structural materials are arranged in appropriate order in each channel drawer. The fuel is composed of Pu and 20 % enriched uranium.

Sodium void reactivities were measured for many loading patterns. For convenience, the measurements can be classified into two categories: (A) measurements performed at the center of core and (B) those on channels voided throughout the core along the axial direction. For category B, the experiments, S-1 ~ S-6 were measurements with a voided single channel drawer, S-1 being that with the voided channel at the core center and S-2 ~ S-6 those with the channel successively removed forward the radial core boundary. In the experiments M-1, 2, 3 the voided regions were distributed in checker board pattern, as shown in Fig. 4.1.1, where the voided channels are indicated by shading. All patterns are symmetric in reference to the midplane along the core axis.

Measurements in the category A were performed by removing sodium regionally from the nine central channels, constituting a square of 16.56 cm \times 16.56 cm.

4.1.3 Calculational methods

(1) Reference calculations

Reference calculations for the non-voided reference core and sodium voided core have been performed by one- and two-dimensional diffusion codes.

Using the one dimensional diffusion code EXPANDA-70D⁽⁴⁹⁾, six group cross sections were produced from JAERI Fast set. The boundary energies of 1.4 MeV, 400 keV, 100 keV, 10 keV, 1 keV and 0.215 eV were chosen for the lower group. The collapsed cross section were obtained for three regions in the core and two regions in the blanket. Two-dimensional calculations were performed using the code EXTERMINATOR-2⁽³⁸⁾ and CITATION⁽³⁹⁾ for X-Y and R-Z geometry. The EXTERMINATOR-2 code was modified for calculations of axial buckling and anisotropic leakage components in perturbation routine. The axial buckling for each channel drawer voided, as well as non voided, was obtained from the two-dimensional calculations, in such manner as to conserve the leakage at the boundary between the core and blanket. As a result, criticality factors for standard core showed very good agreement between R-Z and X-Y calculations (1.00461 and 1.00459 respectively). The collapsed cross sections obtained to the reference core were used for the voided cores except in the voided region.

The JAERI Fast set with 70 group structure was used instead of that with 25 group, throughout the present analysis. The difference in the criticality factors due to these two different group structures was about 0.65 % $\Delta K/K$ for the standard core, and the difference was significant also for the sodium void reactivity as will be discussed later. Since these differences are maintained in the collapsed six group calculations, it was judged preferable to use the 70 group structure as standard set.

(2) Calculation of streaming and heterogeneity effects

The discrepancy between diffusion calculations and measurements is large in the central channel of the core and gradually decrease as the channel approaches the core boundary as shown in Table 4.1.1. This tendency is also confirmed by another independent work⁽⁵⁰⁾ in which different group

constants are used. This naturally leads to the conclusion that this discrepancy is not attributable to the group constants used but to the calculational methods. When we assume that the leakage component is the main contributor to the reactivity in the regions voided throughout the channels, and consider the tendency, mentioned above of greater discrepancy toward core center, we naturally come to suspect inadequate treatment of the leakage component in the axial direction as the cause for this discrepancy between calculation and measurement. For a critical assembly with plate structure of materials such as FCA, the parallel directional neutron streaming may be considerable especially when a void region exists throughout the channel.

This streaming effect is taken into consideration by introducing anisotropic diffusion coefficients, defined by Eq. (2.42).

Calculations taking account of the heterogeneous arrangement of the plates are performed for an eight-region cell with infinite length as shown in Fig. 4.1.2. The casing stainless steel is homogenized in each material and the structural materials at the upper lower extremities are homogeneously diluted in the cell. The SLAROM code is used for the calculations of directional collision probabilities and cell averaged effective cross sections. The diffusion coefficients are calculated at several void fractions of sodium. In Fig. 4.1.3 is shown the parallel directional diffusion coefficients $D_{//}$ for a six-group structure collapsed from those of the 70 group. The values of $D_{//}$ vary almost linearly with void ratio except at 100 percents void. The same trend is observed for the perpendicular diffusion coefficients, D_{\perp} .

When the void ratio is 100 percents, Σ_t of the sodium region becomes very small (not zero on account of the homogenized stainless steel), and in this case then the approximation for the directional collision probability may be poor. When Σ_t is small in region i , the collision probability P_{ii}

is given by function $E_1(\lambda)$, where λ is optical path length. Since $E_1(\lambda)$ displays a logarithmic singularity at $\lambda=0$, the approximation of $E_1(\lambda)$ becomes inaccurate in the range of small Σ_t . Following the usual practice, the collision probability is multiplied by source strength: $\Sigma_x \phi$ (Σ_x is a scattering or a fission cross section), $\Sigma_x P_{ij}$ tends to zero for a small value of Σ_t . But directional collision probability P_{ij}^k is given by P_{ij}/Σ_t as defined earlier since the product $\Sigma_x P_{ij}^k$ varies with P_{ij} , that is, $E_1(\lambda)$, which becomes inaccurate near $\lambda=0$ as already mentioned. To circumvent this difficulty we adopt the values for the full void by extrapolation from the values for lower void ratios by linear fitting. When approaching close to the full void, it is physically expected that the diffusion coefficients become almost constant. But the exact treatment of the problems will be difficult even theoretically with the multi-group treatment.

The streaming effect changes with the thickness of the sodium plates. In Fig. 4.1.4 the values of $\frac{D_{//} - D_{\perp}}{D_{\perp}}$ are shown against the thickness of sodium plates, where the material composition and thickness of other materials are not changed. The calculations have been performed for full and 80 percent voided sodium, and diffusion constants are collapsed into one group. In this range the streaming effect is proportional to the thickness of the sodium region, that is, the void region, It can be expected that when the thickness of the sodium plate is reduced below about 0.2 cm the streaming effect due to sodium voiding should become very small.

The perturbation theory is used for the calculation of reactivity change $\delta k_s/k$, due to streaming effects, which is defined in R-Z geometry by the formula.

$$\delta k_s/k = \int dE \int dV \left\{ (\delta D_z \frac{\partial^2 \phi}{\partial z^2} + \delta D_r \frac{\partial^2 \phi}{\partial r^2}) \phi^* - \delta D_{\text{homo}} \left(\frac{\partial^2 \phi}{\partial z^2} + \frac{\partial^2 \phi}{\partial r^2} \right) \phi^* \right\} / N.I. \quad (4.1)$$

where δD_z , δD_r and δD_{homo} are the variations in the diffusion coefficients due to sodium voiding in the z and r directions and for homogeneous case, respectively, N.I. is the normalization factor. When the assumption of infinite slab cell is valid D_r is determined by taking the average between $D_{//}$ and D_{\perp} ($D_{\text{av}} = \frac{2D_{//} + D_{\perp}}{3}$), but because the length of the void region is small for the case of a single channel void this assumption causes a large over-estimation of radial leakage.** It is difficult to obtain an appropriate value of D_r for cells with small width, and so we use D_{\perp} when calculating the radial leakage, which will result in some underestimation of leakage near the radial core boundary.

Heterogeneity effects on the effective cross sections of the cell are also obtained by averaging the cross sections of each material with the spatial fine structure flux. Reactivities are calculated by direct k calculation and the first order perturbation theory.

4.1.4 Results and Discussion

Table 4.1.1 presents a comparison between measurements and calculations, the latter values being given both corrected and uncorrected for streaming effect. Reactivities are obtained from the differences derived from direct criticality calculations. If the streaming effect is not considered, the factor C/E (calculated reactivity/measured reactivity) of case S-1, which represents the case of void core center, is 0.58 and the values of C/E are gradually improved as the void channel approaches the core boundary.

** The parallel directional collision probability in the direction of the finite length becomes small because the optical path length with small angle (angle to slab surface) becomes shorter when a neutron passes the sodium region outside the void region. This decreases $D_{//}$ as defined by Eq. (2.42). The overestimation of D_r results in a larger inaccuracy where leakage is large.

However, when the streaming effects are considered, almost all the values of C/E come close to 0.9, which is a fairly good value considering the uncertainty in cross section. In Fig. 4.1.5, the space dependence of the leakage components are shown for the cases of S-1 ~ S-6. The individual leakage components are defined by

$$\text{Homogeneous leakage} = \int dE \int dV \delta D_{\text{homo}} \left(\frac{\partial^2 \phi}{\partial z^2} + \frac{\partial^2 \phi}{\partial r^2} \right) \phi^* / N.I.,$$

$$\text{Axial leakage} = \int dE \int dV \delta D_z \frac{\partial^2 \phi}{\partial z^2} \phi^* / N.I.,$$

$$\text{Radial leakage} = \int dE \int dV \delta D_r \frac{\partial^2 \phi}{\partial r^2} \phi^* / N.I..$$

Anisotropic leakage = axial leakage + radial leakage and axial streaming is defined by Eq.(4.1). The streaming effect in the axial direction (read in $-10^{-4} \Delta k/k$ unit marked on the left-hand side of the figure) is largest in the central channel of the core, that is about 35 percents of reactivity, and negligibly small at the core boundary.

The contribution to reactivity provided by axial leakage is greater than the radial in S-1 ~ S-4, but the trend is opposite for S-5 ~ S-6. At the core boundary (S-6), the radial leakage is about 7 times the axial and thus in this region the axial streaming effect is quite small. The total anisotropic leakage components are almost flat over the core and provide about 80 ~ 90 percents of the total sodium void reactivity except at the boundary channel. On the other hand, the spectrum components are negative in the central region and become positive with approach to the core boundary.

In Table 4.1.2 the spectrum components are presented for fission, absorption, inelastic scattering and elastic removal scattering. The absorption and inelastic scattering components tend toward the negative

side with approach to the core boundary. On the other hand the fission and elastic removal components tend toward the positive side, and more steeply than the negative components. The elastic removal component changes more rapidly than all the rest. This space dependence is due to flattening of the adjoint spectrum, particularly below 1 MeV. The elastic removal component given by $\delta\Sigma_{er}^i \phi_i (\phi_{i+1}^* - \phi_i^*)$, where $\delta\Sigma_{er}^i$ is the difference in elastic removal cross section, and ϕ_i, ϕ_i^* are flux and adjoint flux of i -th group, respectively, is positive above 1 MeV and negative below this value. As the adjoint spectrum flattens, the negative component becomes smaller since the factor $(\phi_{i+1}^* - \phi_i^*)$ is reduced.

For the widely distributed void regions, C1, 2, and M1, 2, 3 the values of C/E are improved consistently by considering the streaming effect, as shown in Table 4.1.1. If $D_{r(av)}$ (average of $D_{//}$ and D_{\perp}) is used instead of D_{\perp} for the case C-2 the value of C/E becomes 1.01, since the assumption of infinite slab becomes better for such greatly voided regions.

For the cases mentioned above our method of treating the streaming effect is adequate, but the assumption of infinite length of the plates will cause overestimation in the void regions which are small compared to a mean free path. For example, in the axial edge region, 20.32 ~ 30.48 cm, in central nine channels, C/E is 0.89 when the homogeneous diffusion coefficient is used but it becomes 1.65 by taking into consideration the correction for axial streaming, as presented in Table 4.1.3. It thus becomes necessary to calculate collision probabilities for finite length cell in order to obtain a sufficiently accurate anisotropic diffusion coefficient.

Table 4.1.3 gives the comparison between measurement and calculation for the central void reactivity. Even if the streaming effect is taken into account, the values of C/E still remain at 0.46 and 0.47 for the region, 0 - 10.16 cm, 0 - 20.32 cm, respectively, since the streaming effect is

small at the center of core. By comparing the results for the nine central channels of which the void regions are 0 - 10.16, 0 - 20.32 cm and 0 - 30.48 cm (case C-1), it can be said that the values of C/E are improved as the void region extends toward the core boundary, and correspondingly the leakage component of the reactivity becomes larger. Therefore the large discrepancy produced at the center of core would appear attributable to inadequate treatment of the spectrum component. Moreover, we note that the results presented in Table 4.1.1 invariably carry a bias to lower values of about 10 percents compared with measurements. This convinces us that the difference is partly due to underestimation of the spectrum component.

For the region, 0 - 10.16 cm, two calculations were performed in addition to the above, as shown in parentheses in Table 4.1.3. In one case, the core was treated as one region when collapsing the group cross sections, and a value of $-1.90 \times 10^{-4} \Delta k/k$ was obtained for the reactivity. In this treatment the space dependence of the core spectrum was neglected, as in the heterogeneous case to be discussed later. Consideration of space dependence by dividing the core into three regions brought a difference about 14 percent. When the collapsed cross sections for all regions which were obtained for the voided case by one dimensional calculation were used for the corresponding regions in two dimensional calculations, the void reactivity was found to decrease significantly, to a value of $-0.70 \times 10^{-4} \Delta k/k$. This means that the influence of the void region on the environment is considerable when the void region is large. On the other hand the influence of the environment on the void region is also important, and detailed investigation will be required.

The cell heterogeneity effect on the spectrum component was calculated for the pattern C-1 and the central void (0 - 10 cm). Void reactivity changes were obtained from six-group calculations by using homogeneous and

heterogeneous cell averaged cross sections. Table 4.1.4 shows the results obtained by calculating each component from the perturbation theory.

The heterogeneity effects are negative on the spectrum terms, which improves the calculational values in reference to the measurements, especially in the case of central void. The group contribution is given in Table 4.1.5. The negative effect on the absorption plus fission term is mainly due to the diminution of fission cross sections at higher energy groups. The scattering component also shows a negative contribution.

The main part of the scattering component is caused by the change in the elastic removal cross sections and in the shape of the adjoint flux. The method of calculation of the elastic removal cross section requires to be studied more precisely. First, perturbation calculations were performed to examine this problem using 25 groups and 70 groups in the region 0 - 10.16 cm. The result is presented in Table 4.1.6. The table shows a larger difference in scattering component, which is also true for the 6-group calculation. Therefore it can be supposed that the ambiguity is due mainly to the treatment of the scattering term. The main contribution to the scattering component is provided by the energy range 2 MeV - 25 keV, and that around 3 keV where predominant resonances of oxygen, iron and sodium are observed. The contribution from the single 2.85 keV sodium resonance is fairly small, in contrast with the case of more dilute (large fast) core. The difference in the scattering component is due to the inadequacy of group structures for 25-group constants, and to treatment of the elastic removal cross sections of these light and medium weight elements at the resonances, the same self-shielding factors for the elastic scattering cross sections having been used for the elastic removal cross sections in the JAERI Fast set.

The method of calculation of the JAERI Fast set was examined by the ultra fine group calculation, and its influence on sodium void reactivity was

studied. The exact effective elastic removal cross sections were obtained for a homogeneous medium composed of oxygen, sodium, iron and ^{238}U with use made of the ERSE code⁽⁴⁶⁾, where the main resonances of oxygen, sodium and iron are presented by the resonance parameters. (The sodium cross sections are compared in Table 4.1.7 for conventional and fine-group calculations). The effect of these differences on reactivity is estimated by perturbation calculations. The result shows that the values for the case of S-1 becomes more negative by about five percent but less negative in the case of conral void. While the influence is not very appreciable for the V-1 assembly, they will not be negligible for a more dilute core.

When few-group calculations are performed, it is important to select appropriately the group boundaries in relation to the position of large scattering resonance peaks and to the shape of the adjoint spectrum. It is desirable to collapse the energy groups where the adjoint spectrum is almost flat. For the region 0 - 10.16 cm (see Table 4.1.3), a reactivity of $-1.84 \times 10^{-4} \Delta k/k$ is obtained when the 6-group cross sections with improved group structure are used.

4.1.5 Concluding Remarks

Sodium void reactivities measured in the FCA V-1 assembly are well predicted by taking into consideration two effects, axial streaming and spatial flux heterogeneity. For cases where channels are voided throughout the core height, the axial streaming effect is very significant because the leakage component dominates in the sodium void reactivity. This effect can be estimated with satisfactory precision by using anisotropic diffusion coefficients and the perturbation theory. In computing the directional collision probability, the assumption of infinite slab cell appears applicable to void regions extending throughout the channels, but it becomes

less valid for void regions having a relatively small width or length. The anisotropic diffusion coefficients for the case of full void should be obtained by extrapolation from values obtained for lower void ratios.

Spatial flux heterogeneity results in a small negative reactivity change attributable to negative spectrum components. These reactivity changes are about 10 percents for voided central channel, and 20 percents for the case of central void. This effect is more important in regions with a large spectrum component. Further study will be required to show whether or not the assumption of infinite slab cell, despite of the actually finite length and numbers of voided cells, is adequate in the central region. The environment effect will also have to be examined in detail.

The elastic removal cross section given by the conventional group constant set, is not accurate; however, the calculation by the 70 group JAERI Fast set has resulted in values not far from the ultra fine group calculations performed previously. Present treatment of resonance cross sections for light and medium weight elements has not included all the resonances, and the nuclear data are different from the JAERI set.

Table 4.1.1 Comparison of measurements and calculations for channel void

Cases	Position of void center from core center (cm)	Number of void channels	Measurements	$(\times 10^{-4} \Delta k/k)$	
				Calculations (C/E)	Calculations (with streaming effects) (C/E)
S-1	0	1	2.39 ± .11	1.39 (.58)	2.24 (.94)
S-2	5.52	1	2.25 ± .03	1.42 (.63)	2.20 (.98)
S-3	11.04	1	2.36 ± .03	1.54 (.65)	2.15 (.91)
S-4	16.56	1	2.41 ± .01	1.77 (.73)	2.17 (.90)
S-5	22.08	1	2.39 ± .04	2.08 (.87)	2.13 (.89)
S-6	27.60	1	2.07 ± .04	1.81 (.88)	1.82 (.88)
C-1	0	9	20.1 ± .1	11.1 (.55)	18.0 (.90)
C-2	0	33	75.0 ± 9.8	47.7 (.64)	66.4 (.88)
M-1	0	9	22.0 ± .7	13.1 (.60)	19.2 (.88)
M-2	0	21	44.4 ± 3.1	34.5 (.78)	45.6 (1.03)
M-3	0	33	75.3 ± 9.3	56.4 (.75)	67.9 (.90)

Table 4.1.2 Space dependence of spectrum component

($\times 10^{-5} \Delta k/k$)

	Fission	Absorption	Inelastic Scattering	Elastic removal
S-1	-.363	2.64	1.33	-6.41
S-2	-.344	2.51	1.29	-6.00
S-3	-.297	2.17	1.18	-4.96
S-4	-.227	1.66	1.02	-3.30
S-5	-.148	1.07	0.873	-1.10
S-6	-.074	0.524	0.665	1.18

Table 4.1.3 Central void reactivities

($10^{-4} \Delta k/k$)

Region	0 - 10.16 cm	0 - 20.32 cm	20.32 - 30.48 cm
Experiment	-4.0 ± 0.1	-10.9 ± 0.1	-5.5 ± 0.1
2-dimensional, 6-group calculation	$-1.66(-1.90)^*$ $(-0.70)^{**}$	-5.14	-4.87
With streaming	-1.87	-7.42	-9.15

* The standard core was treated as one region.

** Collapsed cross sections obtained from the voided case were used for all regions.

Table 4.1.4 Heterogeneity effects on C-1 and central void

$(10^{-4} \Delta k/k)$		
	C-1	Central (0 - 10.16 cm)
Experiment	-20.1 ± 0.1	-4.0 ± 0.1
Homogeneous	-11.1	-1.90
Hetero. isotropic D*	-13.5	-2.75
Capture + fission**		
Homogeneous	+ 1.45	+0.746
Heterogeneous	+ 0.163	+0.111
Scattering**		
Homogeneous	- 2.52	-1.54
Heterogeneous	- 2.93	-1.65
Hetero. with streaming	-20.7	-2.97
Homo. with streaming	-18.0	-2.12

* Direct calculation

** Perturbation calculation

Table 4.1.5 Group contributions from heterogeneity effect
(hetero - homo) $\times 10^{-4} \Delta k/k$

Groups	Capture + fission		Scattering	
	C-1	Central(0 - 10.16 cm)	C-1	Central(0 - 10.16 cm)
1	-0.551	-0.262	0.083	0.029
2	-0.618	-0.290	0.135	0.017
3	0.261	0.115	-0.015	0.020
4	-0.395	-0.200	-0.252	-0.027
5	0.015	0.004	-0.364	-0.151
6	0.001	-0.001	—	—
Total	-1.287	-0.634	-0.413	-0.112

Table 4.1.6 Dependence of components on spectrum for
(0 - 10.16 cm) region

Groups	$(\times 10^{-4} \Delta k/k)$			
	Capture + Fission	Scattering	Leakage	Total
25G	1.019	-1.460	-1.059	-1.500
70G	0.907	-2.040	-1.104	-2.237

Table 4.1.7 Ratio of effective elastic removal cross sections
of sodium (R = fine group calculation^{*}/JAERI set)

G	R	G	R	G	R	G	R
10	1.15	16	0.98	23	0.94	33	0.62
11	1.00	17	1.01	24	0.56	34	2.19
12	0.97	20	1.21	25	1.03	35	1.14
13	0.88	21	0.97	26	0.97	36	1.04
14	1.09	22	0.96	32	0.85	37	1.01

G : group number in JAERI Fast set with 70 group
structure.

* Infinite dilution cross sections are normalized
to JAERI FAST set.

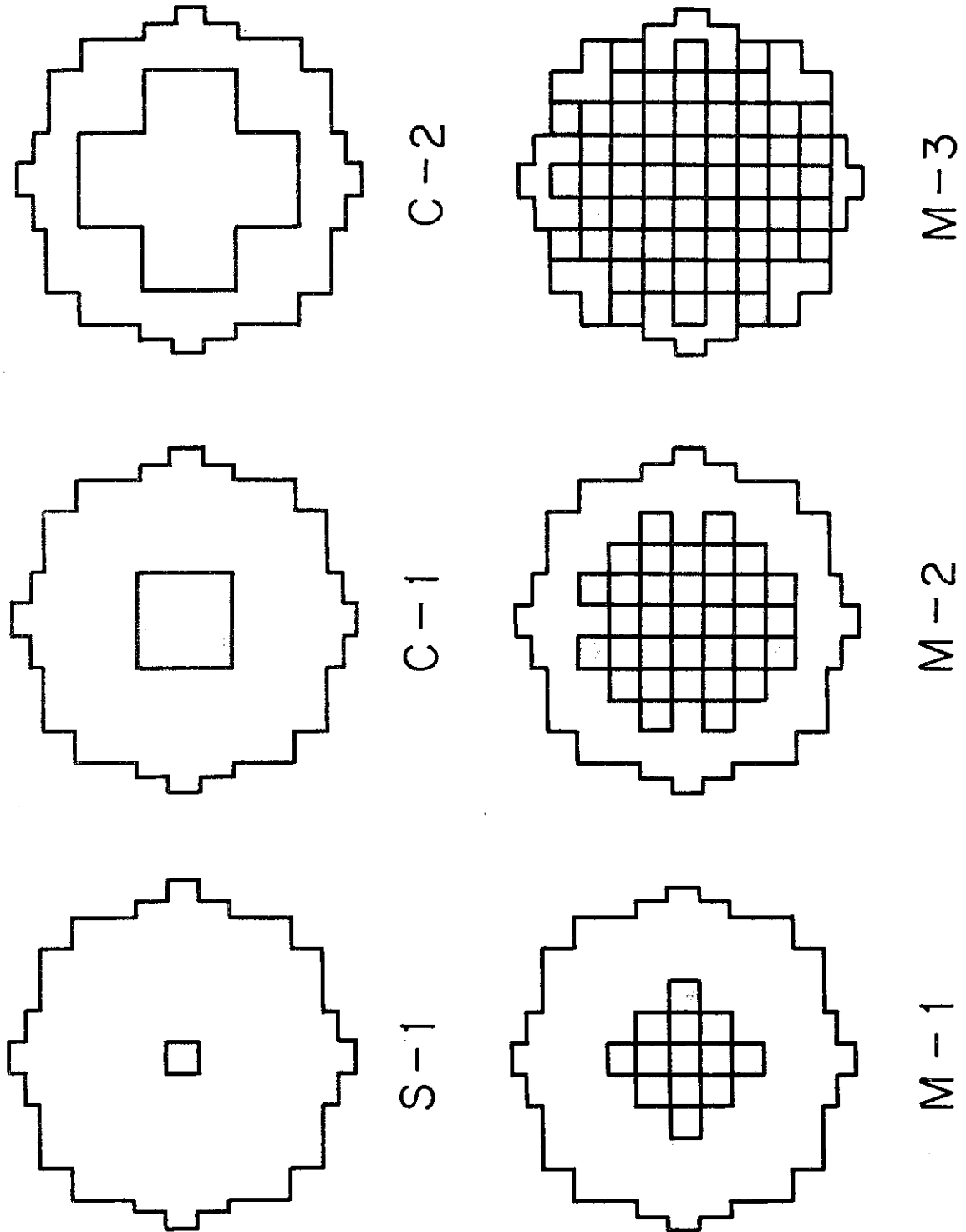


Fig.4.1.1 Sodium voided zones in FCA V-1

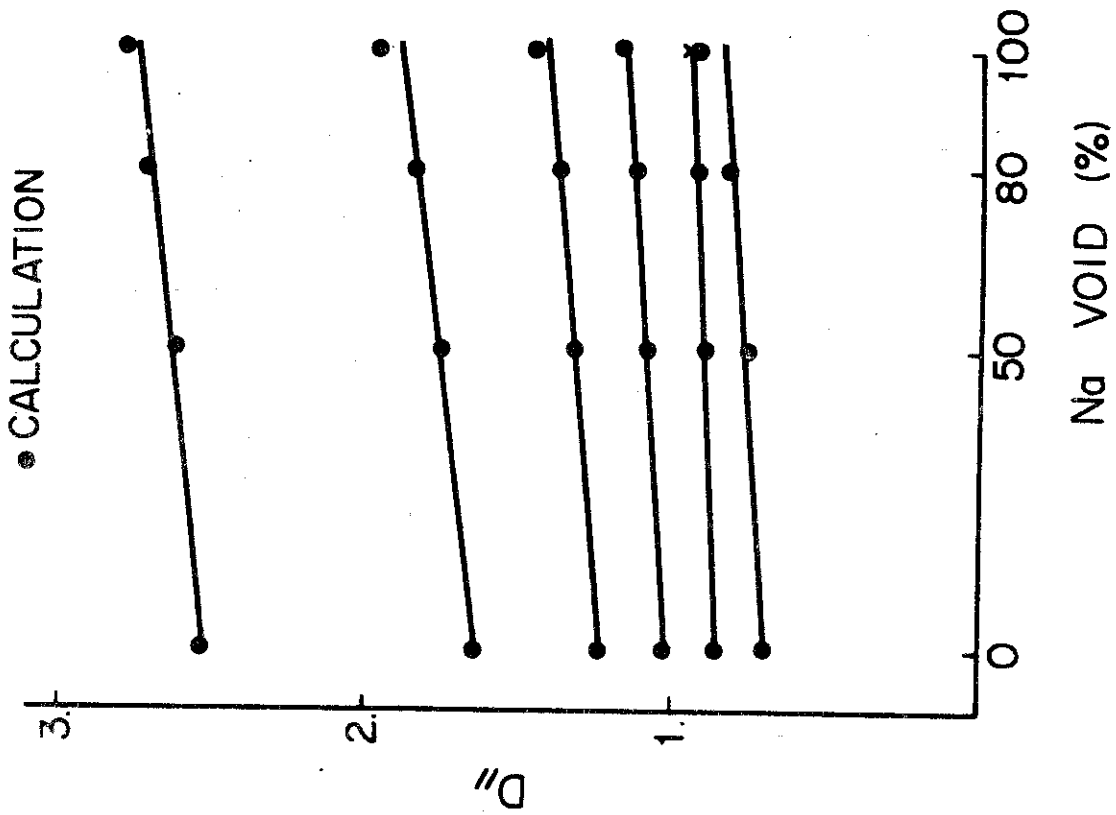


Fig.4.1.1.3 Parallel directional diffusion coefficient

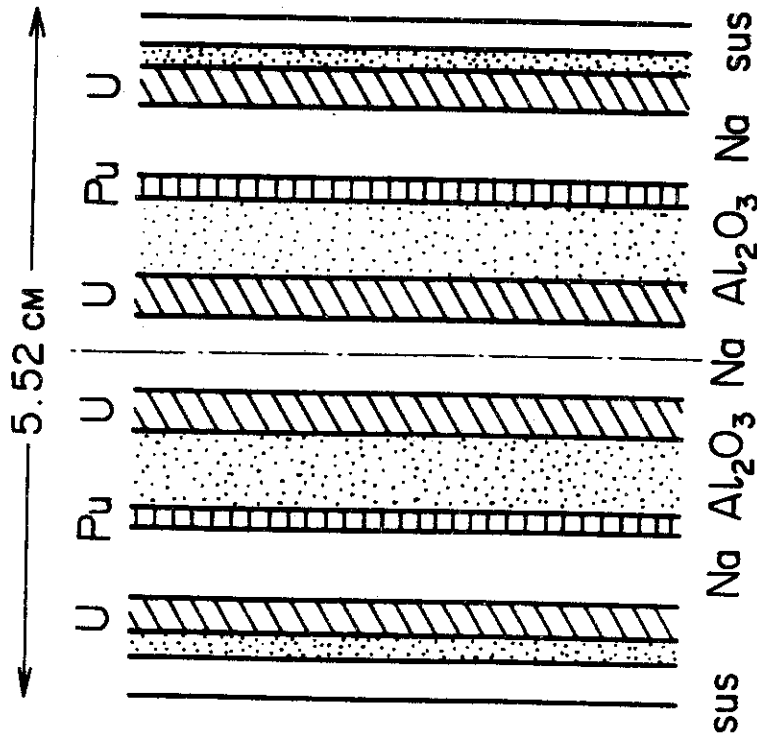


Fig.4.1.1.2 Unit cell structure

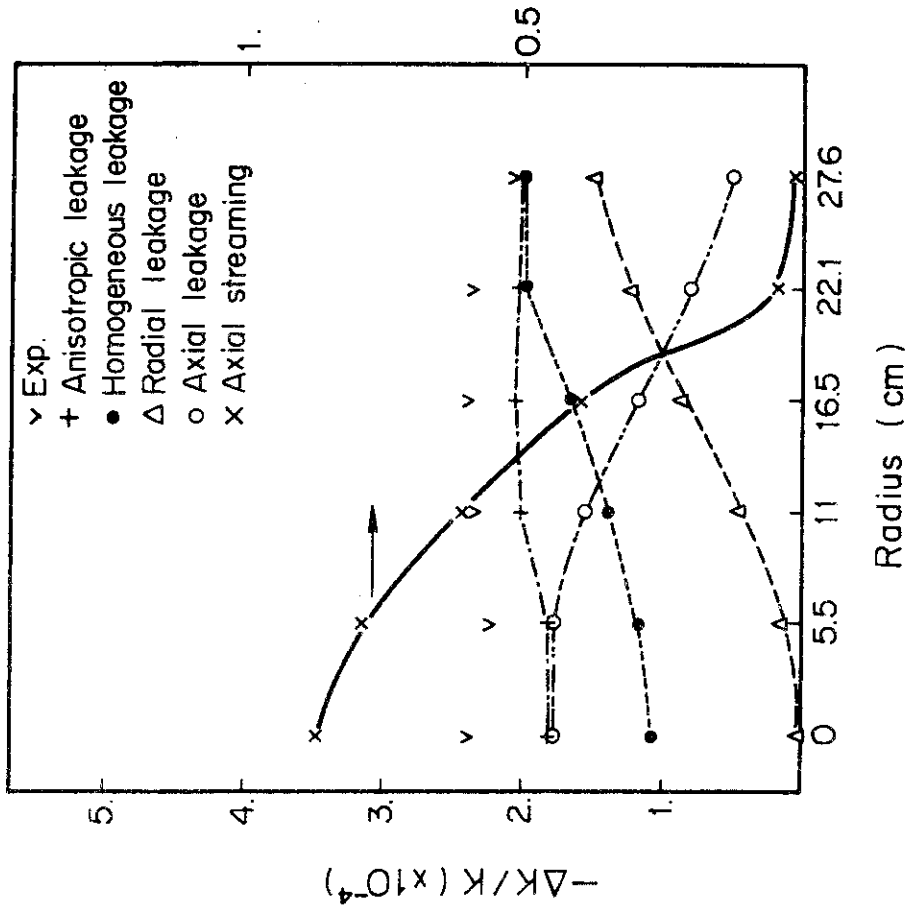


Fig.4.1.5 Space dependence of leakage component

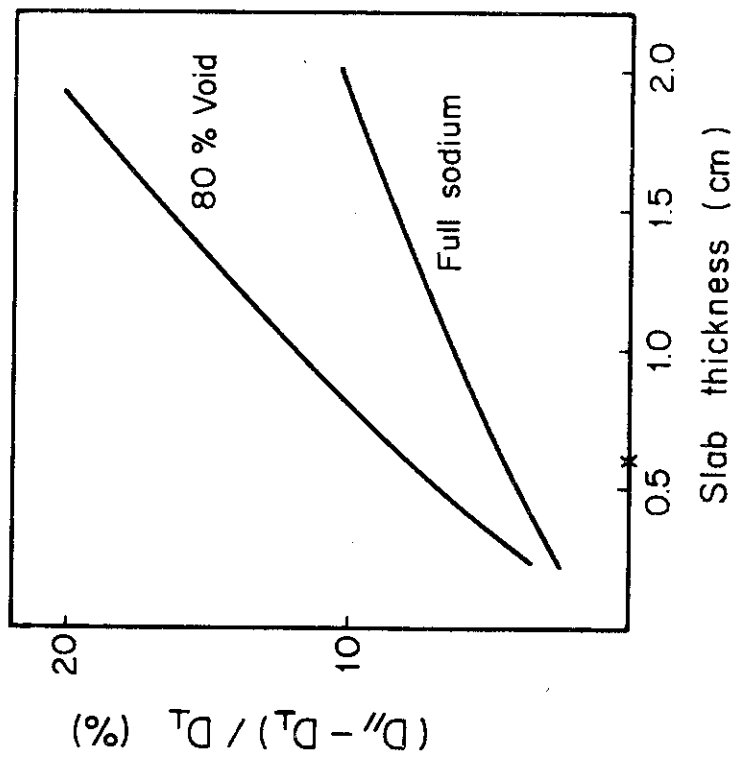


Fig.4.1.4 Dependence of anisotropy on sodium plate thickness

4.2 Analysis of MZA and MZB Assemblies

4.2.1 Description of Assemblies

MZA and MZB were constructed at fast critical assembly ZEBRA⁽¹³⁾ in Winfrith, United Kingdom in order to simulate physics performances of Japan proto-type fast breeder reactor "MONJU". MZA had a single zone core of which the enrichment of plutonium is identical to that of the outer core in MONJU. The core with 90 cm height and 90.8 cm diameter, was surrounded by a blanket of uranium metal with 30 cm thick. MZB was a clean plutonium fueled assembly with two zone core which was designed to provide reasonably close representation of MONJU. In the outer core, the high enriched plutonium used in MZA was contained. In the radial blanket, a sector arrangement was chosen because of inventory limitations. The detailed description of these assemblies was given in Ref.(13).

Sodium void worths were measured by replacing each steel-canned sodium plate by a dummy steel can at the central nine elements in MZA. They were voided in turn from the four axial zones, central cells, intermediate cells, cells at the core edge and then all axial blanket cells. Also the whole elements were voided together. Figure 4.2.1 shows the rz model of MZA and its voided configuration at the core center.

In MZB, nine elements in six different radial positions were voided. At the core center, central three cells, upper and lower three cells and axial blanket cells were voided in turn and all together. The sodium void worths for pin elements were also measured at the center and at the off-center of the inner core. Twenty five pin elements containing fuel and blanket pins in the sodium filled calandria replaced for the plate elements at the center in a 5×5 array. The partial voided regions of central nine elements were almost the same as the plate elements. Sodium was

removed also from one or four pin elements at the core center. A pin calandria with 12 inch height and 2×2 inch cross section contained 16 fuel pins of PuO_2/UO_2 . The composition of the calandria corresponded closely to that of the inner core plate cell. The rz model of MZB is presented in Fig.4.2.2. The detail of measurements was explained in Ref.(21).

4.2.2 Method of Analysis

The analysis was carried out with use of the JAERI Fast set version 1 (JFS-V1) and version 2 (JFS-V2) with 70 group structure.⁽⁵¹⁾ In modeling plate cells, canning stainless steel was homogenized into the inner materials, and the matrix tube and drawer bottom were diluted into the cell materials. The pin calandria was modeled by two concentric cylindrical regions of fuel with an actual radius of 0.42418 cm and a diluent region of 0.76524 cm thick. The outer radius of pin cell was determined to conserve the volume of one sixteenth of a unit matrix tube. The outer region contains the cladding, sodium, pin calandria and matrix tube. The adequacy of two-region model adopted here was confirmed by comparing it with three- or four-region model. The cell calculations were performed by using the SLAROM code. The heterogeneity effect on the resonance shielding factor was taken into account by the Dancoff factor given by Bell⁽³⁷⁾ for a pin cell and by Meneghetti⁽³⁶⁾ for a plate cell. The anisotropic diffusion coefficient was obtained to estimate the neutron streaming effect. Since the plate surfaces are arranged in perpendicular to the core axis (z-axis) in ZEBRA, the streaming effect around the central elements of the core will contribute negatively to the sodium void reactivity, since the neutron leakage to z direction is proportional to the perpendicular

directional diffusion coefficient which is smaller than the isotropic value. Therefore, it is contrast with FCA or ZPPR assemblies. The reactivity change due to the streaming effect was calculated by the CIPER code using exact perturbation theory. The collapsed cross sections were obtained by one-dimensional diffusion calculations in slab geometry for the central regions and in cylindrical geometry for the other regions. The number of groups were 18 for the version 2 and 12 for the others. The rz model was used for the central voiding cases.

In the calculation of MZB, also JFS-1R,⁽⁵²⁾ the revised set of JFS-V1 was used to examine an influence of the cross sections. The revision was made for σ_f of ^{235}U , σ_f of ^{239}Pu and σ_c of ^{238}U . The new fission cross section of ^{235}U is 10 percents less in 100 keV ~ 1 MeV and about 5 percents less in 10 ~ 100 keV than that of the version 1. The fission cross section of ^{239}Pu becomes lower by about 1 ~ 2 barns in the energy range, 10 keV ~ 1 MeV. The capture cross section of ^{238}U is reduced slightly in the energy range 10 keV ~ 1 MeV, so it is generally in a good agreement with the data of Moxon.⁽⁵³⁾ The cross section in the resonance region was not revised in this version. Moreover, we evaluated current experimental data and data files to examine the nuclear data of sodium adopted in JFS-V1. The modified set (JFS-N) was produced from JFS-1R and used for the calculation of MZB.

The effective multiplication factors are presented in Table 4.2.1 for the reference cores. It shows k_{eff} and heterogeneity effect for different versions of JFS. The heterogeneity effect of MZB is about 1.2 % $\Delta k/k$ for all the versions. The version 2 gives smaller k_{eff} by about one percent than the JFS-V1 for both the assemblies. When the transport effect and impurities are taken into account, k_{eff} of MZA becomes slightly larger than the measured value and k_{eff} of MZB comes to be predicted

accurately.

4.2.3 Results and Discussions on MZA

The calculational results are compared with measurements in Table 4.2.2. The worths and streaming effects were calculated by the exact perturbation method. The JFS-V1 gives more negative values than the measurements. However, JFS-V2 shows an excellent agreement except for the whole elements case (A ~ D). The C/E values corrected with the streaming effects are almost within the uncertainties of experiments. The specific worth ($\Delta k/k/\text{Na-kg}$) of the case B is not so deviated from the measurement compared with the other cases though the C/E value is 0.66. It can be seen that the sodium void worth is quite sensitive to the group cross sections used. The neutron streaming effect is negligibly small at the center and gradually increases as approaching to the core boundary since the gradient of neutron flux becomes larger. The corrections for the cases C, D and A ~ D amount to several times of the uncertainties of experiments, so they are important to obtain consistent prediction. The anisotropic diffusion coefficients have been defined under the assumption that the length of the cell is infinite and it is arranged infinitely. However, in these voided cases, the actual length is 16.28 cm, so the anisotropic diffusion coefficients obtained here may result in a uncertainty in the final leakage correction.

In Table 4.2.3, the calculated values are resolved into the components for each region. It can be seen that the fission, absorption and scattering (spectrum) components decrease as the region approaches to the axial boundary and on the contrary, the leakage component increases. The net worths of the regions B and A ~ D, where the C/E values deviate fairly from 1.0, are determined through the cancellation of large positive and negative

components, and accordingly even if an error of each component would be small, it may cause a discrepancy in the net worth.

4.2.4 Neutron Cross Section Evaluation of Sodium

The neutron cross section of sodium influences sensitively to the sodium void reactivity. The original version of the JAERI Fast set adopted the data in the UKNDL-1967.⁽⁵⁴⁾ Since numerous measurements have been made on sodium cross section, especially for the resonance at 2.85 keV, we re-evaluated the current data. Elastic scattering cross section is compared among the ENDF/B-4,⁽⁵⁵⁾ UKNDL-1972⁽⁵⁶⁾ and KEDAK⁽⁵⁷⁾ in Fig.4.2.3. They almost agree with each other except for the resonances at 2.85 keV and 54 keV, while the UKNDL has given the low resolution data. The peak value at 2.85 keV is 350 barns in the ENDF/B-4 and 600 barns in the UKNDL and KEDAK files. The UKNDL shows a narrow neutron width Γ_n which would be based on the data by Hibdon.⁽⁵⁸⁾ Table 4.2.4 shows the resonance parameters currently measured or evaluated. The peak value of 600 barns was obtained by assigning the total angular momentum $J=2$. The measurements listed in the table may support $J=1$. Therefore, we adopt here the value $J=1$. Though it is difficult to choose the neutron width Γ_n , we have concluded that $\Gamma_n=410$ eV is better than 380 eV. As the radiation width Γ_γ , 0.35 eV or 0.47 eV is supported from the table. The former value seems to be better considering the theoretical extrapolation from the thermal region. The point wise cross section is calculated by using these resonance parameters and plotted in Fig.4.2.4, where the value of JFS-V1 is also shown. It reveals that the revised value becomes smaller compared with the original one. The infinite dilute group cross sections are presented in Table 4.2.5 in the energy range, 59.8 ~ 1.0 keV. The elastic scattering

cross section is compared for $\Gamma_n = 410$ eV and $\Gamma_n = 380$ eV, and its difference at the 2.85 keV resonance is found to be less than ten percents. The capture cross section is compared for $\Gamma_\gamma = 0.47$ eV and 0.35 eV, and found that it differs by about 30 percents between them. The capture cross section was insensitive to the neutron width. In the higher energy region, 5 ~ 150 keV, the capture cross section shows a large discrepancy among three files though its absolute value is small. Especially, the ENDF/B-4 gives a lower value.

As a conclusion, the present data are the same as in the ENDF/B-4 except for Γ_γ of 2.85 keV resonance. These data were processed to produce the group constants for the revision of JFS-1R. We call this version as JFS-N.

4.2.5 Results and Discussions on MZB

The results for the central plate cells are shown in Table 4.2.6. The group constant sets used were JFS-V1, -1R, -N and -V2. The heterogeneous model considers the correction due to the neutron streaming effect. The JFS-V2 shows a good agreement with the measurements. The JFS-V1 gives the results shifted to the negative side compared with the measurements for all the regions. The JFS-1R of which the nuclear data were revised for heavy elements, shifts further the calculated void worths in the core to the negative side. Thus, the revision of heavy elements did not improve the accuracy of prediction of the sodium void reactivity. As for JFS-N the calculations are improved for all the regions. For example, the value of C/E is varied from 0.61 to 0.75 at the center cells. Since the difference between JFS-1R and -N exists only in the cross sections of sodium, it can be said that the void worth of sodium is very

sensitive to the cross sections. The version 2 set predicts the best value among these sets, while it gives still more negative values than the measurements. The experimental uncertainties shown in the table do not include a systematic error (4 %) from the reactivity scale. It is seen, in addition, that the calculation can predict well the change in reactivity, due to the change of voided regions in the core region. In this case, the additivity is well established. On the other hand, for the whole element voiding, the sum of reactivity changes of separate voided regions is larger by ten percents than that of total voided regions in the measurements and by four percents in the calculations.

Table 4.2.7 shows the sodium void reactivity worths obtained from the direct k calculation, the exact perturbation (EP), the neutron streaming effect and the specific void worths. The reactivity worths obtained by differences in k -values agree with those by EP within an expected accuracy of the k -values, a few parts in 10^{-6} . The neutron streaming effect reduces the axial leakage and hence shifts the reactivities to the positive side as mentioned in 4.2.2. The correction is about 15 percents for the whole core voiding. The specific worth is a good criterion to evaluate the consistency of calculated results, especially if the absolute value of reactivity worth is small. The table shows that $(C-E)/kg$ are consistently $-0.02 \sim -0.03 \times 10^{-4} \Delta k/k$ except for the center cells. That is, the calculated values for upper and lower cells, and for elements are not inconsistent with other cases, though their C/E values deviate fairly from 1.0.

The reactivity components obtained by the first order perturbation theory are presented in Table 4.2.8 in order to examine the sources of the differences in the calculated values among the cross section sets and models. These worths were obtained on the basis of the 70 group

one-dimensional spherical diffusion calculations except for the results given in the last two columns. The table includes also the heterogeneous calculation and the two-dimensional 12- or 18-group calculations. It can be seen from Table 4.2.8 that the leakage term is nearly constant overall the sets in the one-dimensional cases, but the values differ fairly from the two-dimensional results. It is seen thus that this term is insensitive to the cross section sets but sensitive to the geometrical model. Both the fission and absorption terms are on the most positive side for JFS-V2. The heterogeneity effect influences significantly these terms. The scattering term (spectrum term) is a dominant contribution to the central void worth and it is the main source of the difference among these sets. This term depends sensitively also on the number of energy groups. The order of the magnitude given by each set is JFS-1R < JFS-V1 < JFS-N < JFS-V2, and this is the same order as that of the total worths. It can thus be concluded that the larger positive contribution from the scattering term has decreased the discrepancy between the calculation and the measurement in the case of JFS-V2.

In order to examine the dependence of the neutron streaming effect on the group constant set, Table 4.2.9 shows the ratio of the parallel directional ($D_{//}$) to perpendicular directional diffusion coefficient (D_{\perp}) and the difference between the ratios at the normal and voided inner cores for the energy groups 1 ~ 40 in the 70 group structure. We can see that the value $D_{//}/D_{\perp}$ are rather close to unity with the deviation of about several percents for all the groups. The difference between the values in the normal and void states, $(D_{//}/D_{\perp})_{\text{void}} - (D_{//}/D_{\perp})_{\text{normal}}$, which is roughly proportional to the streaming correction, hardly depends on the group constant sets for all the groups except for the groups 33 and 34, which include the 2.85 keV sodium resonance with the largely different

peak value between JFS-V1, -1R and JFS-N, -V2 as mentioned in 4.2.4. As a result, it can be said that the correction by neutron streaming effect is insensitive to the group constant sets. These values are only about a few percent, though they contribute significantly to the reactivity corrections. Thus, the calculation method should be carefully selected to obtain a sufficiently accurate correction for the neutron streaming.

Table 4.2.10 presents the results of the calculations (with JFS-V1, -N and -V2) and measurements for the sodium void reactivity worth of the central nine pin elements. The results have been corrected for the neutron streaming effect. The JFS-V1 and -N predict more negative reactivities than the measurements similarly to the cases of plate cells. The JFS-V2 shows a better agreement for all the cases except for the whole elements. Moreover, the deviation of specific worth from the measurements (C-E)/kg are consistent throughout the cases except for the axial blanket. In the core region, the reactivity worths obtained by JFS-V2 are slightly more positive compared with the measurements. As shown in the table, the corrections by the neutron streaming effect is not so significant for the pin cell as for the plate cell, though it may not be negligible for the case of whole element voiding. This fact suggests that the neutron streaming effect will not significantly influence the sodium void reactivity in power reactors, while it will be necessary for an accurate prediction of the relatively small reactivity worth.

In Table 4.2.11, the reactivity worths are shown for one, four and nine elements at the center of MZB, where the results by JFS-N and JFS-V2 are given. Though JFS-N underestimates the positive reactivities for all the cases, JFS-V2 predicts them with a high confidence. The table also shows the relative value to the worth of one element voiding in parentheses. The measurements deviate only slightly from the proportionality and the

worth per one element becomes smaller than that of one element voiding. The JFS-N shows a similar proportionality while the worth per one element is smaller than the measurements. On the other hand, JFS-V2 shows a contrary proportionality to the measurements. It may arise from the fact that the space dependence of the cross sections in voided regions is not considered in the calculations using JFS-V2.

The present results are compared with an independent work performed by Stevenson et al.⁽²¹⁾ for the pin and plate cells of nine elements. Table 4.2.12 shows the non-leakage and leakage components and the total reactivities obtained by the exact perturbation method. Stevenson et al. calculated by the two-dimensional diffusion model with 37 groups. Since they did not correct for the neutron streaming effect, the present results do not include it. The table shows an excellent agreement between our results and UK calculations for the core region. Especially, the leakage components for plate cells agree quite well. For pin cells, UK calculations give slightly more negative leakage components, which may be caused by the difference in the model of calandoria and fuel pin. Though the non-leakage component is very sensitive to the calculation model and the cross sections, these results show the similar values.

Table 4.2.1 Comparison of effective multiplication factor of MZA and MZB

	MZA	MZB
Experiment	1.0108±.0009	1.0040±.0009
JFS-V1	1.0231 (0.0103)*	1.0139 (0.0119)*
JFS-1R	—	1.0058 (0.0118)*
JFS-N	—	1.0023 (0.0115)*
JFS-V2	1.0148	1.0036 (0.0125)*
Correction**	+0.0034	+0.0023
Corrected V2	1.0182	1.0059

JFS-V1 : original version presented in Ref.(9), (10)

JFS-1R : revised for heavy elements by adjustment method

JFS-N : sodium cross sections are modified.

JFS-V2 : second version presented in Ref.(51)

* Heterogeneity effect on k_{eff}

** Correction for transport effect and impurities

Table 4.2.2 Sodium void reactivity worth in MZA
 ($\times 10^{-4} \Delta k/k$)

Voided region (cm)	A 0~15	B 15~30	C 30~45	D 45~80	A ~ D 0~80
Mass of sodium (kg)	2.55	2.55	2.55	6.79	14.13
Experiment	3.41±.22	0.55 ±.20	-3.05±.17	-3.22 ±.16	-1.80 ±.43
Specific worth (/kg)	1.34±.086	0.216±.078	-1.20±.067	-0.474±.024	-0.127±.03
JFS-V1	1.61	-0.77	-3.99	-3.69	-6.84
(C/E)	0.47	—	1.31	1.15	3.80
JFS-V2	3.06	0.097	-4.01	-3.54	-4.82
Streaming effect	0.029	0.268	0.818	0.544	1.72
Corrected with streaming effect	3.09	0.365	-3.19	-3.00	-3.10
(C/E)	0.91±.06	0.66 ±.36	1.05±.06	0.93 ±.05	1.72 ±0.24
(C-E) (/kg)	-0.125	-0.073	-0.055	0.032	-0.092

Table 4.2.3 Components of sodium void reactivity worth by
 exact perturbation in MZA ($\times 10^{-4} \Delta k/k$)

Component	Voided region (cm)	A	B	C	D	A~D
		0~15	15~30	30~45	45~80	0~80
Fission		-1.30	-0.884	-0.363	-0.023	- 2.60
Absorption		1.61	1.13	0.549	0.244	3.53
Scattering		3.44	2.57	1.44	1.10	8.65
Leakage		-0.688	-2.72	-5.63	-4.87	-14.40
Total		3.06	0.097	-4.01	-3.54	- 4.82

Table 4.2.4 Resonance parameters of ^{23}Na at 2.85 keV

E_r (eV)	Γ_n (eV)	Γ_γ (eV)	J	Reference
2810	380 ± 15	(0.34)	1	Seltzer, Firk, N.S.E. ('74)
2860	424	0.6	1	Moxon, CN-23/27
2850	400		1	Rahn et al, Phy. Rev. C. ('73)
	(410)	0.35		Friesenhahn, Wash. Conf. ('68)
	(424)	0.35	1	Kopecky et al, RCN-175 ('72)
		0.47		Hockenbury ('70)
		0.47		Yamamuro, N.S.E. ('70)
	220			Hibdon, UK 72
*2850	410	0.47	1	ENDF B/III, IV
*2850	410	0.38	1	BNL-325, 3rd. ed. ('73)
*	380	0.22		Schmidt, KFK 120

* Evaluated values

() Assumed values for determining Γ_γ or Γ_n

Table 4.2.5 Comparison of infinite group cross sections of ^{23}Na

Energy (keV)	Elastic scattering (barn)		Capture (m barn)	
	$\Gamma_n=410$ eV	$\Gamma_n=380$ eV	$\Gamma_\gamma=0.47$ eV	$\Gamma_\gamma=0.35$ eV
59.8 - 46.5	7.80	7.79	5.11	5.11
46.5 - 36.	3.04	3.02	.138	.137
36. - 27.8	3.48	3.45	.0467	.0451
27.8 - 21.5	3.70	3.67	.0375	.0343
21.5 - 16.6	3.93	3.88	.0454	.0389
16.6 - 12.9	4.20	4.13	.0716	.0579
12.9 - 10.	4.61	4.51	.135	.105
10. - 7.73	5.30	5.13	.295	.224
7.73 - 5.98	6.61	6.31	.739	.555
5.98 - 4.65	9.69	9.06	2.24	1.67
4.65 - 3.6	21.32	19.37	10.4	7.77
3.6 - 2.78	165.1	157.9	166.	123.
2.78 - 2.15	89.49	81.86	124.	92.5
2.15 - 1.66	10.6	9.01	22.6	16.8
1.66 - 1.29	4.66	4.06	12.1	8.98
1.29 - 1.0	3.22	2.90	8.93	6.66

Table 4.2.6 Sodium void reactivity worth for plate cells in MZB
 ($\times 10^{-4} \Delta k/k$)

Void region (cm)	Experiment	Calculation model	JFS-VI	JFS-IR	JFS-N	JFS-V2 (C/E)
Center cells 0 ~ 12 cm	1.75±.02	Homo	1.40	1.32	1.54	1.88
		Hetero	1.22	1.07	1.32	1.72 (0.98±.01)
Upper and lower cells 12 ~ 45 cm	0.56±.04	Homo	-0.36	-0.60	-0.20	0.606
		Hetero	-0.55	-0.70	-0.30	0.366 (0.65±.07)
Axial blanket 45 ~ 80 cm	-0.76±.03	Homo	—	-1.14	-1.09	-0.293
		Hetero	-1.10	-1.04	-1.02	-0.891 (1.17±.04)
Whole core 0 ~ 45 cm	2.31±.05	Homo	—	—	—	2.47
		Hetero	0.68	—	1.01	2.08 (0.90±.02)
Element 0 ~ 80 cm	1.49±.06	Homo	—	—	—	1.98
		Hetero	-0.42	—	-0.15	1.08 (0.73±.04)

Table 4.2.7 Comparison of specific sodium void worth and neutron streaming effect for plate cells in MZB
 ($\times 10^{-4} \Delta k/k$)

Void region (cm)	Center cells	Upper and lower cells	Axial blanket	Whole core	Elements
Mass of sodium (kg)	2.23	5.95	6.81	8.19	14.99
Experiment	1.75±.02	0.56±.04	-0.76±.03	2.31±.05	1.49±.06
Specific worth (/kg)	0.785	0.094	-0.112	0.282	0.099
Hetero. direct	1.72	0.050	-1.059	1.756	0.548
Exact pert.	1.71	0.030	-1.083	1.732	0.546
Streaming effect	0.01	0.336	0.192	0.345	0.538
(C - E)/kg	-0.0135	-0.0326	-0.0192	-0.0284	-0.0271

Table 4.2.8 Comparison of one-dimensional perturbation calculation with 70 groups for central sodium void reactivity
($\times 10^{-4} \Delta k/k$)

Set	JFS-V1	JFS-1R	JFS-N	JFS-V2	JFS-N	JFS-N	JFS-V2
Model Component	Homo	Homo	Homo	Homo	Hetero	Hetero *	Hetero *
						2D - 12G	2D - 18G
Fission	-0.111	-0.123	-0.140	-0.098	-0.390	-0.363	-0.398
Absorption	0.748	0.809	0.744	0.845	0.590	0.597	0.628
Scattering	1.115	0.976	1.288	1.656	1.39	1.140	1.551
Leakage	-0.032	-0.032	-0.032	-0.033	-0.034	-0.089	-0.089
Total	1.720	1.630	1.89	2.37	1.555	1.285	1.692

Calculations were made for spherical geometry by the first order perturbation method.

* Equivolume rz geometry

Table 4.2.9 Anisotropy of diffusion coefficient in normal and void state
 $[(D_{//}/D_{\perp})_{\text{void}} - (D_{//}/D_{\perp})_{\text{normal}}] \times 100$

Group	JFS-V1	JFS-1R	JFS-N	JFS-V2	$D_{//}/D_{\perp}$ (JFS-V2)
1	0.50	0.57	0.55	0.6	1.011
2	0.53	0.59	0.58	0.6	1.013
3	0.56	0.62	0.64	0.6	1.014
4	0.60	0.68	0.71	0.6	1.016
5	0.81	0.89	0.92	0.9	1.024
6	0.68	0.73	0.72	0.7	1.016
7	0.81	0.86	0.87	0.8	1.017
8	1.09	1.14	1.08	1.0	1.025
9	1.47	1.56	1.51	1.4	1.034
10	2.11	2.11	2.04	2.0	1.044
11	1.79	1.84	1.82	1.8	1.024
12	1.73	1.80	1.82	1.6	1.029
13	2.67	2.59	2.54	2.3	1.072
14	2.30	2.38	2.41	2.2	1.052
15	2.25	2.34	2.37	2.2	1.051
16	2.75	2.55	2.55	2.4	1.043
17	2.05	2.08	1.99	1.8	1.045
18	1.93	1.94	2.40	2.0	1.043
19	2.04	2.07	2.15	1.4	1.049
20	1.78	1.82	1.86	1.9	1.045
21	2.20	2.26	2.17	2.1	1.049
22	2.61	2.65	2.52	2.5	1.042
23	1.92	2.06	2.03	1.9	1.048
24	1.09	1.09	1.05	1.0	1.038
25	2.58	2.52	2.46	2.3	1.055
26	2.40	2.45	2.40	2.4	1.054
27	1.94	1.93	1.87	1.9	1.048
28	2.18	2.15	2.03	2.0	1.046
29	1.87	1.87	1.73	5.6	1.041
30	1.67	1.66	1.53	1.8	1.037
31	2.67	2.67	2.54	2.4	1.040
32	2.03	2.04	2.65	2.6	1.028
33	-22.77	-22.75	-14.6	-14.2	1.002

Table 4.2.9 (Continued)

Group	JFS-V1	JFS-1R	JFS-N	JFS-V2	$D_{//}/D_{\perp}$ (JFS-V2)
34	- 8.72	- 8.71	- 3.01	- 2.9	1.005
35	3.01	3.02	3.04	2.7	1.042
36	2.53	2.57	2.02	1.7	1.044
37	2.02	2.00	1.65	1.6	1.046
38	1.62	1.65	1.48	1.5	1.047
39	1.43	2.42	1.34	1.3	1.045
40	1.19	1.28	1.30	1.3	1.047

$D_{//}$: parallel directional diffusion coefficient

D_{\perp} : perpendicular directional diffusion coefficient

Table 4.2.10 Sodium void reactivity worth for pin cell in MZB
 $(\times 10^{-4} \Delta k/k)$

Voided region (cm)	Experiment	JFS-V1	JFS-N	JFS-V2		
					(C/E)	(C-E) (/kg)
Core center 0 ~ 15 cm	1.91±.02	1.23	1.36 (-0.002) *	1.976	(1.03)	0.025
Core edge 15 ~ 45 cm	-0.15±.02	-0.96	-0.83 (-0.10) *	-0.049	(0.33)	0.020
Axial blanket 45 ~ 74 cm	-0.85±.02	-1.00	-1.01 (-0.10) *	-0.865	(1.02)	-0.003
Whole core 0 ~ 45 cm	1.72±.02	0.23	0.55 (-0.05) *	1.92	(1.10)	0.022
Element 0 ~ 74 cm	.74±.02	-0.86	-0.56 (-0.15) *	0.989	(1.34)	0.019

* Reactivity due to neutron streaming effect

Table 4.2.11 Comparison of sodium void reactivity worth for central pin cell in MZB
($\times 10^{-4} \Delta k/k$)

No. of elements	Experiment	JFS-N	JFS-V2
1	0.20±.02 (1.0)*	0.06 (1.0)*	0.204** (1.0)* (1.02)
4	0.77±.02 (3.85)	0.215 (3.59)	0.835** (4.09) (1.08)
9	1.75±.02 (8.75)	0.550 (7.50)	1.92** (9.41) (1.10)

* () shows a ratio of reactivity to one voided element.

** C/E value.

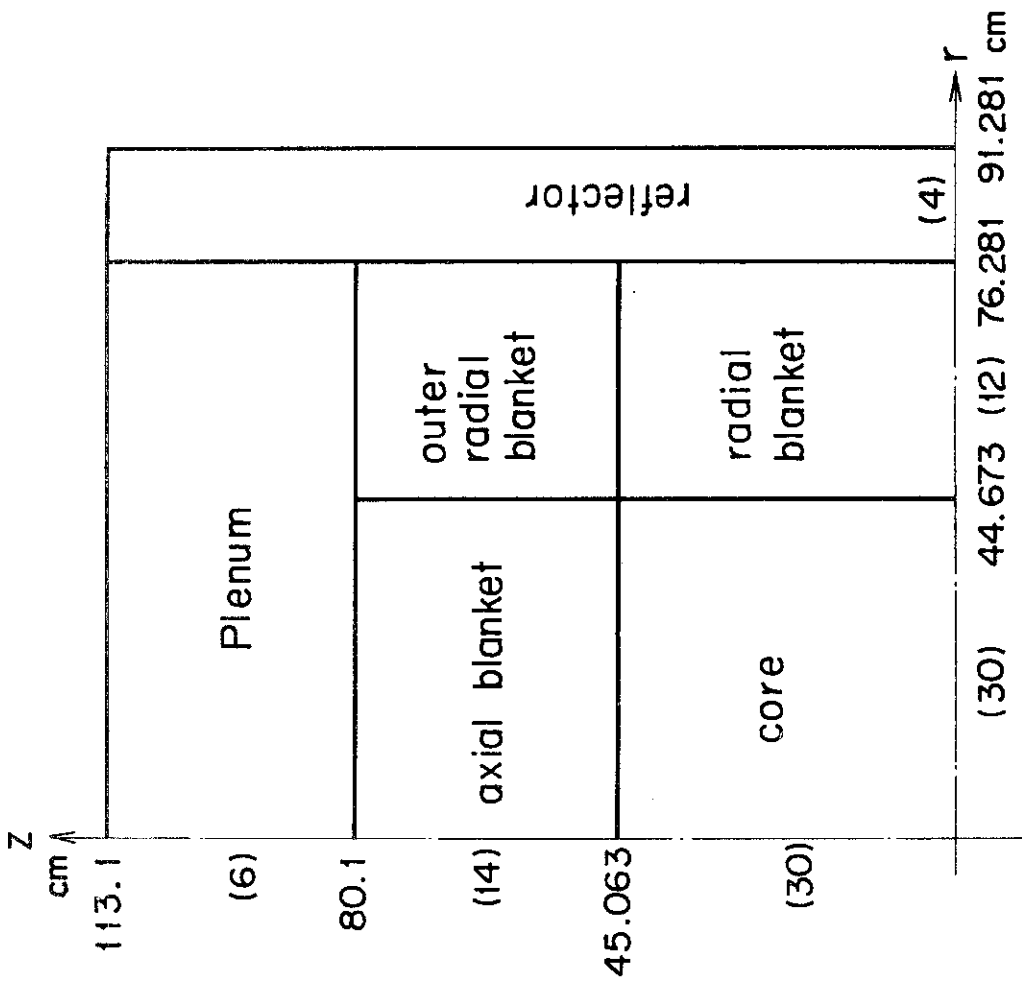
Table 4.2.12 Comparison of reactivity component by perturbation calculation for central region
($\times 10^{-6} \Delta k/k$)

Cell	Voided region	Non leakage		Leakage		Total	
		Present	UK*	Present	UK*	Present	UK*
Plate	Center cells	180	174	- 9	- 8	171	165
	Upper and lower cells	300	292	-297	-295	3	- 3
	Whole core	481	468	-308	-306	173	162
	Axial blanket	72	78	-180	-193	-108	-116
	Element	554	546	-499	-517	55	29
Pin	Center cells	212	200	- 14	- 14	198	186
	Upper and lower cells	257	245	-252	-268	5	- 23
	Whole core	470	447	-268	-286	202	161
	Axial blanket	65	71	-146	-166	- 81	- 94
	Element	534	518	-420	-466	114	52

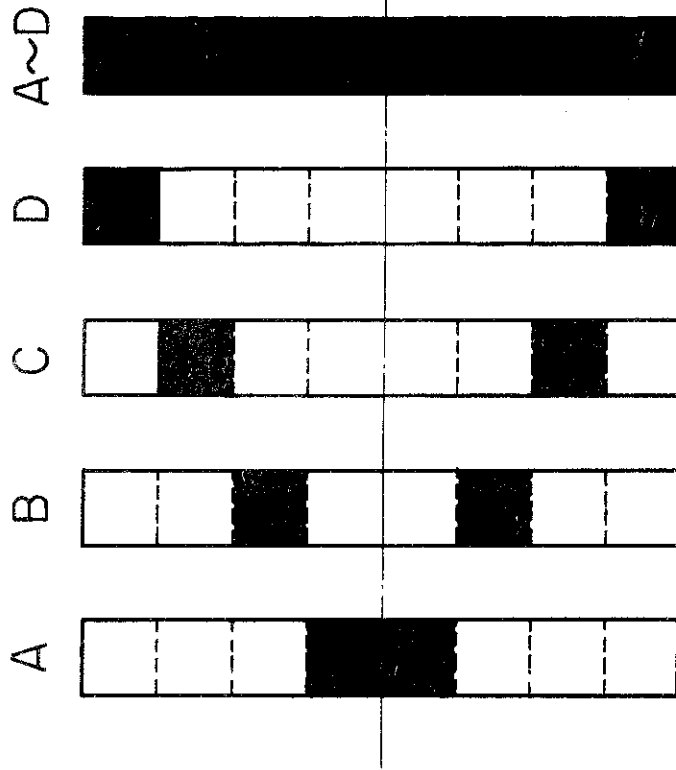
Present : JFS-V2 was used.

UK* : By Stevenson J.M. et al, Ref.(21).

These values are not corrected for the neutron streaming effect.

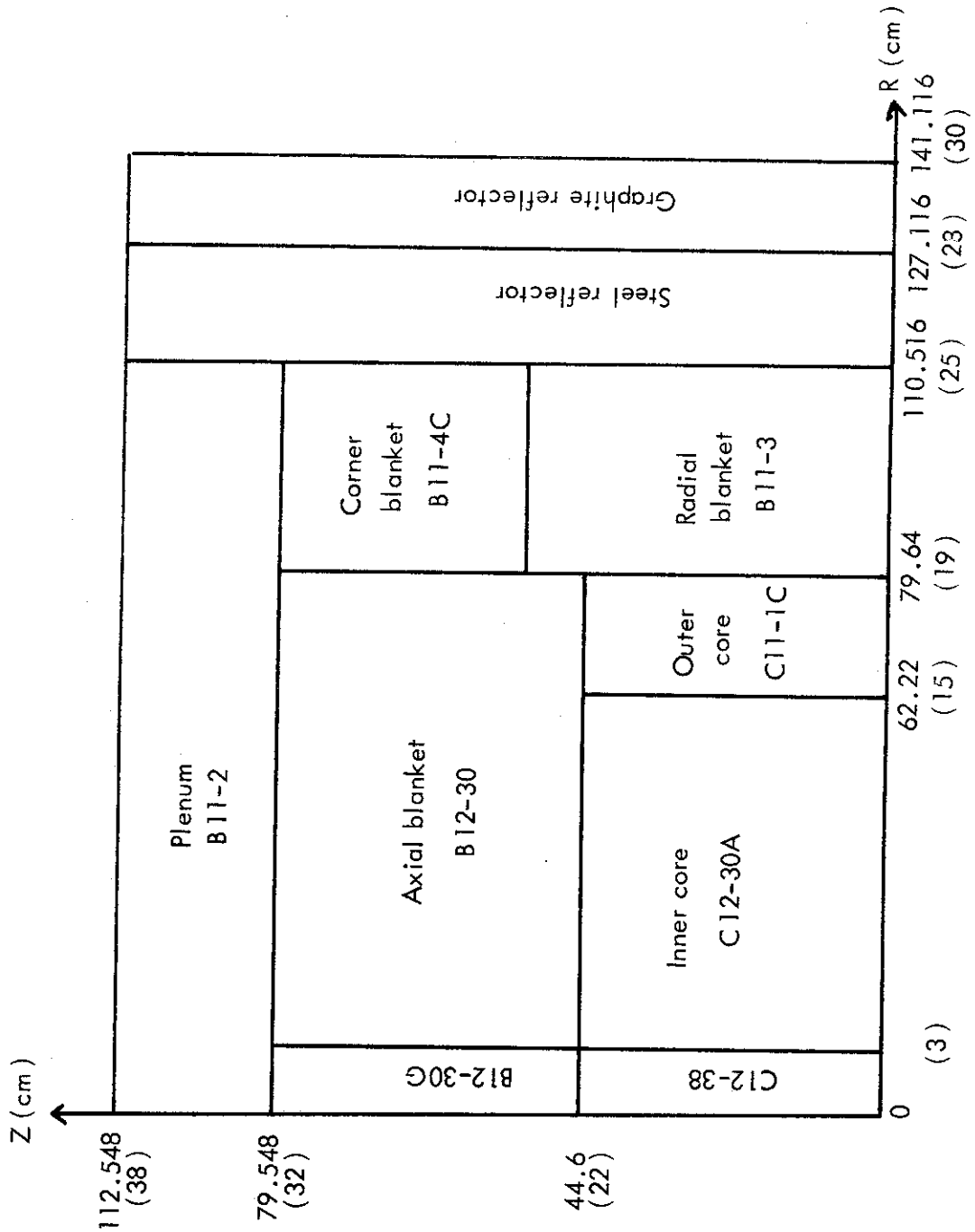


(a)



(b)

Fig.4.2.1 Calculation model and void configuration of MZA



() mesh point number

Fig.4.2.2 Calculation model and void configuration of MZB

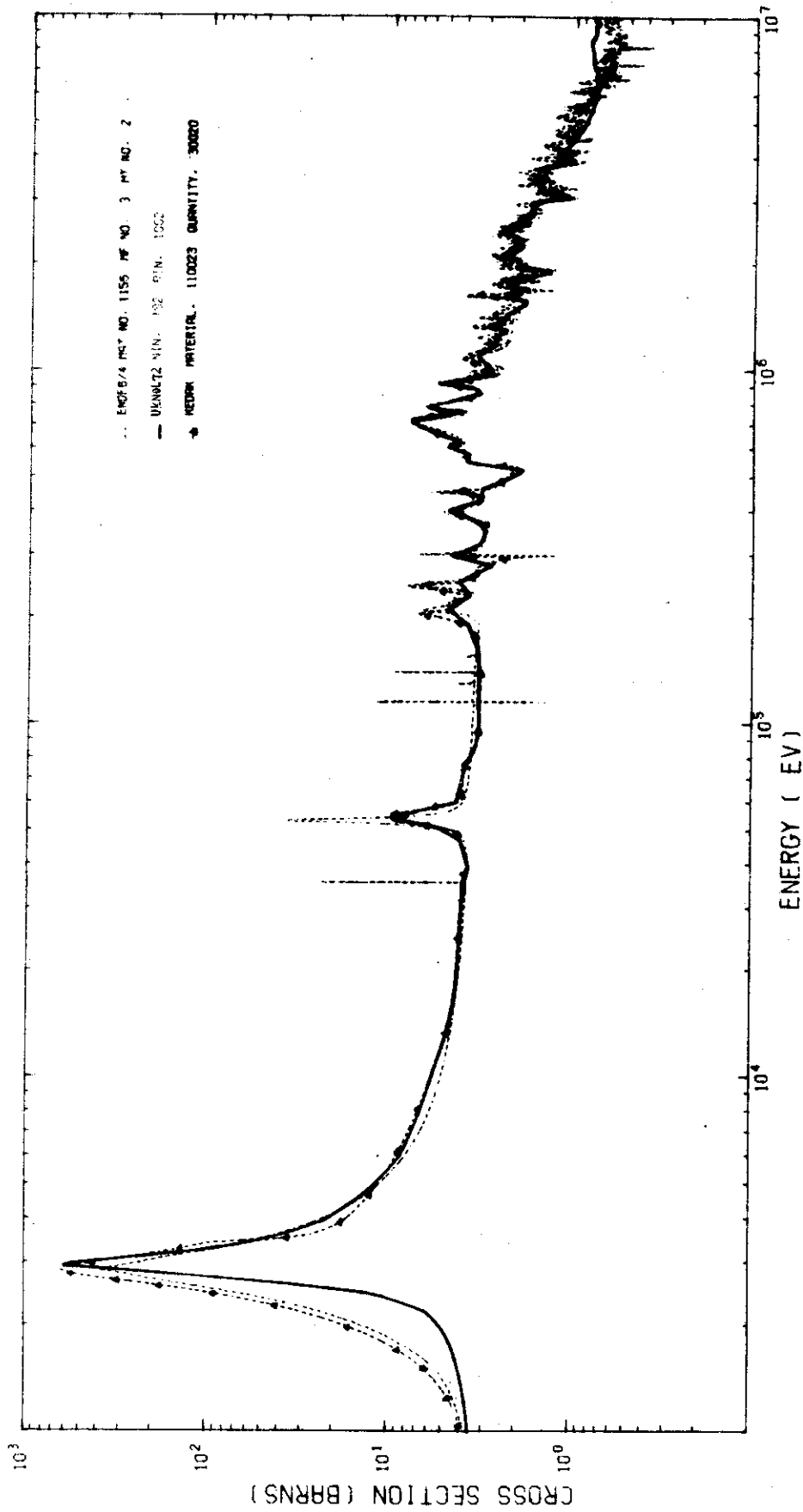


Fig.4.2.3 Comparison of elastic scattering cross sections of ^{23}Na among ENDF/B-4, UKNDL and KEDAK files

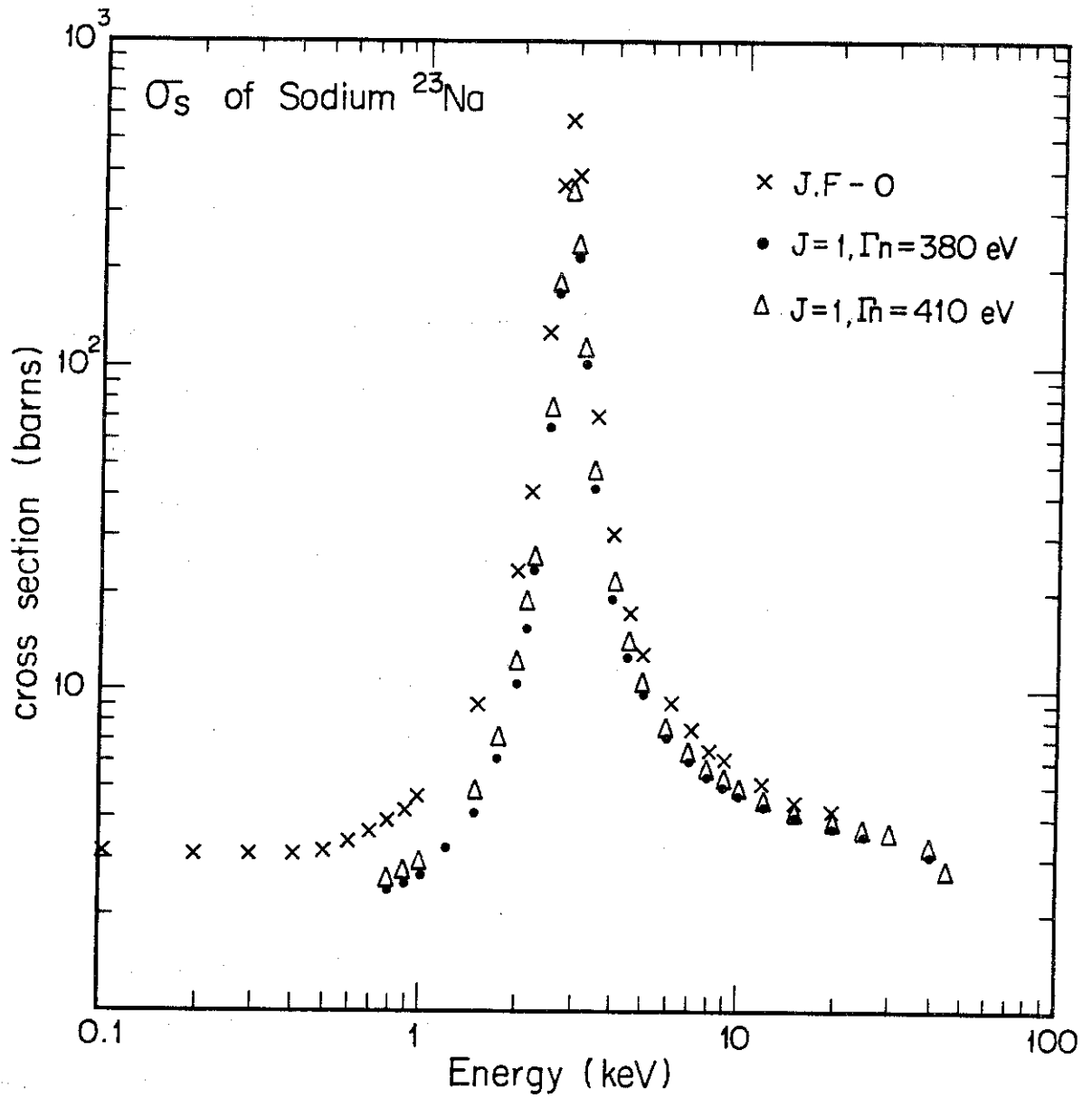


Fig.4.2.4 Sodium cross section at 2.85 keV resonance

4.3 Analysis of ZPPR Assembly 2 and Assembly 3

4.3.1 Description of Assemblies and Void Configurations

ZPPR-2 (Zero Power Plutonium Reactor Assembly 2) is a mock-up of a demonstration size plutonium fueled fast breeder reactor. The assembly regions simulate closely the mixed PuO_2/UO_2 fuel, stainless steel structure, sodium coolant and blanket compositions of a real power reactor. The core is a flattened cylinder ($H/D \sim 0.5$) with two equal-volume (about 2400 liters) zones. To provide the power flattening, the plutonium concentration in the outer core is higher by fifty percents than that in the inner core. The fuel, sodium and other simulated structural materials are in plate form and some significant quantity of mixed PuO_2/UO_2 rods is used to investigate the rod configurations. An extensive series of sodium void reactivity, Doppler effect, neutron spectrum and sample worth measurements⁽²²⁾ were performed in ZPPR-2. Among these parameters, the sodium sample worth and the large scale-sodium void reactivity measurements were analysed in this chapter.

The detailed assembly description is given by Amundson et al.⁽⁵⁹⁾ Figure 4.3.1 shows a view of the interface of ZPPR-2. The core height covered ± 45.8 cm and the equivalent radii of the inner and outer core were 64.67 cm and 91.45 cm, respectively. The plate cell patterns of the inner and outer core, and radial and axial blanket are shown in Fig.4.3.2. The inner core consists of one drawer cell, but the outer core is composed from two types of drawer cells with single or double columns of Pu-U-Mo plate. The dimension of structure matrix is illustrated in Fig.4.3.3.

The sodium void reactivities were measured at the central region of the inner core and at the interface regions of the inner and outer cores. In the latter case, the twenty five drawer sector was voided

in each region of the inner and outer cores as shown in Fig.4.3.1. In the former case, the number of voided drawers was 1, 4, 9, 21, 45, 69 or 93, and in the last case the voided region occupied 23 percents of the inner core cross-sectional area. The most cases were voided over an axial distance of $z = \pm 12$ inches.

The sample worth distributions of sodium were measured at six different axial positions, $z = 0.00, 3.036, 7.036, 11.036, 14.036$ and 22.036 in., by traversing radially from the reactor center to the outermost portion of the radial reflector. The measurements were performed in the slot environment at $z = 0.0$ and in the tunnel environment at the other locations. The sample size of sodium is 5.5 cm in length and 1 cm in diameter.

ZPPR assembly 3 was constructed with about the same core volume as the assembly 2. Experiments performed in the assembly 3 were divided into four phases, and the phase 3 simulated a stage of beginning-of-cycle condition in a burn-up cycle. Nine control rods (CR) of B_4C and ten control rod positions (CRP) filled with sodium were added to study effects of control rods on neutronics parameters. Therefore, plutonium spiked fuels were used in the plate fueled drawers in order to maintain the criticality. The cross sectional view of the core is shown in Fig.4.3.4.

The voided region was extended to an axial distance of $z = \pm 12$ in., where the sodium worth changes its sign from positive to negative. The voiding zones varied from four central drawers to 632 drawers which introduced nearly the maximum positive void worth. Sodium was removed also from CR and CRP. At the central four elements, the voided regions varied axially. These voided regions are illustrated in Fig.4.3.5 by denoting with the same symbol for each voiding stage, for which the void worths were measured. The reference core of phase 3 has

$\beta_{\text{eff}} = 0.30125 \% \Delta k/k$ and the voided core $\beta_{\text{eff}} = 0.30686 \% \Delta k/k$.

4.3.2 Methods of Analysis

In the analysis of ZPPR-2, the two-dimensional cylindrical model was employed as shown in Fig.4.3.6. The sodium voided regions with irregular boundaries were necessarily depicted as right cylinders. The adequacy of this model was examined by comparing the calculated results with those in the three-dimensional xyz model for the 69 drawers voided case.

In modeling a unit cell, the stainless steel drawer and side wall of the assembly matrix were treated as one region of stainless steel. The upper and lower matrix is uniformly diluted into the cell after obtaining the cell averaged cross sections. The heterogeneity calculations have been performed by SLAROM with use of JFS-V2. The multi-dimensional diffusion calculations were carried out by using CITATION and its output real and adjoint fluxes were used in the perturbation calculations performed by CIPER. The calculations of ZPPR-3 were made in xyz geometry, since it is improper to describe the complex configurations with CR and CRP in rz geometry, and also it is not easy to give accurately space dependent bucklings in xy or $r\theta$ geometry. Furthermore, to discuss the control rod effect on the sodium void reactivity, it is preferable to exclude an ambiguity resulted from the calculation model. We have made two-dimensional calculations in rz, xy and $r\theta$ geometry in order to examine how the criticality is affected when CRs are smeared into annular rings. The results will be discussed below. The mesh spacing in xy plane was generally one mesh per drawer (~ 5.6 cm) and the half of it at the central drawer, and in z-axis it was 3.817 cm in the core and 5.084 cm in the blanket.

The method of heterogeneity calculations was similar to the case of assembly 2. The spiked cell was treated separately with use of the same buckling value as the normal cell. Then, the macroscopic cross sections were obtained by averaging those of normal and spiked cells with the weights of the number of drawers in the inner and in the outer core, respectively. In the cell calculation of a control rod, the integral transport equation was solved for a control rod cell with the surrounding homogenized core region. Thus, the influence from the neutron spectrum in the core could be introduced into the cell averaged cross sections of CR. The diffusion coefficient of CR was obtained from the averaged transport cross section without use of Benoist's diffusion coefficient because the absorption is strong in CR. When sodium was removed from a control rod channel, it looked like a cavity. Therefore, the conventional definition of diffusion coefficient would be inadequate in this circumstance. In the present work, the modified diffusion coefficients proposed by Seki et al.⁽⁶⁰⁾ were used:

$$D_{//} = \frac{1}{3} [\lambda e^{-2r/\lambda_0} + \lambda_0 (1 - e^{-2r/\lambda_0})] ,$$

$$D_{\perp} = D_{\text{hom}} ,$$

$$D_{\text{av}} = \frac{1}{3} (2D_{//} + D_{\perp}) ,$$

where λ_0 and λ are a mean neutron transport length in CRP and its neighbouring core, respectively, and r stands for the radius of CRP.

The cell averaged cross sections with 70 groups structure were collapsed into eighteen groups by weighting with the neutron flux obtained for the one-dimensional cylindrical geometry. Then, the collapsed regions

were carefully chosen to take account of the space dependence of the neutron spectra.

As shown in Fig.4.3.4, the core of ZPPR-3 is not a quarter symmetry but a half symmetry. The right half core includes four CRs and two CRPs, but the left half core does two CRs and four CRPs. Though the flux calculations should be made for a half symmetric core, a quarter symmetric core model was adopted by considering the capacity of the core memory in computer. Therefore, the final results were obtained from the average of two runs for the left and right quarter cores.

The sample worth of sodium was measured at $z = 0$ from the center to the outermost portion of reflector. This analysis was made by the first order perturbation method.

Since the EP method is too much time-consuming to calculate many cases in the three-dimensional model, we adopted an intermediate method where the real and adjoint fluxes were only calculated for the reference core and the two voiding stages corresponding to the voided inner core and the most reactive core. In addition, the perturbations for the intermediate voiding stages were made by using appropriately these real and adjoint fluxes to approximate the exact perturbation.

4.3.3 Results and Discussions on ZPPR-2

(1) Sample Worth Distribution of Sodium

In the calculations of the small sample worth of sodium, the FOP method was used since the sample size was so small that it would not disturb the environment. The real and adjoint fluxes were obtained for xyz geometry in order to reflect the three-dimensional effect. The value

of k_{eff} was 0.9980 without including any corrections. The radial traverses are compared between the calculations and the measurements in Fig.4.3.7 at $z = 0, 7.711, 17.871, 28.031, 35.651$ and 55.971 cm. The measured values at $z = 0.0$ and 17.871 cm do not fit to a smooth curve and also have the large experimental uncertainties. We can see from the figure that the calculations give consistently more negative values than the measurements except for the results at $z = 55.971$ in the axial blanket, where a better agreement is found. The discrepancies were nearly constant over the entire radius as shown in the figure at $z = 7.711, 28.031$ and 35.651 cm. As seen from Fig.4.3.7 (g), the slot measurements at $z = 0$ are not consistent with the tunnel measurements at the other locations because of the systematic experimental errors due to the streaming effect through a slot. The observed trend of discrepancy in the sodium sample worths is similar to the results of the large scale sodium void worths as described below.

(2) Sodium Void Worth

The calculated and the measured sodium void reactivity worths are presented in Table 4.3.1. The calculated values are corrected for the neutron streaming effects. The C/E values are indeed constant, $1.10 \sim 1.20$ over the range of zone sizes from nine to 93 drawers voided for ± 30.54 cm. The C/E value for one drawer voided for ± 30.54 cm seems to be quite good but the measured value has a large experimental uncertainty. The measured value for the nine drawers voided for ± 30.54 cm is thought to be in consistent with the others because those specific worths are about $0.31 \sim 0.34 \times 10^{-4} \Delta k/k$, nevertheless the nine drawers case gives a too small value of $0.28 \times 10^{-4} \Delta k/k$. Therefore, if omitting this case it can be concluded that the calculations predict more positive

worths by 10 ~ 20 percents than the measurements for all the voided regions. The deviations of the specific worths from the measurements are consistently $6 \times 10^{-6} \Delta k/k/kg$ for the 9 ~ 93 drawers, of which the spread is apparently small. Here, it should be noted that the calculations for MZA and MZB gave more negative worths than the measurements in contrast with those for ZPPR-2. The rz model adopted here was examined its accuracy by comparing with xyz model for the 69 drawers. As shown in Table 4.3.1, the result in xyz model is smaller by 6 percents than that in rz model. The difference would be contributed mainly from the leakage component.

Table 4.3.2 shows the results for the off-central regions. These calculations were made in xyz geometry for obtaining the worths from the difference of k_{eff} (DC) or EP methods corrected and uncorrected for the neutron streaming effect. In the inner core (region A), the C/E value is consistent with those for the central zones, but in the outer core (region B) the calculation gives a fairly negative value than the measurement. The additivity of the worths for regions A and B is well realized for both the measurements and the calculations.

4.3.4 Results and Discussions on ZPPR-3

(1) Effective Multiplication Factor

The effective multiplication factors are compared in Table 4.3.3 which are obtained by using different models in two and three-dimensional calculations. It should be noted that k_{eff} by rz geometry is about three percents lower than that by xy geometry. In rz model, CRs and CRPs were smeared into annular regions with equal volumes and the disadvantage factor was not accounted in the calculation. Since this large difference is thought to be caused from the annular models of CRs, we compared k_{eff}

between other two models in $r\theta$ geometry of which configurations are shown in Fig.4.3.8. One model represents CRs and CRPs as the annular regions and the other does them as the isolated regions. The results show that the annular model is 3.5 percents smaller in k_{eff} than the isolated model which gives k_{eff} close to the xyz model. This fact means that the rz model will be inadequate for ZPPR-3 and it may be also true in the calculation of the sodium void worths. The underestimation of k_{eff} arises from the fact that in the annular model the absorption becomes larger than the isolated case as the spatial shielding effect decreases.

Moreover, Table 4.3.3 shows that the average value over the two quarter symmetric cores is in a good agreement with the value of the half core symmetric core, so this treatment will be reasonable in three-dimensional cases. The calculation in xyz geometry thus obtained predicts k_{eff} as 0.99591 which is very close to the value in the xy model mentioned above.

(2) Sample Worth Distribution of Sodium

The small sample worth traverse is compared between the calculations and the measurements in Fig.4.3.9. In this direction (negative x direction at $y = 0$ and $z = 0$), the sodium worth was measured across two CRs, so Fig.4.3.9 shows large depressions there. The calculation agrees very well with the measurement in the region, 0 ~ 90 cm, while it underestimates slightly in the interval, 90 ~ 110 cm. At the outer CR, the calculation predicts more positive value than the measurement and a more fine mesh calculation will be required to follow the deep minima.

In Fig.4.3.9, the calculated sample worth traverse is shown also in another direction (positive y direction at $x = 0$ and $z = 0$) where CRP is present at the outer boundary of the inner core ($r = \sim 65$ cm) as

seen in Fig.4.3.4. A positive peak value appears there. It can be seen that the two sample worth traverses are fairly different from each other in the region, 20 ~ 100 cm. It suggests that CR or CRP will influence significantly to the sodium void worth in their neighbourhood.

(3) Sodium Void Worth

Table 4.3.4 shows a comparison between the calculated and the measured void worths in each voiding stage. The symbols represent the voiding stages corresponding to the regions in Fig.4.3.5. In the steps A1 ~ A3, the worths were measured at the central CRP by varying axially the voided regions. The real and adjoint fluxes used in the perturbation calculations are also shown in the table. They were selected to provide approximately the unperturbed adjoint flux and the perturbed real flux for each voiding stage. The calculations were corrected for the neutron streaming effects. Examination of these calculated results reduces to the following:

- 1) At the central CRP, the C/E values of steps A1 and A2 are much lower than that for A3 in the core, which shows good agreement with the measurement. Hence, the worths will be underestimated in the axial blanket.
- 2) In the inner core, the C/E values of the most steps are 0.8 ~ 0.9, and in the outer core the sign of the worth is reverse for some steps although their absolute values are small.
- 3) For the steps B3.8 ~ B3.10 which correspond to the outer ring of CRs and CRPs or their adjacent drawers, it seems better for the perturbation formula to use ϕ_I^v and ϕ_I^{*v} , the real and adjoint fluxes in the voided state of the inner core, than to use ϕ_I^v and ϕ^* , because the

reference state of these steps are rather closer to the voided state of the whole inner core than to the reference core. Consequently, their C/E values are improved by using ϕ_I^v and ϕ_I^{*v} .

4) All the calculations give more negative worths than the measurements, showing a similar trend observed for MZA and MZB.

The cumulative voiding worths are shown in Table 4.3.5. The C/E values are 0.84 ~ 0.93 in the inner core and 0.74 ~ 0.86 in the outer core. These results are illustrated in Fig.4.3.10 where the results by FOP method is also presented. The present method (VP) is clearly superior to FOP. The radius which provides the maximum worth is slightly different between the calculation and the measurement. The deviations of specific worths (C-E)/kg are shown also in Table 4.3.5 which reveals that they are almost constant, $-4.0 \times 10^{-6} \Delta k/k$, throughout the core. Therefore, we can reflect the results to the design of demonstration reactors by using this value as the bias factor in the modification of calculations.

The results of direct k calculations are presented in Table 4.3.6 for the large voided zones. The worths are shown also in dollar units in parentheses. Taking account that the target accuracy of prediction for a large voided zone is 0.5 dollars, the present results may be satisfactory.

(4) Effect of Control Rod and Control Rod Position on Sodium Void Worth

As discussed before, CR and CRP affect significantly to the sodium sample worth, so it is interesting to examine this effect on the sodium void worth. In Table 4.3.7, the sodium void worth of a single drawer is compared among different void positions: CR, CRP, fuel drawer adjacent to CR(F/CR), fuel drawer adjacent to CRP(F/Na) and fuel drawer at the intermediate

position (Fuel). These drawers are selected both in the inner and in the outer rings of CRs and CRPs as illustrated in Fig.4.3.4. It can be concluded from the table that:

- 1) The CRP (sodium filled channel) has a negative void worth but CR a positive one for both the inner and the outer rings.
- 2) The fuel drawer at the intermediate position has the most positive worth among three fuel drawers.
- 3) The worth per drawer or per kg-Na is the most positive for CR.
- 4) The worths of F/Na and F/CR are nearly the same in the inner ring but the latter has a larger negative worth in the outer core.

To explain phenomenistically these results, the real and adjoint fluxes are shown in Figs.4.3.11 and 4.3.12, respectively. The neutron flux at Fuel is softer than that at F/CR but harder than that at F/Na. The neutron flux at CR is the lowest among all of them throughout the energy range. The adjoint spectra are almost the same for CRP, Fuel and F/Na, but at F/CR it decreases below 100 keV and attains the minimum around 10 keV. The adjoint spectrum at CR decreases monotonously with decreasing energy because of the strong absorption due to a $1/v$ capture cross section of ^{10}B . The sodium worth at CR is positive since the scattering component has a large positive values in almost all the energy range. On the other hand, the minimum of the adjoint flux at CRP is around 30 keV, so the scattering component is positive below this energy. It is interesting that the absorption term of CR is negative in contrast with other drawers. Usually, the macroscopic capture cross section of the cell decreases when sodium is lost. However, in the cell of CR, the weighting flux distribution is varied to increase the weight of boron region, accordingly to increase the cell averaged capture cross section even if sodium is voided.

Among three fuel drawers, Fuel has the most positive worth although the magnitude of the scattering term is in the order of $F/Na < Fuel < F/CR$ and that of the leakage term $F/Na > Fuel > F/CR$. In Figs.4.3.13 and 4.3.14, the adjoint and real fluxes are compared between Fuel and F/CR in the inner core. The adjoint flux at F/CR decreases with energy more steeply above 10 keV than that at Fuel, so the scattering and also the non-leakage components become more positive. In other words, CR shifts the non-leakage component of its adjacent fuel drawers to the positive side. Moreover, sodium in front of the outer CRs plays a role to shield the core from boron in CRs, so it reduces the control rod worth in the reference core. When sodium is removed, this effect is lost and consequently the sodium voiding introduces the additional negative reactivity change. As a result, it can be said that CR or CRP may cause the change of the sodium void worth by several tens of percents at the neighbouring fuel region. Hence the spatial distribution of the sodium void worth is substantially distorted by CRs. In addition, it should be noted that CR has a large positive void worth. The influence of CR on the cell averaged cross sections of fuel regions is not accounted in the present investigation.

Table 4.3.1 Sodium void worth at core center of ZPPR-2
 ($10^{-4} \Delta k/k$)

Number of drawers (Equivalent radius)	Axial length , cm	Sodium removed , kg	Experiment E.	Calculation			(C-E)/kg
				C.	Streaming effect	C/E	
1 (3.989 cm)	0. ~ 15.27	0.169	0.0735 ± .0007	0.090	-0.001	1.23 ± .01	0.10
	±30.54	0.660	0.247 ± .079	0.245	-0.009	0.99 ± .32	-0.003
4 (6.378 cm)	±30.54	2.641	0.896 ± .079	0.992	-0.035	1.11 ± .09	0.036
	±45.81	3.961	0.532 ± .079	0.611	-0.100	1.15 ± .15	0.020
9 (9.567 cm)	±15.27	2.969	1.44 ± .079	1.64	-0.010	1.14 ± .05	0.067
	±30.54	5.942	1.67 ± .079	2.25	-0.078	1.35 ± .05	0.098
21 (14.614 cm)	±30.54	13.866	4.47 ± .079	5.27	-0.177	1.18 ± .02	0.058
	±30.54	29.714	9.37 ± .079	11.3	-0.369	1.21 ± .01	0.066
69 (26.491 cm)	±30.54	45.562	14.47 ± .079	17.3	-0.556	1.20 ± .01	0.062
	±30.54	61.410	19.50 ± .079	16.3 ^a	-0.743	1.13 ± .01 ^a	0.040 ^a
93 (30.755 cm)	±30.54			23.2		1.19 ± .00	0.060

a. Obtained by three-dimensional diffusion calculation

Ih = 1015.7% $\Delta k/k$

Table 4.3.2 Sodium void worth at off-center of ZPPR 2

 $(\times 10^{-4} \Delta k/k)$

Voided region	Experiment	Calculation		
		DC	EP*	C/E
Inner core A	3.72±.08	4.55	4.28 4.19	1.12±.02
Outer core B	-1.52±.08	-2.98	-2.82 -2.15	1.42±.05
Inner + Outer cores, A + B	2.14±.10	1.51	1.42 2.02	0.94±.05












* Lower values are corrected for the neutron streaming effects.

Table 4.3.3 Comparison of effective multiplication factor

Geometry	Comment	k_{eff}
R-Z		0.96384
X-Y	Half core	0.99625
X-Y	Average of 1/4 symmetric core	0.99659
R- θ	Annular CR & CRP	0.96422
R- θ	Isolated CR, & CRP	1.00084
X-Y-Z	Right 1/4 symmetric core	0.98974
X-Y-Z	Left 1/4 symmetric core	1.00208
X-Y-Z	Average of 1/4 symmetric core	0.99591
X-Y-Z	Right 1/4 symmetric core with voided inner core	0.99518

Table 4.3.4 Comparison between calculation and measurement for sodium void worth in step at ZPPR 3, phase 3

($10^{-4} \Delta k/k$)

Voiding stage	Total drawers voided per half (in step)	Experiment	Calculation	C/E	Real and adjoint flux
A.1	4 (±36 in.)	- 3.18	- 2.11	0.66	ϕ , ϕ^*
A.2	4 (±18 in.)	2.45	1.55	0.63	ϕ , ϕ^*
A.3	CRP-1 4 (±12 in.)	1.27	1.41	1.11	ϕ , ϕ^*
A.4	 42 (+38)	8.318	7.332	0.88	ϕ_I^v , ϕ^*
B.3.1	 60 (+18)	4.290	3.408	0.79	ϕ_I^v , ϕ^*
B.3.2	 100 (+40)	8.328	6.954	0.84	ϕ_I^v , ϕ^*
B.3.3	 146 (+46)	11.26	11.07	0.98	ϕ_I^v , ϕ^*
B.3.4	 188 (+42)	8.767	7.262	0.83	ϕ_I^v , ϕ^*
B.3.5	 228 (+40)	7.948	6.156	0.77	ϕ_I^v , ϕ^*
B.3.6	 278 (+50)	7.438	5.586	0.75	ϕ_I^v , ϕ^*
B.3.7	 324 (+46)	5.413	4.392	0.81	ϕ_I^v , ϕ^*
B.3.8	 358 (+34)	4.054	2.425	0.60	ϕ_I^v , ϕ^*
		*	3.226	0.80	ϕ_I^v , ϕ^{*v}
B.3.8a	 370 (+12)	- 0.5462	- 1.014	1.86	ϕ_I^v , ϕ^*
		*	- 0.742	1.36	ϕ_I^v , ϕ^{*v}
B.3.9	 410 (+40)	1.982	1.022	0.52	ϕ_I^v , ϕ^*
		*	2.739	1.38	ϕ_I^v , ϕ^{*v}
B.3.10	A 434 (+24)	3.903	2.780	0.71	ϕ_o^v , ϕ_I^{*v}
11	B 480 (+46)	3.777	2.047	0.54	ϕ_o^v , ϕ_I^{*v}
12	C 500 (+20)	0.8377	0.1800	0.21	ϕ_o^v , ϕ_I^{*v}
13	D 522 (+22)	1.028	- 0.2573	—	ϕ_o^v , ϕ_I^{*v}
14	E 542 (+20)	0.2639	- 0.4878	—	ϕ_o^v , ϕ_I^{*v}
15	F 566 (+24)	0.8224	- 0.6051	—	ϕ_o^v , ϕ_I^{*v}
16	G 586 (+20)	1.694	0.2709	0.16	ϕ_o^v , ϕ_I^{*v}
17	H 608 (+22)	- 1.019	- 2.253	2.21	ϕ_o^v , ϕ_o^{*v}
18	I 632 (+24)	0.1596	- 0.9305	—	ϕ_o^v , ϕ_o^{*v}

ϕ : Normal flux, ϕ^* : Normal adjoint flux
 ϕ_I^v : Inner core void flux, ϕ_I^{*v} : Inner core void adjoint flux
 ϕ_o^v : Maximum void worth flux, ϕ_o^{*v} : Maximum void worth adjoint flux

Table 4.3.5 Comparison between calculation and measurement for cumulative voiding worth at ZPPR 3, phase 3

($10^{-4} \Delta k/k$)

Voiding stage	Calc.	C/E	(C-E)/kg
A3	0.8559	0.93	-0.012
A4	8.188	0.89	-0.035
B.3.1	11.60	0.86	-0.046
B.3.2	18.55	0.85	-0.048
B.3.3	26.62	0.89	-0.059
B.3.4	36.88	0.88	-0.036
B.3.5	43.04	0.86	-0.041
B.3.6	48.62	0.85	-0.044
B.3.7	53.15	0.85	-0.041
B.3.8	56.38	0.85	-0.041
B.3.8a	55.63	0.84	-0.040
B.3.9	58.37	0.86	-0.033
B.3.10	61.15	0.85	-0.035
B.3.11	63.20	0.83	-0.037
B.3.12	63.38	0.83	-0.038
B.3.13	63.12	0.81	-0.040
B.3.14	62.63	0.80	-0.038
B.3.15	62.03	0.79	-0.043
B.3.16	62.30	0.77	-0.045
B.3.17	60.05	0.76	-0.046
B.3.18	59.12	0.74	-0.047

Table 4.3.6 Comparison between calculation and measurement for large scale sodium void worth in ZPPR 3

Voided region	Experiment	Calculation	C/E(C-E)\$
Inner core	68.17 (2.22 \$)	60.88 (1.98 \$)	0.89 (-0.24 \$)
Maximum void worth region	80.50 (2.62 \$)	65.38 (2.13 \$)	0.81 (-0.49 \$)

Calculated values were obtained from the differences of direct k calculations.

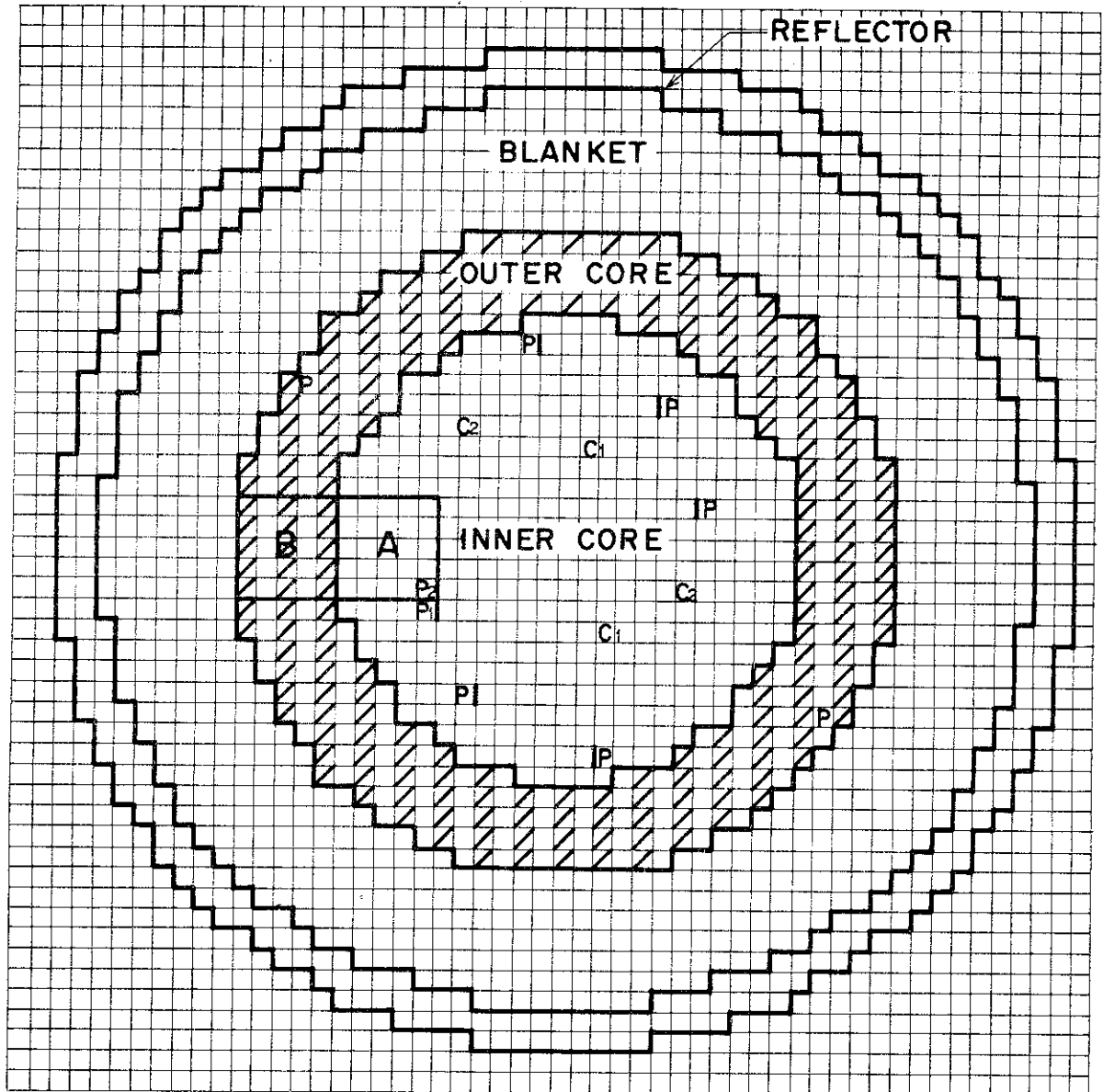
Table 4.3.7 Comparison of sodium void worth at Na-CRP, CR and neighbouring fuel regions

($10^{-6} \Delta k/k$)

Position	Total	Absorption	Fission	Scattering	Leakage
Inner Core					
CRP	- 66.79 (-12.63)	42.35	0.0	200.1 (37.80)	-309.3 (-58.49)
F/Na	23.03 (8.732)	39.19	-29.39	107.2 (40.65)	- 93.97 (-35.63)
Fuel	38.67 (14.66)	37.85	-29.84	133.0 (50.43)	-102.3 (-38.80)
F/CR	24.50 (9.364)	30.51	-27.06	192.6 (73.04)	-171.4 (-64.98)
CR	135.0 (35.17)	-60.38	0.0	420.6 (109.6)	-225.2 (-58.69)
Outer Core					
CRP	- 54.73 (-10.35)	27.36	0.0	112.7 (21.31)	-194.7 (-36.83)
F/Na	- 19.46 (-7.94)	24.75	-21.64	59.69 (23.7)	- 82.26 (-32.71)
Fuel	- 15.80 (-6.283)	23.34	-20.63	74.05 (29.44)	- 92.56 (-36.80)
F/CR	- 32.78 (-13.03)	13.20	-13.34	104.7 (41.62)	-137.3 (-54.60)
CR	50.01 (27.92)	-19.36	0.0	149.3 (83.74)	- 79.91 (-44.61)

() : /kg-Na

Sodium weight : Inner core fuel=2.637 kg, Outer core fuel=2.515 kg,
Na-CRP=5.287 kg, CR(I/C)=3.838 kg, CR(O/C)=1.791 kg



- ▨ OUTER CORE DOUBLE COLUMN DRAWERS
- ▤ CONTROL RODS C₁ - HALF 1, C₂ - HALF 2
- ▥ POISON SAFETY (OR SHIM) RODS

HALF 2 IS MIRROR IMAGE
OF HALF 1

Fig.4.3.1 Interface view of ZPPR 2 and location of off-central voided regions

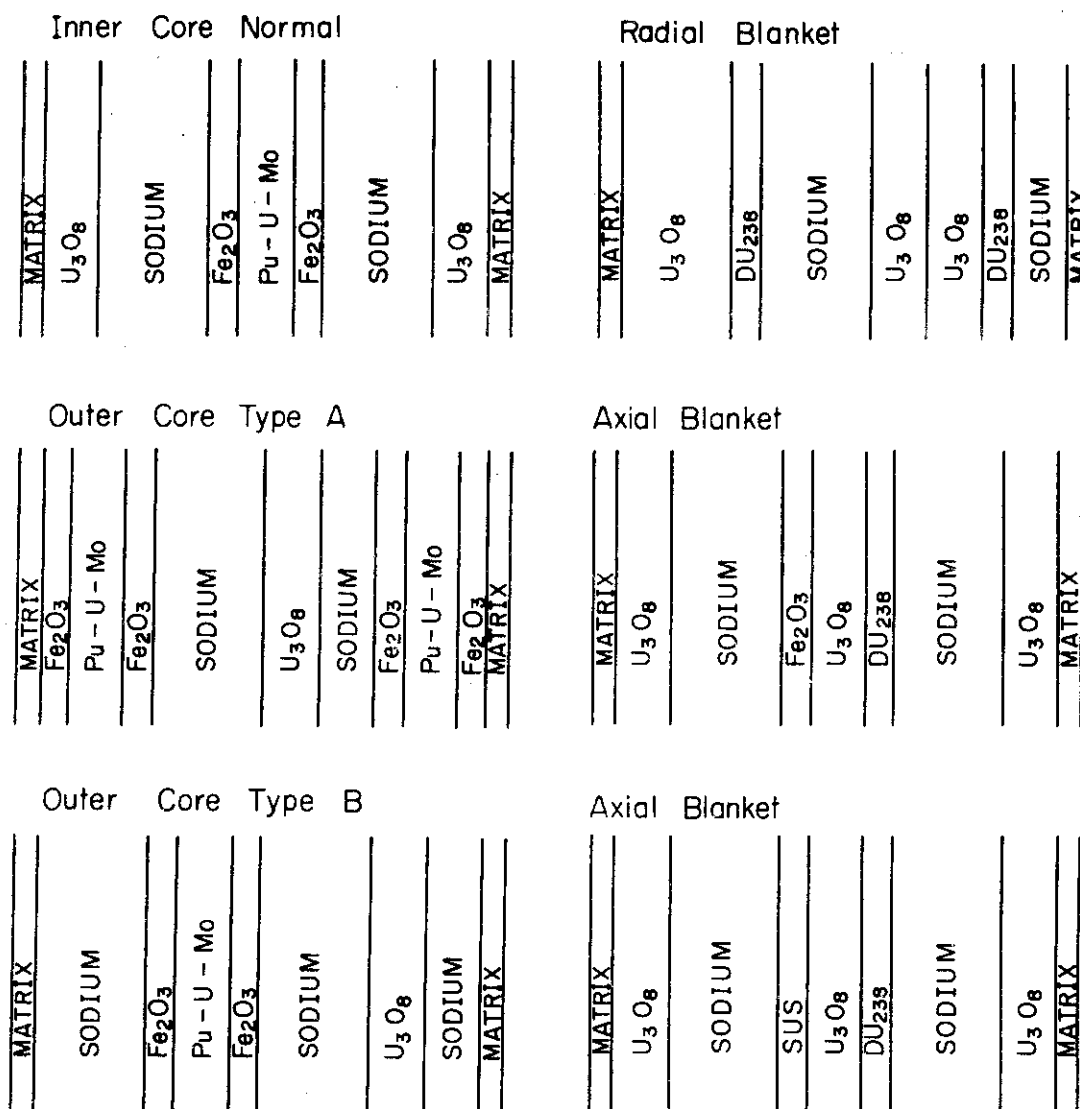


Fig.4.3.2 Cell structure of ZPPR 2

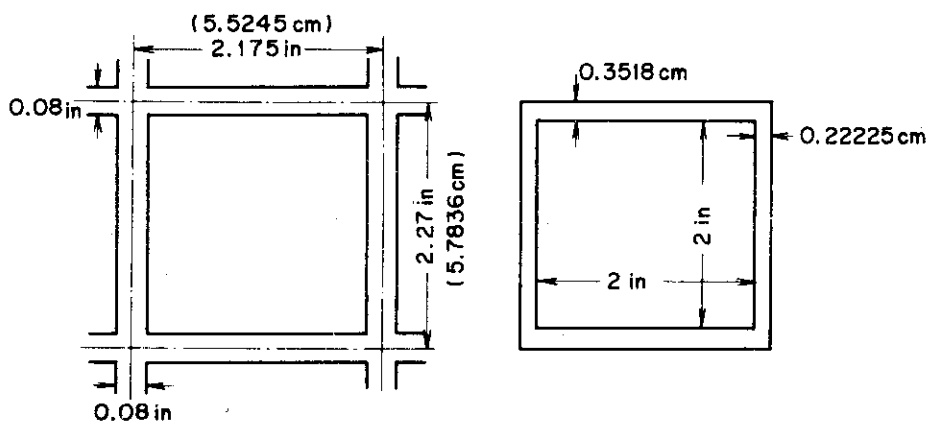
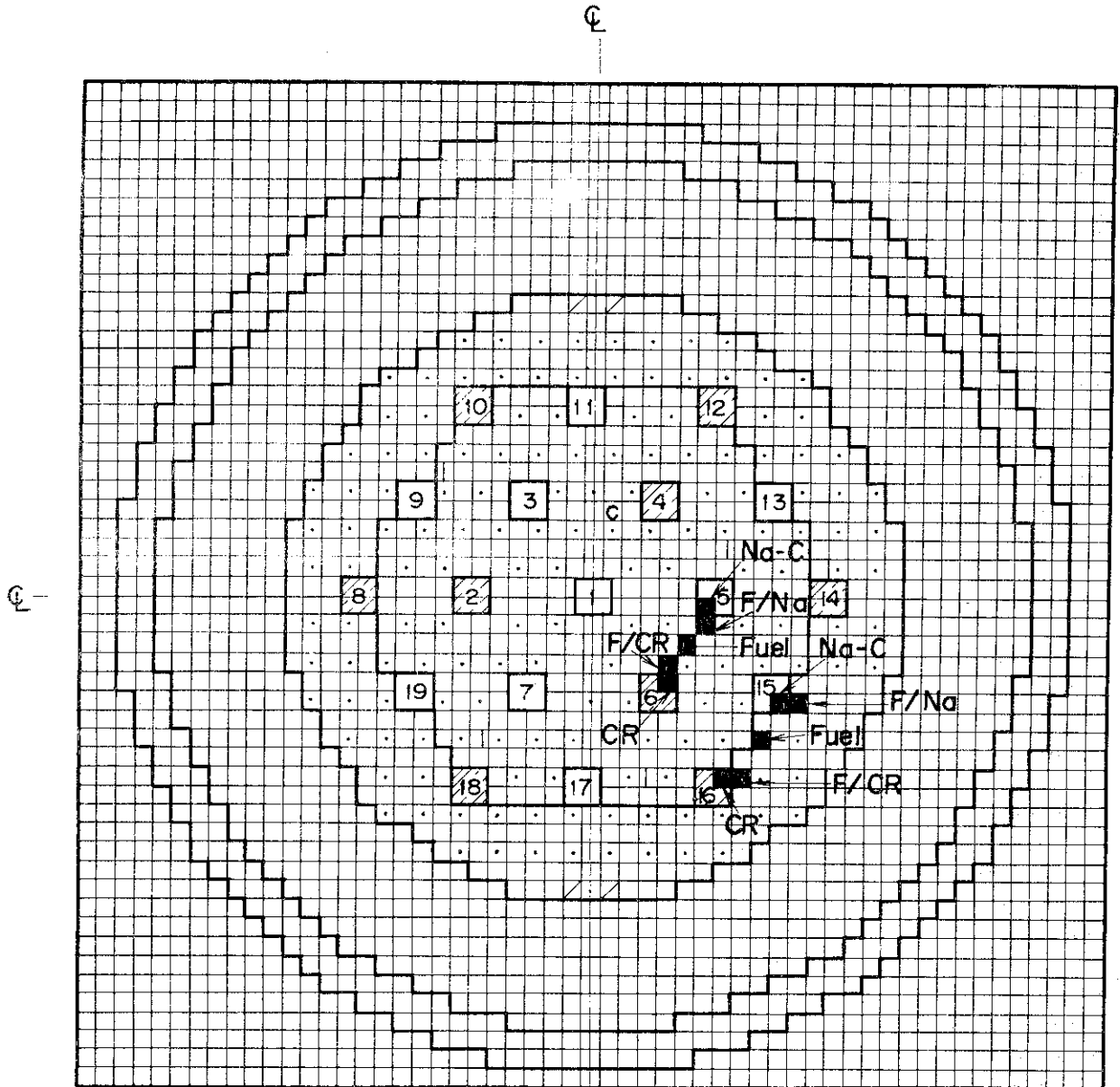


Fig.4.3.3 Dimension of structure matrix



- CRP
 B₄C LOADED CRP
- SPIKED CORE DRAWERS
 EXTRA TYPE A DRAWERS
- SODIUM VOIDING DRAWERS

Fig.4.3.4 Reference loading of ZPPR 3, Phase 3

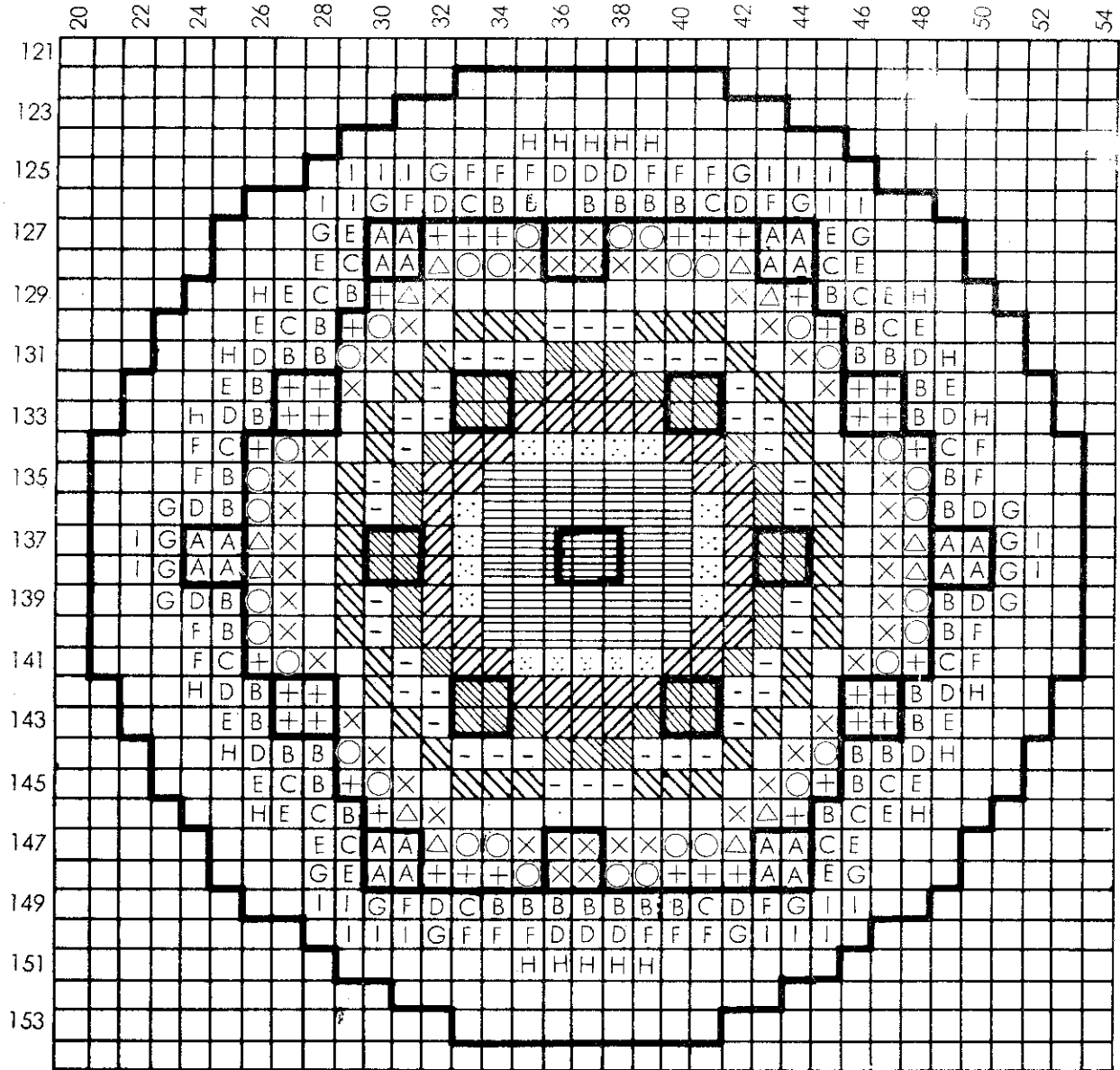


Fig.4.3.5 Stages of sodium voiding experiment in ZPPR 3, Phase 3

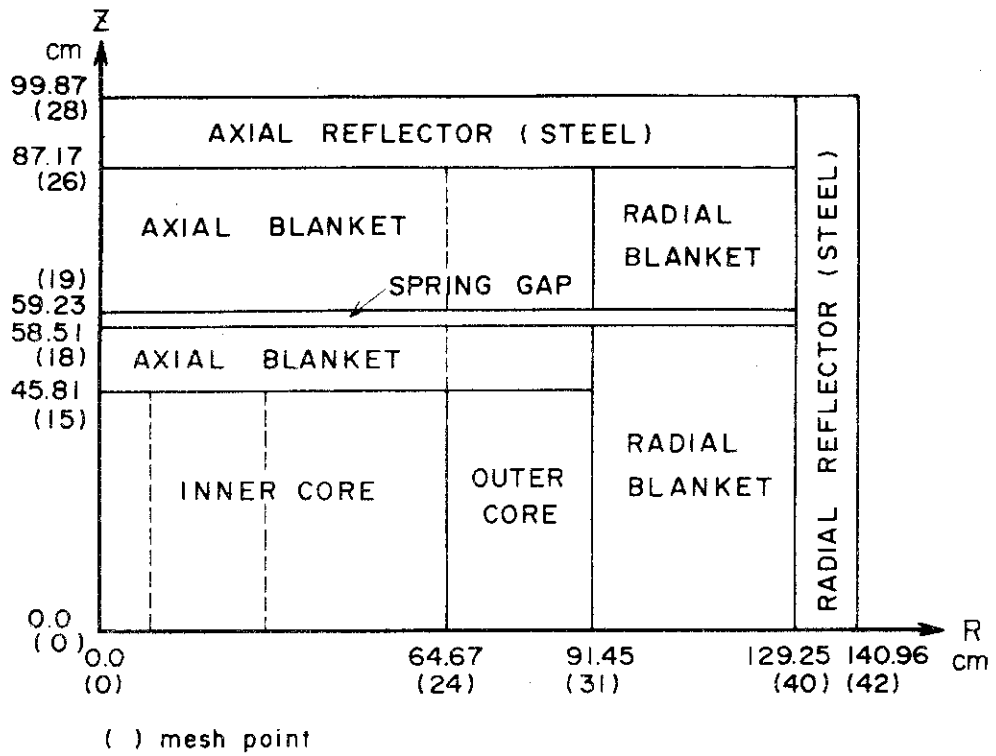


Fig.4.3.6 Cylindrical model of ZPPR 2

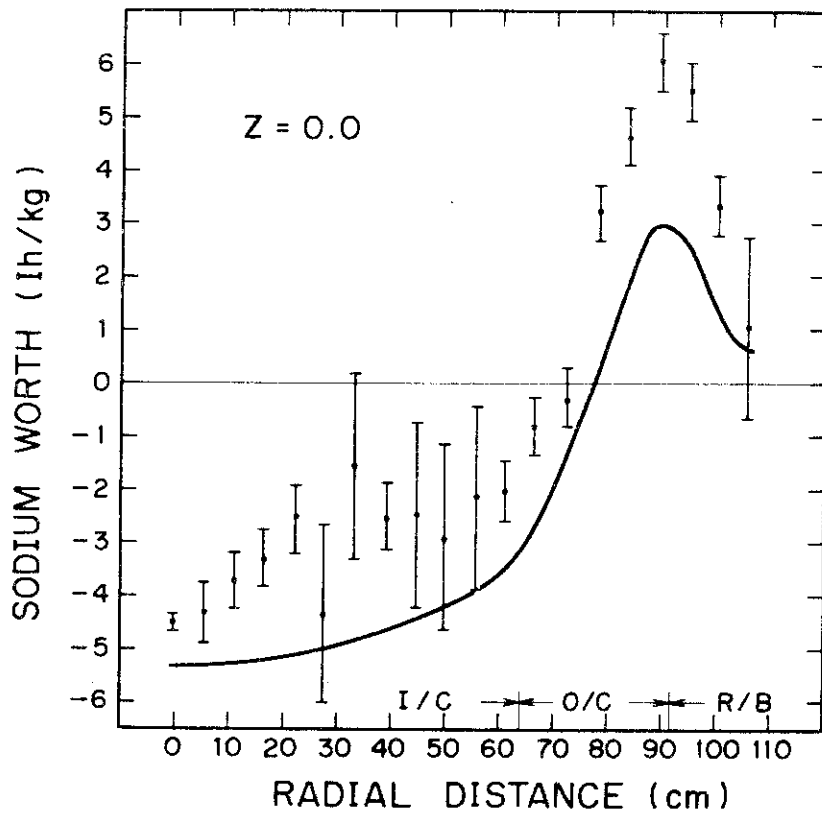


Fig.4.3.7 Sample worth distribution of sodium in ZPPR 2

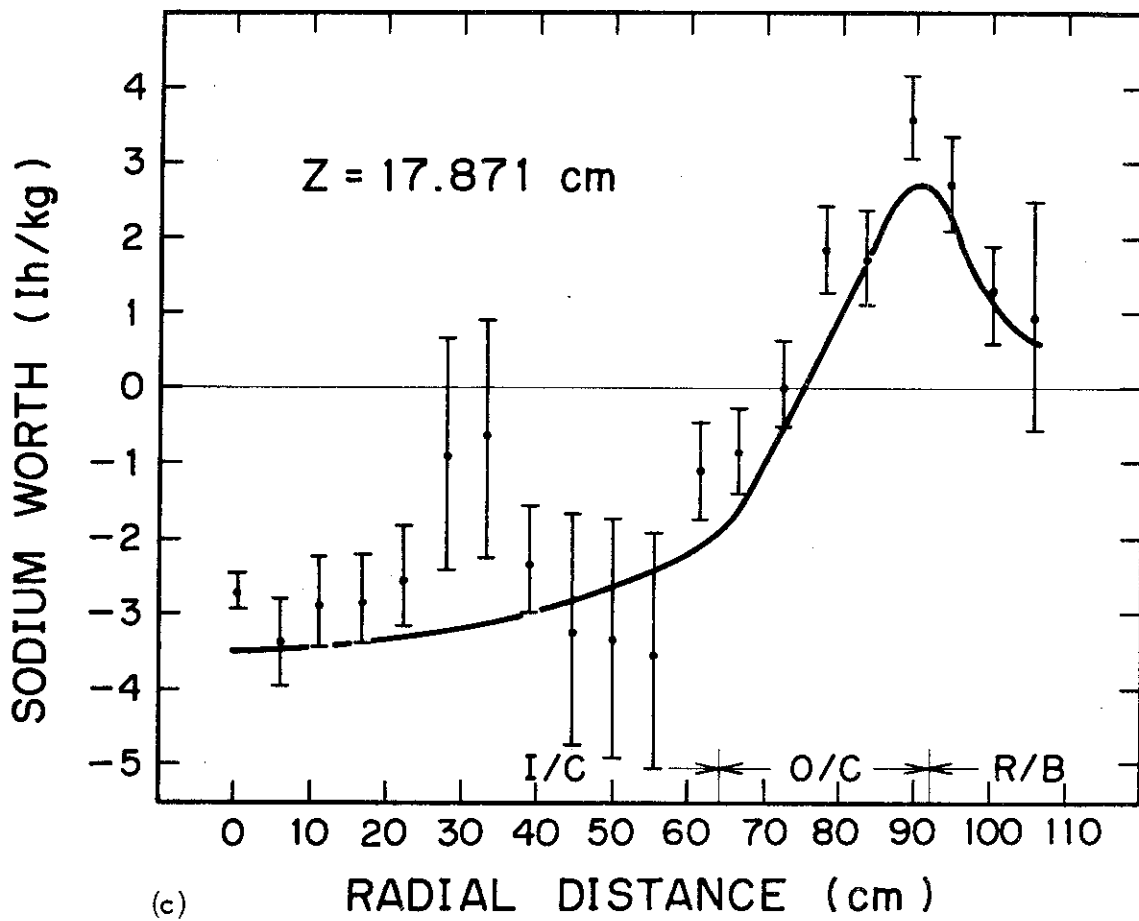
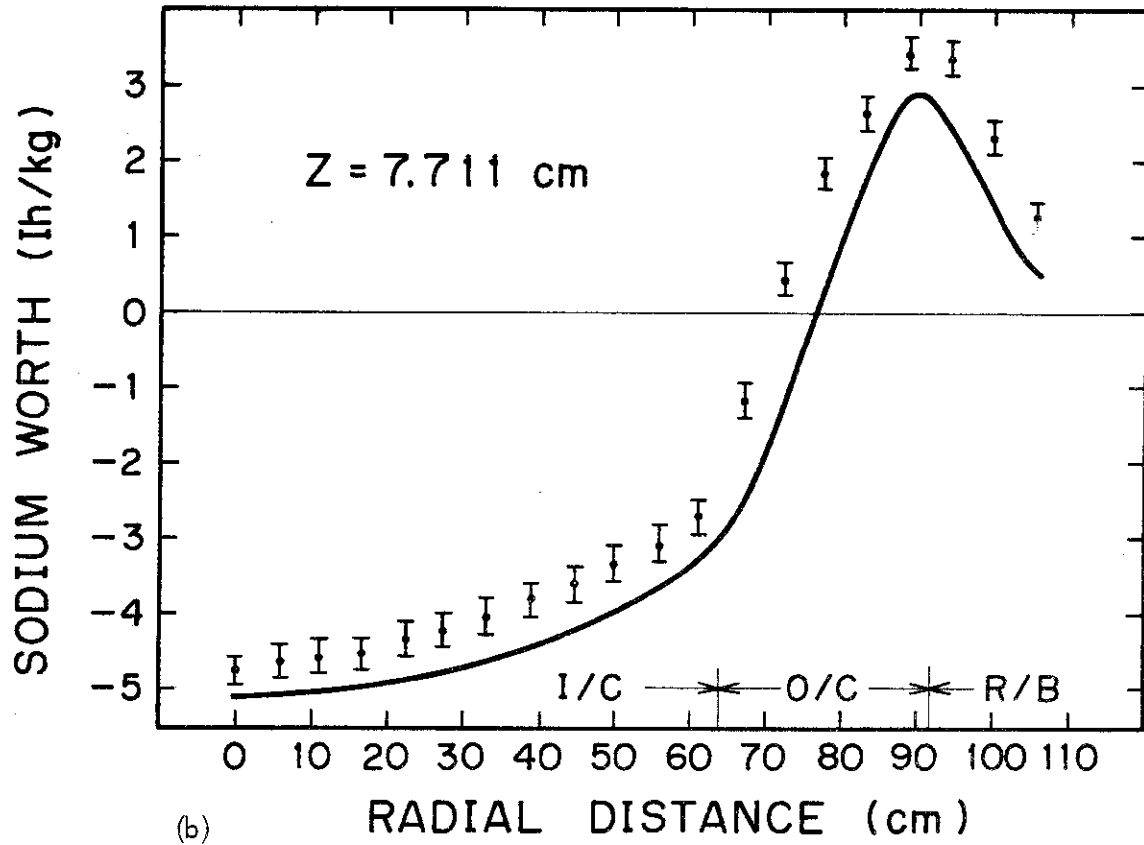


Fig.4.3.7 (continued)

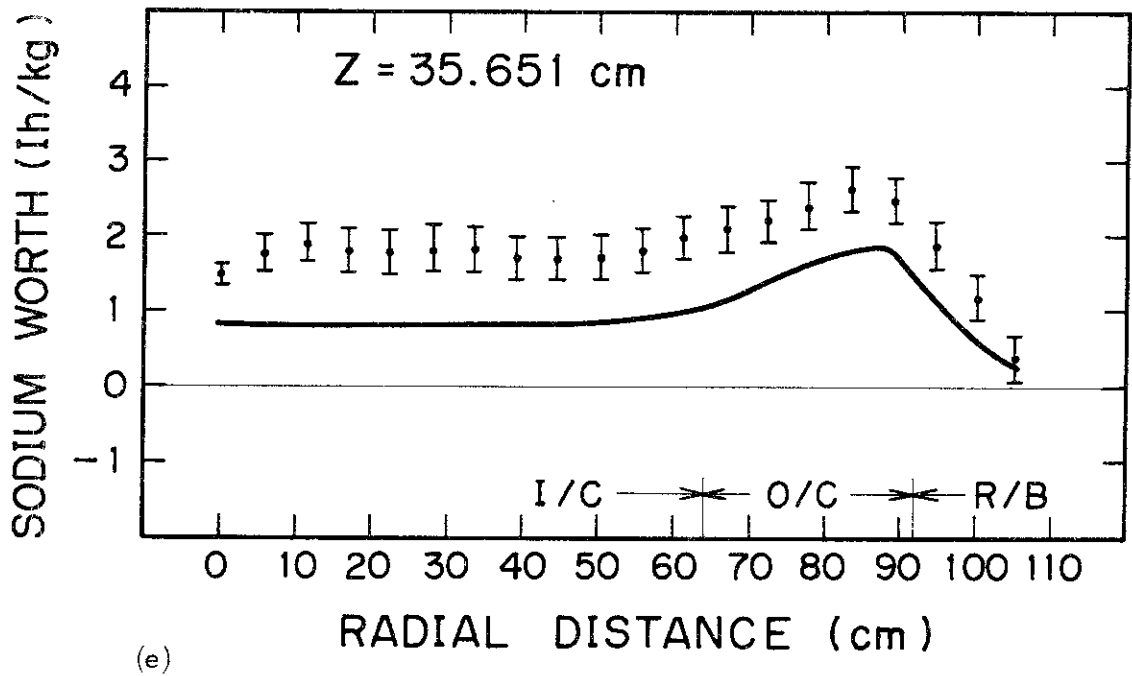
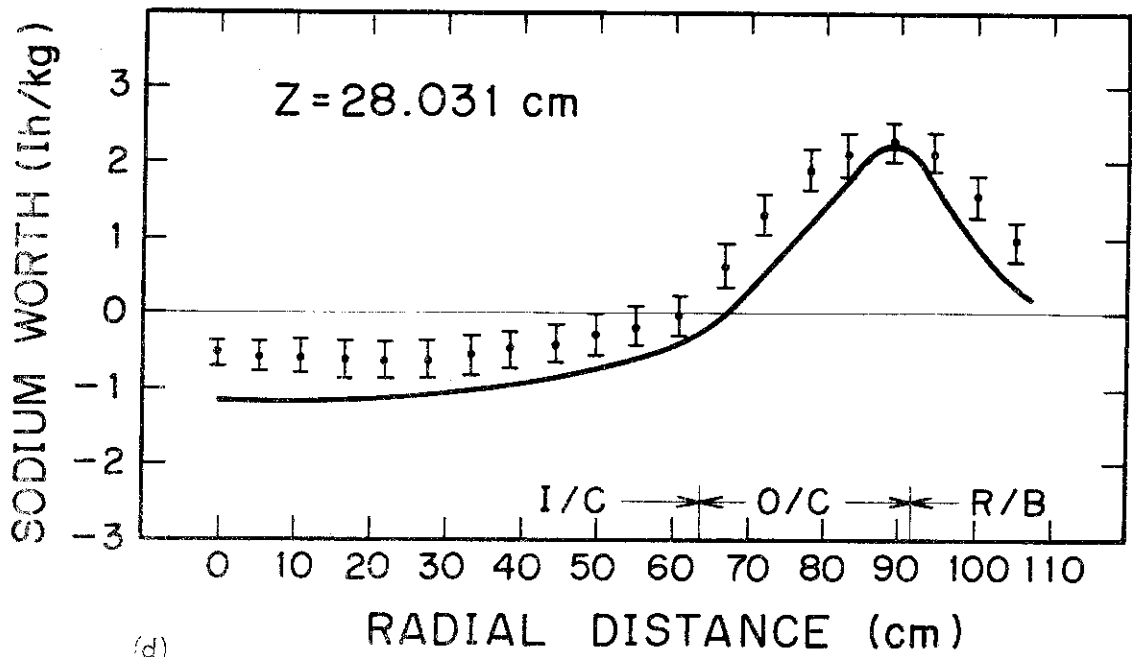


Fig.4.3.7 (continued)

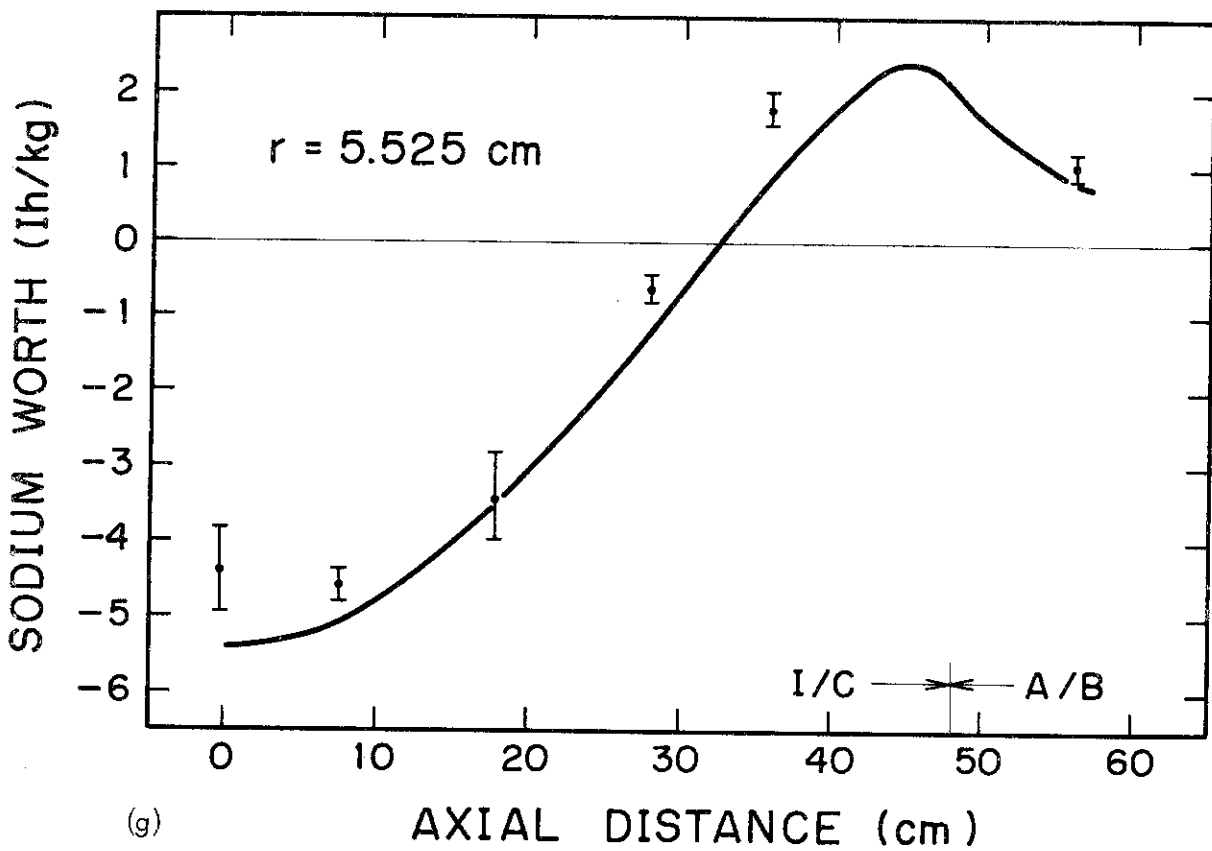
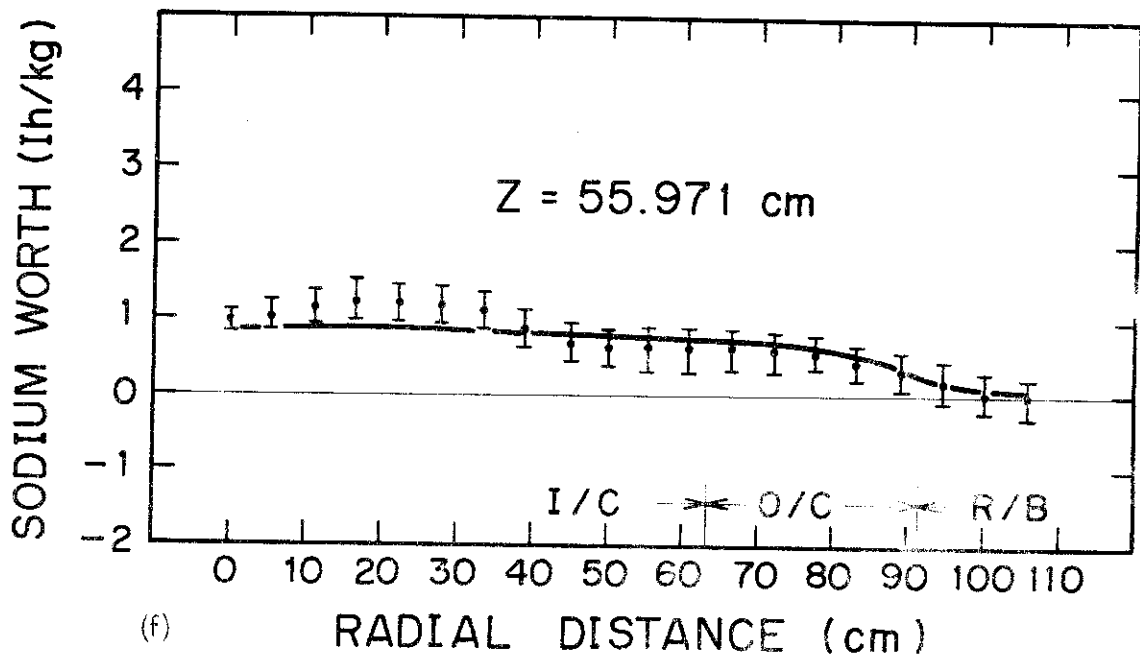
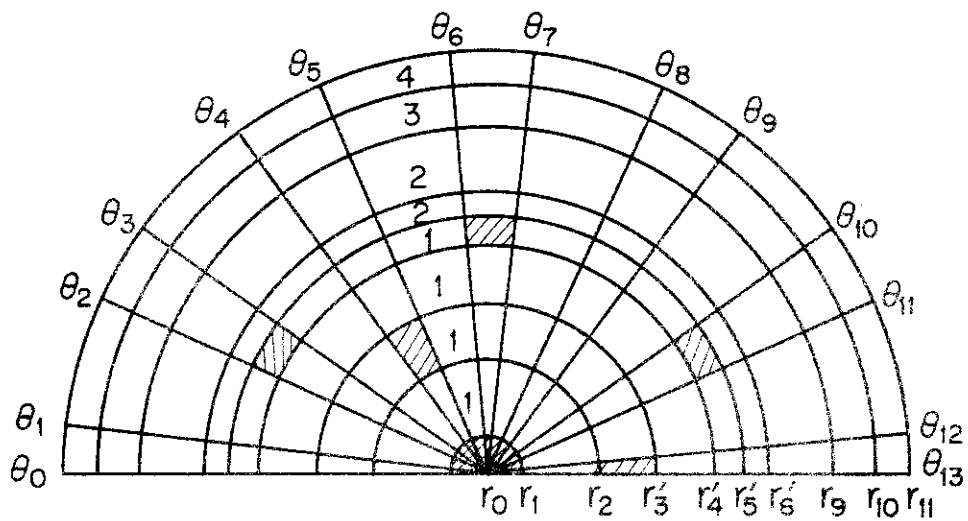
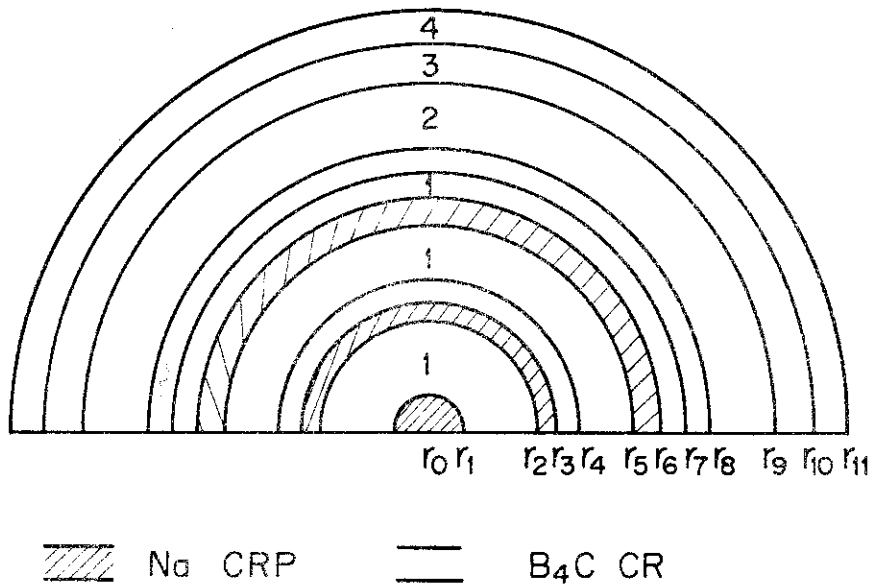


Fig.4.3.7 (continued)



- 1 : Inner Core
- 2 : Outer Core
- 3 : Radial Blanket
- 4 : Radial Reflector

Fig.4.3.8 R-θ model of ZPPR 3, Phase 3

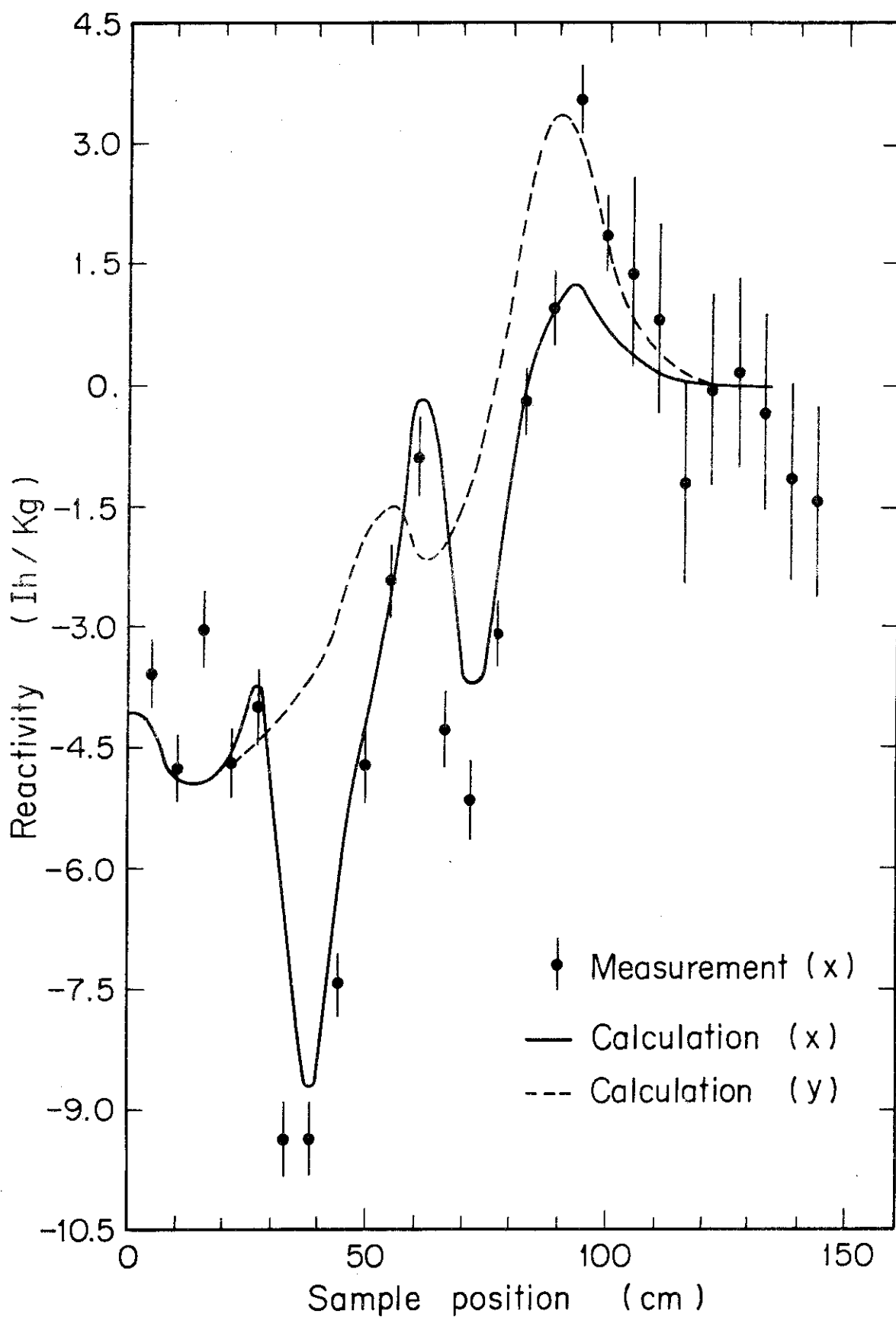


Fig.4.3.9 Sample worth distribution of sodium in ZPPR 3, Phase 3

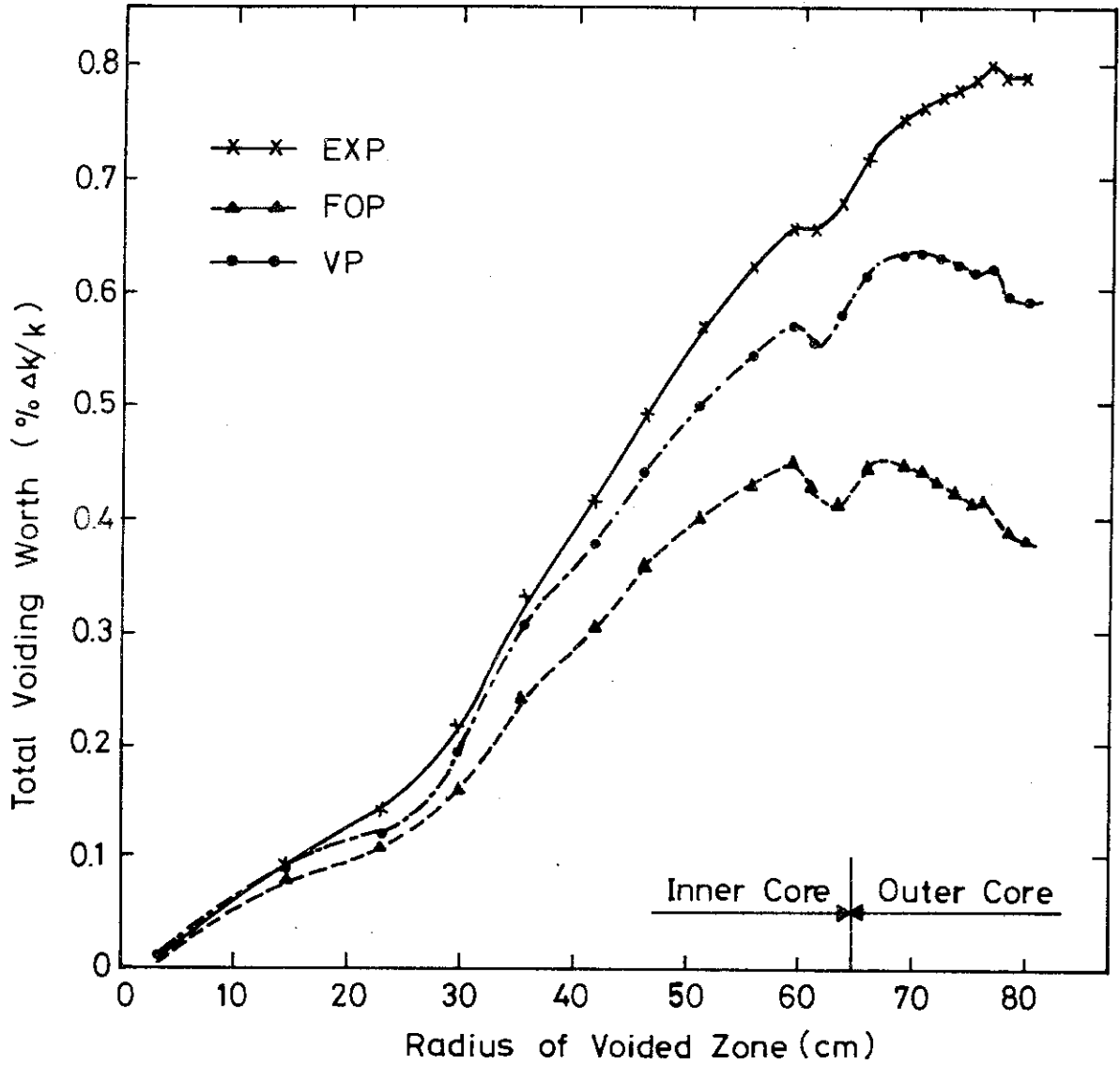


Fig.4.3.10 Cumulative sodium void worth in ZPPR 3, Phase 3

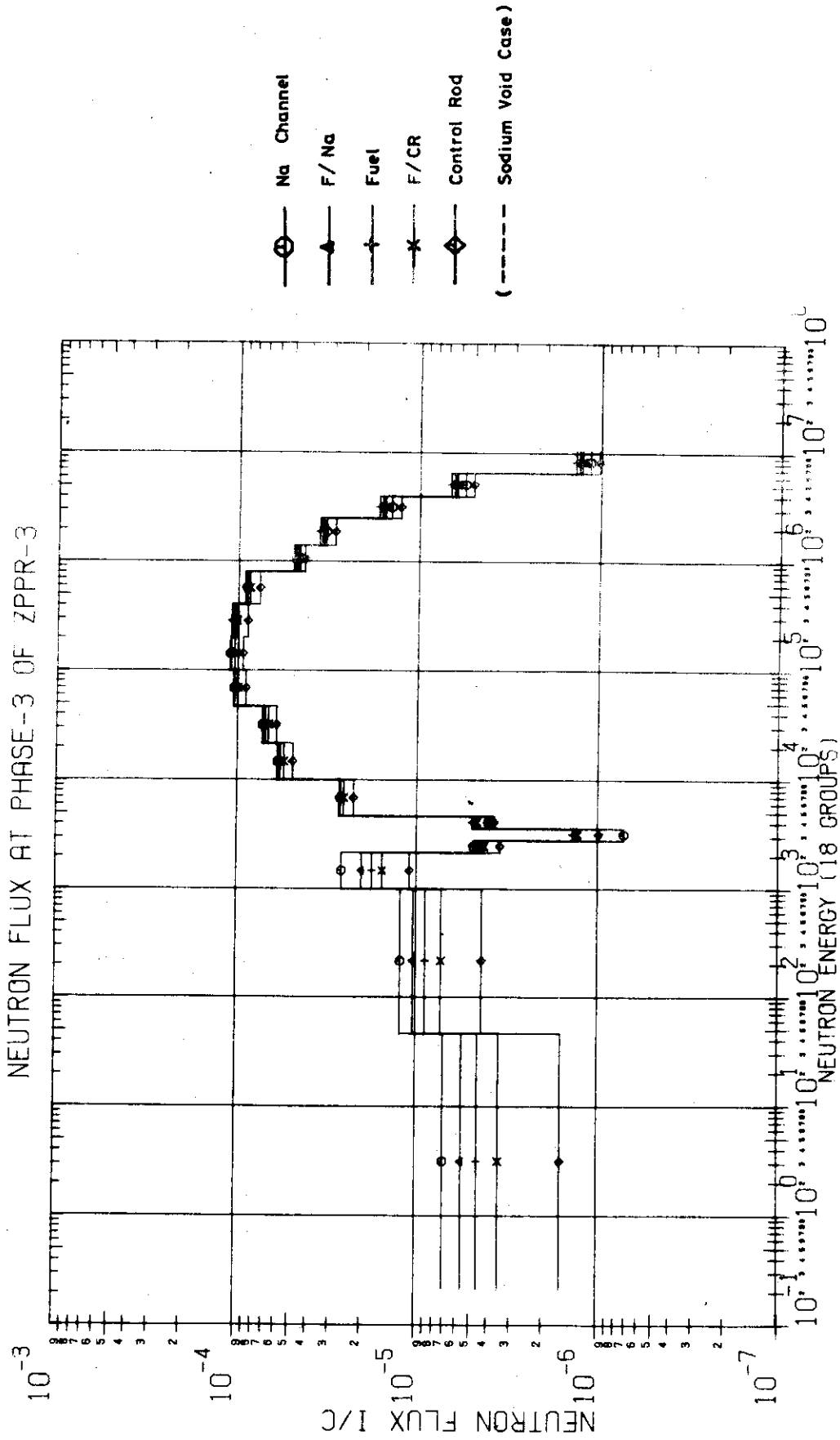


Fig.4.3.11 Neutron flux in inner core of ZPPR 3, Phase 3

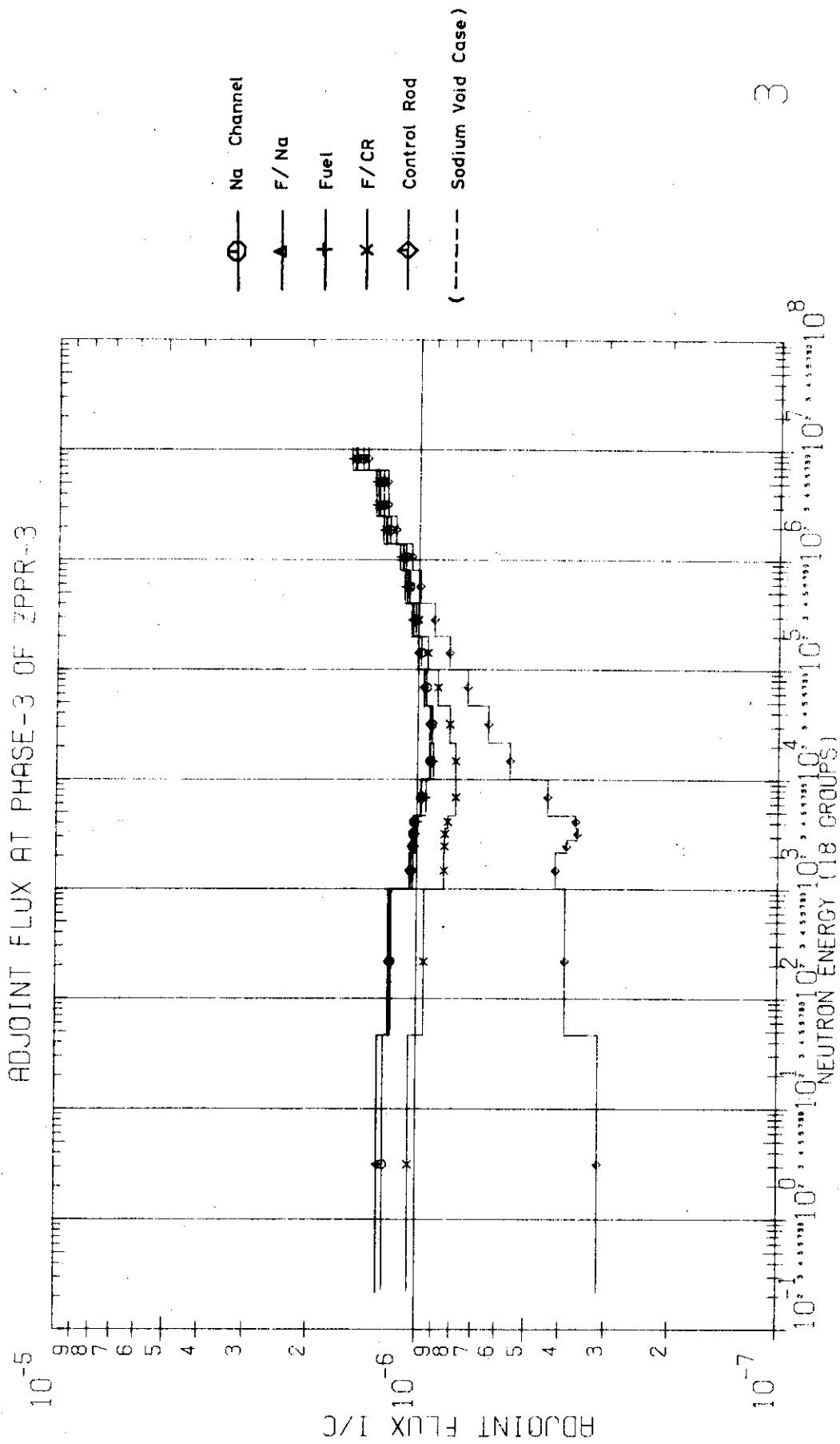


Fig. 4.3.12 Adjoint flux at inner core of ZPPR3, phase 3

1

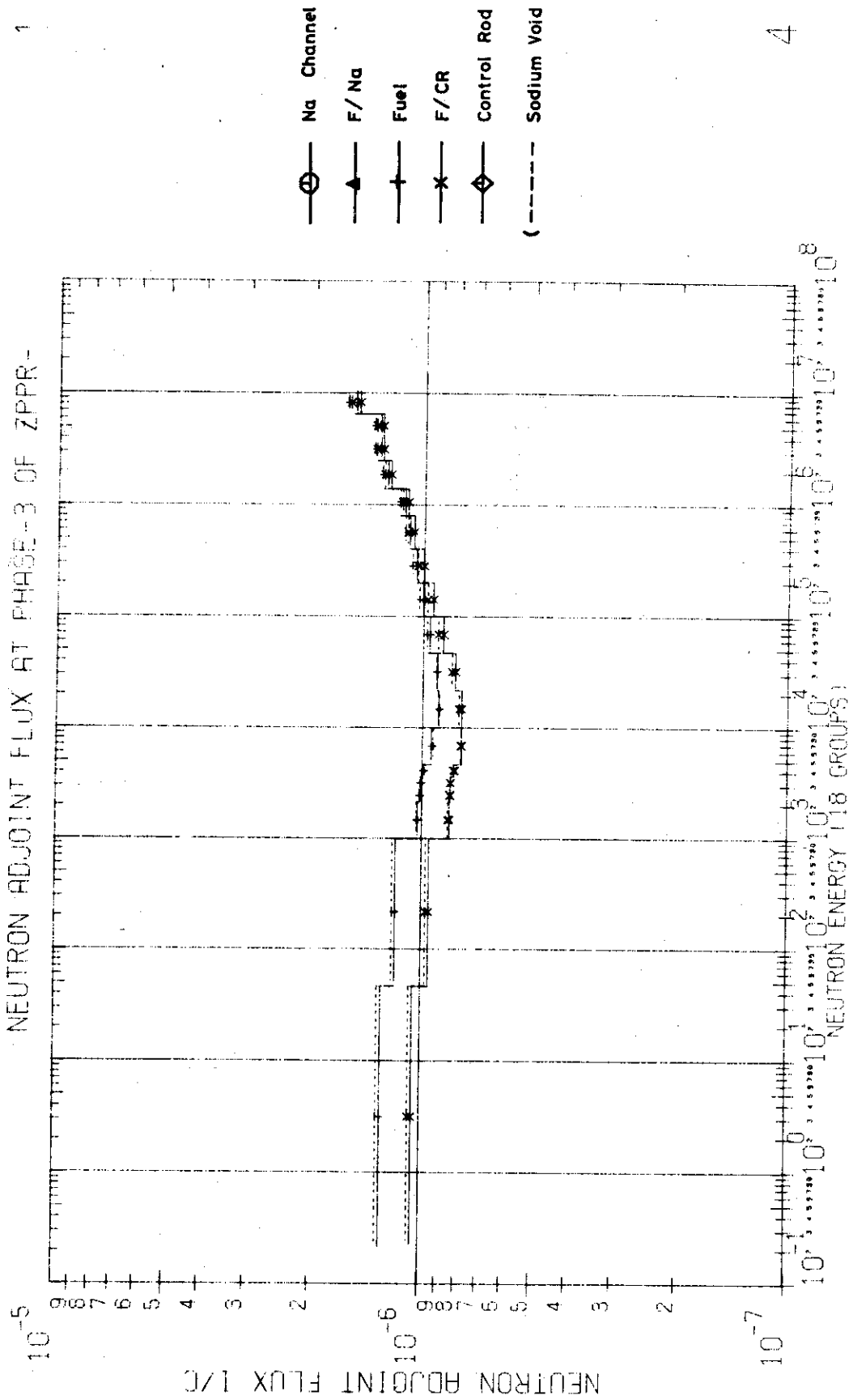
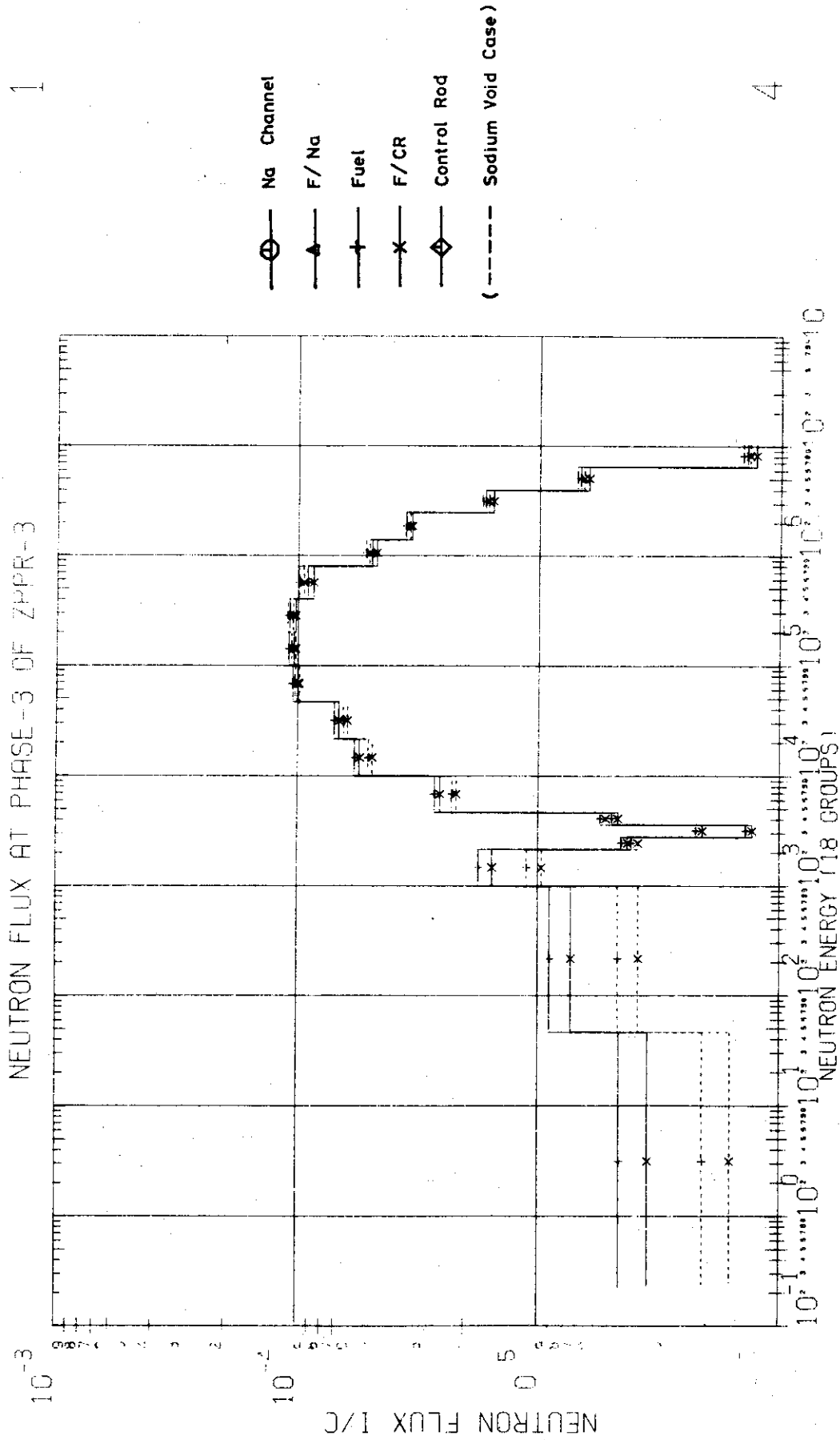


Fig.4.3.13 Adjoint flux at Fuel and F/CR in inner core of ZPPR3, phase 3

1



4

Fig. 4.3.14 Neutron flux of Fuel and F/CR in inner core of ZPPR 3, phase 3

4.4 Calculation of Sodium Void Worth Distribution in Proto-Type Fast Breeder Reactor

The proto-type fast breeder reactor in Japan, "MONJU"⁽¹⁴⁾ is a sodium cooled reactor fueled with plutonium oxide of pin type clad with stainless steel. The core is composed of two zones, inner and outer core with a height of 46.5 cm and equivalent radii of 59 cm and 89.4 cm, respectively. The cross sectional view of the core is shown in Fig.4.4.1.

A main concern in safety related problems is to predict precisely the reactivity change due to sodium loss. In this section, we intend to predict the sodium void worth distribution in the core and axial blanket regions, and also the maximum positive reactivity change.

In the present work, we treat only the core with initial loading composition. As discussed in Ref.(61), the sodium void worth of a power reactor varies to a more positive side as proceeding with the burn-up and as accumulating fission products.

4.4.1 Computational Method and Model

The group constant sets used are the JAERI Fast set version 1R and version 2. The detailed contents of these sets were explained in Ref.(51). Since the heterogeneity effect is not significant for a pin cell, the homogeneous model is adopted here. By using the effective cross sections for each region, one dimensional diffusion calculations have been performed and collapsed into eighteen groups from seventy groups for two dimensional calculations. The lower boundaries of groups are as follows; 6.5 MeV/4 MeV/2.5 MeV/1.4 MeV/800 keV/400 keV/200 keV/100 keV /46.5 keV/21.5 keV/10 keV/4.65 keV/3.6 keV/2.78 keV/2.15 keV/1 keV/ 46.5 eV/0.215 eV/.

The calculational model in rz geometry is shown in Fig.4.4.2. The hexagonal layers consisting of the hexagonal fuel assemblies are approximated by annular regions with the equivalent volumes and distances from the core center. Accordingly, the inner core consists of six fuel regions and the outer core two fuel regions. All the control rods are replaced by the sodium channels. The neutron source is replaced also by the sodium channel. They are circularized in the same manner as shown in Fig.4.4.2. The third layer of the inner core includes the sodium channel region internally.

The sodium void worths were calculated for the fuel regions but not for the sodium channels. To obtain the spacial distribution, each annular region is axially divided into three regions, 0 ~ 15.5 cm, 15.5 cm ~ 31.0 cm, 31.0 cm ~ 46.5 cm, in the core and into two regions, 46.5 cm ~ 62.75 cm, 62.75 cm ~ 79 cm, in the axial blanket. The maximum void worth is determined by taking summation of the positive worths.

The one dimensional diffusion calculations were performed by using SLAROM and the two-dimensional calculations by CITATION. The sodium void worths have been obtained by the first order perturbation routine in the CIPER code. For some regions the exact perturbation or direct criticality calculations have been also performed to compare the results with the first order perturbation. The radial and axial buckling values used for the one-dimensional calculations in slab or cylindrical geometry, are given in Table 4.4.1.

4.4.2 Void Worth Distribution and Maximum Worth

The results is presented in Table 4.4.2, where the upper value in each row is obtained by the JFS version 1R and the lower by the version 2.

The eigenvalue of the reference core is 1.0338 and 1.0264 by the versions 1R and 2, respectively.

The sodium void worth in the axial blanket is negative for all the regions. In the inner core, it is positive in the region, 0 ~ 31.0 cm and turns to negative in the region, 31.5 ~ 46.5 cm. In the outer core, the worth is negative except for the region, 0 ~ 15.5 cm, of the seventh region.

The specific worth (worth / kg-Na) is presented in Table 4.4.3 for each region. The characteristics of spatial distribution can be easily seen from the table. That is, the specific worth varies to negative side with approaching to the outer boundary and is almost constant in the axial blanket. There are large differences between the seventh and the eighth regions, because the radial gradient of the neutron flux varies rapidly in these regions and the leakage component is proportional to it. The specific worth is the most positive at the core center and the most negative at the region, 0 ~ 15.5 cm of the eighth region. Its radial dependence is shown in Fig.4.4.3 for the regions with total core height. The two sets give a similar shape to each other.

The cumulative void worths of the core, and the core plus axial blanket region are shown in Fig.4.4.4. The worth becomes more positive with increasing the radius and arrives at the maximum value around the boundary between the inner and outer core, and then decreases rapidly in the outer core. The figure reveals that the void worth slightly decreases around the sodium channels at the third and fifth regions. This may be due to the environment effect of the sodium channels.

The maximum positive void worth is presented in Table 4.4.4 together with each component obtained by the perturbation calculations. The corresponding void region is composed of the regions, 0 ~ 31.0 cm in the

inner core and 0 ~ 15.5 cm in the outer core. The direct criticality calculations by the version 2 gives 1.01 % $\Delta k/k$ (~ 3.4 dollars) which is in a good agreement with the first order perturbation calculation. It is interesting that the scattering term becomes dominant at the maximum void worth by the cancellation between the leakage and the absorption terms. When the whole core and axial blanket are voided, the version 1R gives a negative worth of -0.37 % $\Delta k/k$ and contrarily the version 2 a small positive value. As a result, it should be taken into account in the safety analysis that the positive reactivity of about 3.4 dollars will be inserted with the sodium loss.

4.4.3 Comparison between Results by Version 1R and 2

From Table 4.4.2 we can see that the results by the version 2 are more positive than those by the version 1R in all the regions. The differences are about 30 ~ 40 percents in the core and 20 percents in the axial blanket. Such quantities may be significant for an accurate prediction of the sodium void worth. As shown in Fig.4.4.4, the difference becomes larger with an increase of the void worth, and attains at the maximum around the boundary between the inner and outer cores. However, the shape of distribution and the zone giving the maximum worth are almost the same for either version.

In the following we examine the contents of difference. Each reactivity component is compared in Tables 4.4.5 ~ 4.4.8. As for the fission term, the version 2 gives more negative values by about ten percents than the version 1R as shown in Table 4.4.5. However, since their absolute values are small and their contribution to the total reactivity is minor, such a difference may not be significant. Here we note that the fission

term is larger in the outer core than in the inner core because an enrichment of plutonium is higher in the outer region.

The absorption terms by the version 2 given in Table 4.4.6, is more positive by about 10 ~ 15 percents than by the version 1R over the inner and outer cores, but in the axial blanket the difference between them is negligibly small.

Table 4.4.7 shows that there exists a significant difference in the scattering term. The version 2 gives more positive values by about 20 percents in the core and by about 10 percents in the axial blanket. Since its absolute value is large, it plays a dominant role in the total reactivity.

Table 4.4.8 shows that the version 2 results in a less negative leakage, but this difference is only a few percents. It should be noted that the leakage term varies rapidly with increasing the radius in the core and consequently moves the total reactivities to the negative side.

From the above discussion, we can conclude that the main reason why the version 2 gives more positive reactivities than the 1R, is firstly due to the difference in the scattering term and secondly due to that in the absorption term. Such a conclusion can be inferred from Fig.4.4.3, where the radial distribution of the total reactivity and the scattering term are compared between both the versions. It can be seen that the difference in the scattering terms is similar to that in the total worths throughout the whole core. Moreover, in order to examine the scattering term more in detail, its group-wise contributions are presented in Table 4.4.9, which shows the values for the region 0 ~ 15.5 cm at the core center. There exist large differences in groups 9, 10(100~21.5 keV), 12(10~4.65 keV) and 15, 16 groups (2.78~1 keV). Above 100 keV, the version 2 gives rather more negative

worths. Further, to decompose the reactivity change we present the neutron flux and the adjoint flux in Fig.4.4.5. It reveals that the neutron flux obtained by the version 2 is lower in the energy range 1 MeV ~ 50 keV and higher below 2 keV, that is, softer spectrum than that by the 1R. They agree well in the neighbourhood of sodium resonance at 2.85 keV. Hence, the neutron flux does not cause the large difference. On the other hand, the difference in the adjoint flux is important. It contributes to the reactivity change as a factor of $(\phi_{i+1}^* - \phi_i^*)$ in the scattering term, which is very sensitive to the change of the adjoint flux. Remembering that the change of macroscopic scattering cross sections accompanied by sodium loss was not so much different (within five percents) between the two sets, the difference in the factor $(\phi_{i+1}^* - \phi_i^*)$ dominantly causes that of the scattering term. The similar discussion can be applied to the case of the maximum void worth presented in Table 4.4.4. In this case, the difference in the scattering term is 0.15 % $\Delta k/k$ and that in the absorption term is 0.067 % $\Delta k/k$. The characteristic of the adjoint flux mentioned above is thought to arise from the revision of cross sections from the version 1R to the version 2 for ^{239}Pu , ^{238}U and light elements. Such a revision for ^{239}Pu and capture of ^{238}U affects mainly to the groups 15 and 16, and that for capture of ^{238}U and light elements does to the groups, 9 ~ 12.

Table 4.4.1 Group independent buckling values

 $(\times 10^{-4} \text{ cm}^{-2})$

Region	Axial buckling	Radial buckling
Central sodium channel		6.182
Inner core	6.30	6.211 (6.125)
Outer core		6.255 (6.156)
Axial blanket	6.80	
Radial blanket		6.211
Axial reflector	7.20	
Radial reflector		5.777

() Sodium voided case

Table 4.4.2 Comparison of sodium void reactivity worth distribution by
JAERI Fast set version 1R and version 2

($\times 10^{-6} \Delta k/k$)

Void region (cm)	1	2	3	4	5	6	7	8
	I/C	I/C	I/C	I/C	I/C	I/C	O/C	O/C
Axial blanket	- 15 - 11	- 27 - 20	- 31 - 24	- 53 - 41	- 44 - 34	- 68 - 58	- 63 - 54	- 45 - 39
Axial blanket	- 95 - 76	- 180 - 144	- 171 - 136	- 350 - 288	- 274 - 225	- 415 - 358	- 535 - 482	- 452 - 415
Core	-109 - 70	- 219 - 143	- 187 - 117	- 426 - 300	- 379 - 280	- 521 - 402	- 994 - 893	-1388 -1309
Core	183 246	332 454	309 420	534 739	332 494	396 593	- 266 - 96	-1714 -1581
Core	391 471	728 883	673 815	1223 1486	862 1069	1063 1318	237 458	-1919 -1749
Core total	465 647	841 1194	795 1118	1331 1925	815 1283	938 1509	-1023 - 531	-5021 -4639
Core total Direct V-1R				1315				-4056 (-4462)*

Upper : First order perturbation by JAERI set V-1R

Lower : First order perturbation by JAERI set V-2

* : Exact perturbation by V-1R

Table 4.4.3 Specific sodium void reactivity distribution
 ($\times 10^{-6} \Delta k/k/kg$)

Void region (cm)		1	2	3	4	5	6	7	8
		I/C	I/C	I/C	I/C	I/C	I/C	O/C	O/C
Axial blanket	62.75-79.0	- 2.0 - 1.5	- 1.8 - 1.3	- 2.0 - 1.6	- 1.7 - 1.4	- 1.6 - 1.2	- 1.7 - 1.4	- 1.2 - 1.0	- 0.74 - 0.64
Axial blanket	46.5 -62.75	-12.5 -10.0	-11.9 - 9.5	-11.3 - 9.0	-11.6 - 9.5	- 9.9 - 8.1	-10.0 - 8.9	-10.1 - 9.1	- 7.5 - 6.9
Core	31.0 -46.5	-15.1 - 9.7	-15.2 - 9.9	-13.0 - 8.1	-14.8 -10.4	-14.4 -10.6	-13.5 -10.4	-19.8 -17.8	-24.2 -22.8
Core	15.5 -31.0	25.4 34.1	23.0 31.5	21.4 29.1	18.5 25.6	12.6 18.7	10.3 15.4	- 5.3 - 1.9	-29.8 -27.5
Core	0.0 -15.5	54.2 65.3	50.5 61.2	46.7 56.5	42.4 51.5	32.7 40.5	27.6 34.3	4.7 9.1	-87.4 -80.7
Core total	0.0 -46.5	21.5 29.9	19.4 27.6	18.4 25.8	15.4 22.2	10.3 16.2	8.1 13.1	- 6.8 - 3.5	-29.1 -26.9

Upper : First order perturbation by JFS-V-1R

Lower : First order perturbation by JFS-V-2

Table 4.4.4 Maximum sodium void reactivity worth
by first order perturbation ($\% \Delta k/k$)

		V - 1R	V - 2
Maximum positive worth	Fission	-0.064	-0.072
	Absorption	0.390	0.457
	Scattering	0.794	0.943
	Leakage	-0.395	-0.384
	Total Direct calc.	+0.73	+0.94 +1.01
Core + axial blanket void worth	Fission	-0.125	-0.139
	Absorption	0.653	0.750
	Scattering	1.465	1.711
	Leakage	-2.360	-2.311
	Total Direct calc.	-0.37	+0.01 +0.20

Table 4.4.5 Fission term of sodium void reactivity worth by first order perturbation
 ($\times 10^{-6} \Delta k/k$)

Void region (cm)	1 I/C	2 I/C	3 I/C	4 I/C	5 I/C	6 I/C	7 O/C	8 O/C
Axial blanket	- 0.021 - 0.068	- 0.04 - 0.127	0.055 - 0.039	0.158 - 0.005	0.125 - 0.004	0.132 - 0.003	0.055 - 0.054	0.034 - 0.035
Axial blanket	- 0.016 - 0.083	- 0.029 - 0.155	0.211 0.04	0.546 0.208	0.436 0.169	0.487 0.207	0.288 0.127	0.183 0.069
Core	-12.7 -13.3	- 23.8 - 25.0	- 25.1 - 26.9	- 40.3 - 43.8	- 34.2 - 37.2	- 34.6 - 36.9	- 78.2 - 85.3	- 62.6 - 66.1
Core	-16.6 -18.0	- 31.3 - 33.9	- 33.0 - 36.6	- 52.9 - 60.0	- 45.3 - 51.5	- 47.6 - 52.4	-101. -115.	- 89.7 - 97.3
Core	-20.7 -22.5	- 38.9 - 42.5	- 40.8 - 45.7	- 66.2 - 75.7	- 56.8 - 65.1	- 60.3 - 66.8	-129. -148.	-116 -126
Core	-50.0 -53.8	- 94.0 -101.4	- 98.9 -109.2	-159. -180.	-136. -154.	-143. -156.	-308. -348.	-268. -289.

Upper : JFS-V1-R

Lower : JFS-V2

Table 4.4.6 Absorption term of sodium void reactivity worth by first order perturbation ($\times 10^{-6} \Delta k/k$)

Void region (cm)	1 I/C	2 I/C	3 I/C	4 I/C	5 I/C	6 I/C	7 O/C	8 O/C
Axial blanket	4.13 3.97	7.78 7.48	7.03 7.04	10.1 10.3	8.18 8.40	8.53 8.80	6.91 7.02	4.01 4.06
Axial blanket	25.2 25.6	47.9 48.6	42.0 44.4	66.9 72.3	54.3 58.9	60.2 65.7	55.5 59.8	34.4 36.8
Core	64.7 73.5	123. 140.	128. 134.	205. 234.	166. 191.	188. 216.	210. 235.	146. 159.
Core	110. 128.	210. 245.	201. 234.	353. 413.	288. 338.	331. 388.	356. 410.	255. 285.
Core	143. 167.	272. 318.	260. 305.	460. 540.	376. 442.	433. 511.	467. 541.	337. 378.
Core	318. 369.	605. 703.	589. 673.	1018. 1187.	830. 971.	952. 1115.	1033. 1186.	738. 822.

Upper : JFS-VI-R

Lower : JFS-V2

Table 4.4.7 Scattering term of sodium void reactivity worth by first order perturbation ($\times 10^{-6} \Delta k/k$)

Void region (cm)	1 I/C	2 I/C	3 I/C	4 I/C	5 I/C	6 I/C	7 O/C	8 O/C
Axial blanket 62.75-79.0	24.8 26.3	47.3 50.3	43.2 46.4	75.1 79.9	59.5 63.4	64.9 69.0	57.5 60.4	36.0 37.5
Axial blanket 46.5 -62.75	92.6 105.	177. 200.	158. 180.	294. 332.	231. 261.	263. 296.	255. 284.	174. 192.
Core 31.0 -46.5	143. 168.	274. 322.	250. 295.	467. 547.	368. 430.	417. 490.	410. 471.	323. 368.
Core 15.5 -31.0	226. 270.	434. 518.	392. 469.	750. 891.	586. 694.	671. 799.	681. 785.	569. 651.
Core 0.0 -15.5	293. 350.	563. 674.	506. 608.	979. 1165.	764. 906.	878. 1049.	898. 1038.	759. 870.
Core 0.0 -46.5	662. 788.	1271. 1514.	1148. 1372.	2196. 2603.	1718. 2030.	1966. 2338.	1989. 2294.	1651. 1889.

Upper : JFS-VI-R

Lower : JFS-V2

Table 4.4.8 Leakage term of sodium void reactivity worth by first order perturbation ($\times 10^{-6} \Delta k/k$)

Void region (cm)	1 I/C	2 I/C	3 I/C	4 I/C	5 I/C	6 I/C	7 O/C	8 O/C
Axial blanket 62.79-79.0	- 43.5 - 41.3	- 81.8 - 77.5	- 81.7 - 77.6	- 139. - 132.	- 112. - 106.	- 142. - 135.	- 128. - 122.	- 84.5 - 80.4
Axial blanket 46.5 -62.75	-213 -206	-405. -393.	-371. -360.	- 712. - 692.	- 560. - 545.	- 739. - 721.	- 845. - 826.	- 661. - 644.
Core 31.0 -46.5	-304. -298.	-592. -580.	-530. -519.	-1058. -1038.	- 879. - 862.	-1091. -1072.	-1537. -1513.	-1794. -1770.
Core 15.5 -31.0	-137. -134.	-281. -275.	-252. -246.	- 517. - 505.	- 497. - 486.	- 557. - 541.	-1201. -1176.	-2448. -2420.
Core 0.0 -15.5	- 23.8 - 23.6	- 68.5 - 66.9	- 53.2 - 52.0	- 150. - 143.	- 221. - 214.	- 188. - 175.	- 999. - 973.	-2899. -2871.
Core 0.0 -46.5	-465. -456.	-942. -922.	-835. -817.	-1725. -1686.	-1597. -1562.	-1836. -1788.	-3737. -3662.	-7141. -7061.

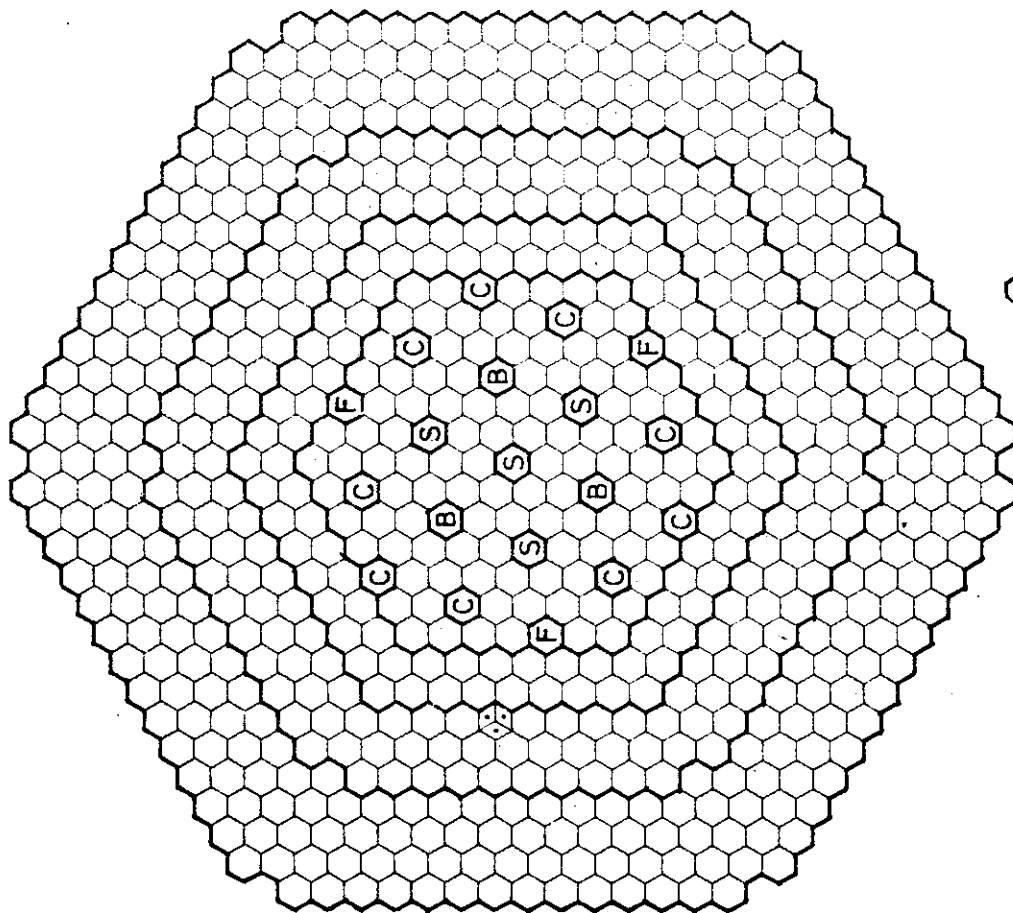
Upper : JFS-V1-R



Lower : JFS-V2




Table 4.4.9 Comparison between group-wise contributions of scattering terms by JFS-V2 and 1R ($\times 10^{-6} \Delta k/k$)

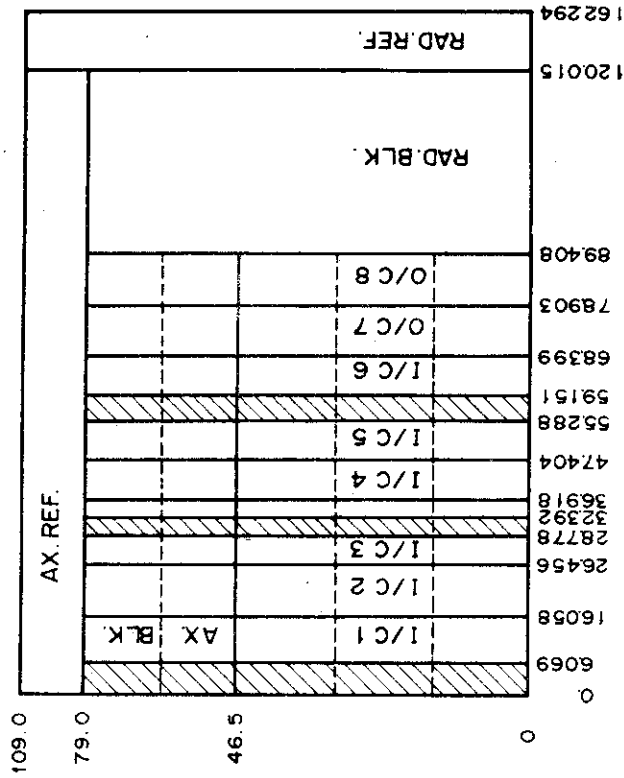
Group	JFS-1R	JFS-V2	Difference (V2) - (1R)
1	4.4	5.0	0.6
2	10.9	10.3	- 0.6
3	44.4	41.1	- 3.3
4	78.2	76.4	- 1.8
5	51.0	46.1	- 4.9
6	85.4	83.3	- 2.1
7	75.1	76.2	1.1
8	62.5	61.2	- 1.3
9	69.7	86.1	16.4
10	- 2.3	15.3	13.0
11	-12.2	-16.2	- 4.0
12	-46.7	-33.5	13.2
13	-23.0	-19.7	3.3
14	-13.4	-10.3	3.1
15	-42.2	-32.5	9.7
16	-45.4	-30.2	15.2
17	- 8.1	- 8.2	- 0.1
18	0.0	0.0	0.0
Total	292.7	350.4	57.7

Calculated by first order perturbation for
0.0 - 15.5 cm of the first region in the
inner core.



-  Safety Rod
-  Back up Rod

-  Coarse Rod
-  Fine Rod
-  Neutron Source




 No Follower

Fig.4.4.2 Calculation model of proto-type fast breeder reactor

Fig.4.4.1 Cross sectional view of proto-type fast breeder reactor

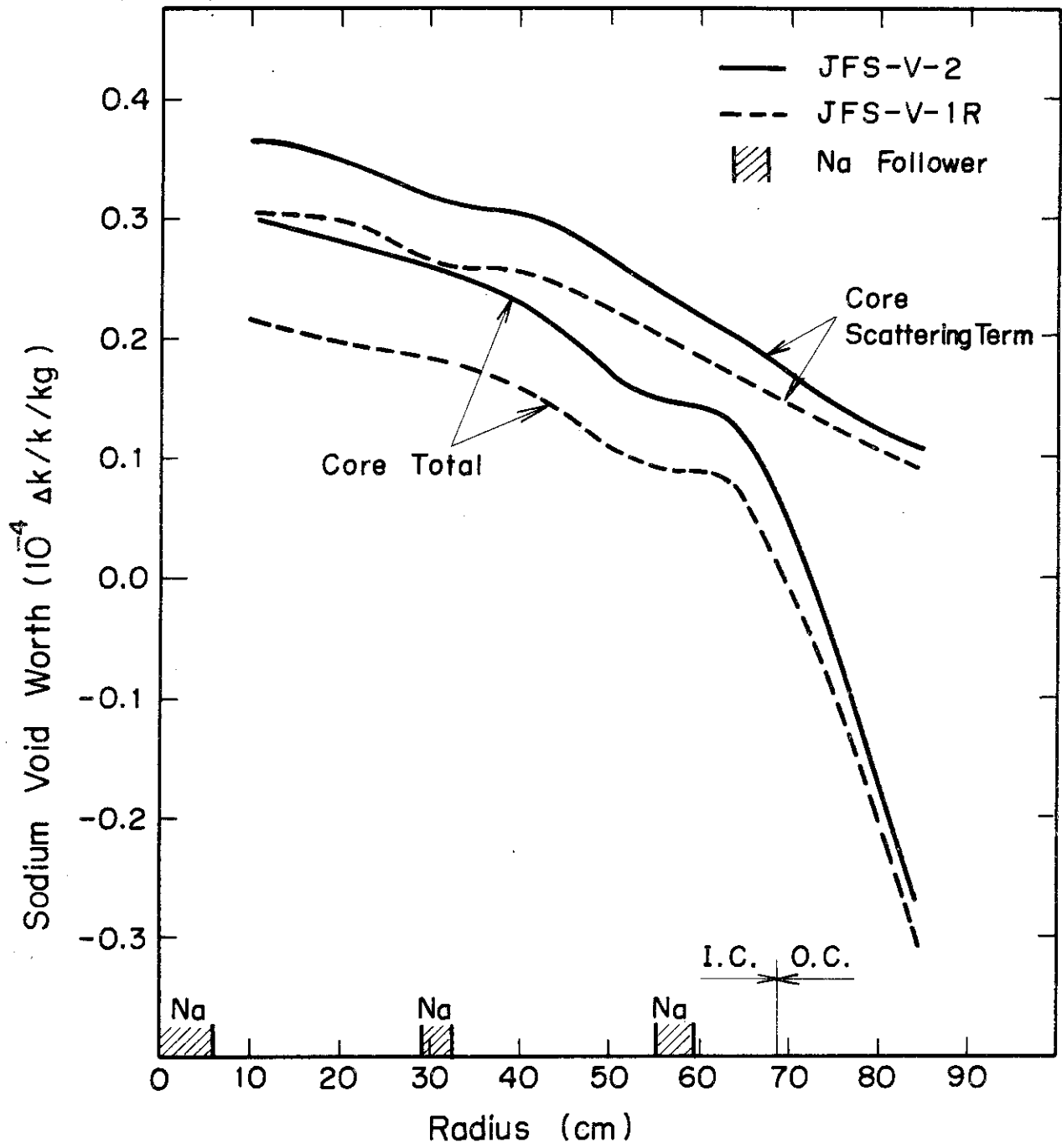


Fig.4.4.3 Spatial dependence of specific sodium void reactivity

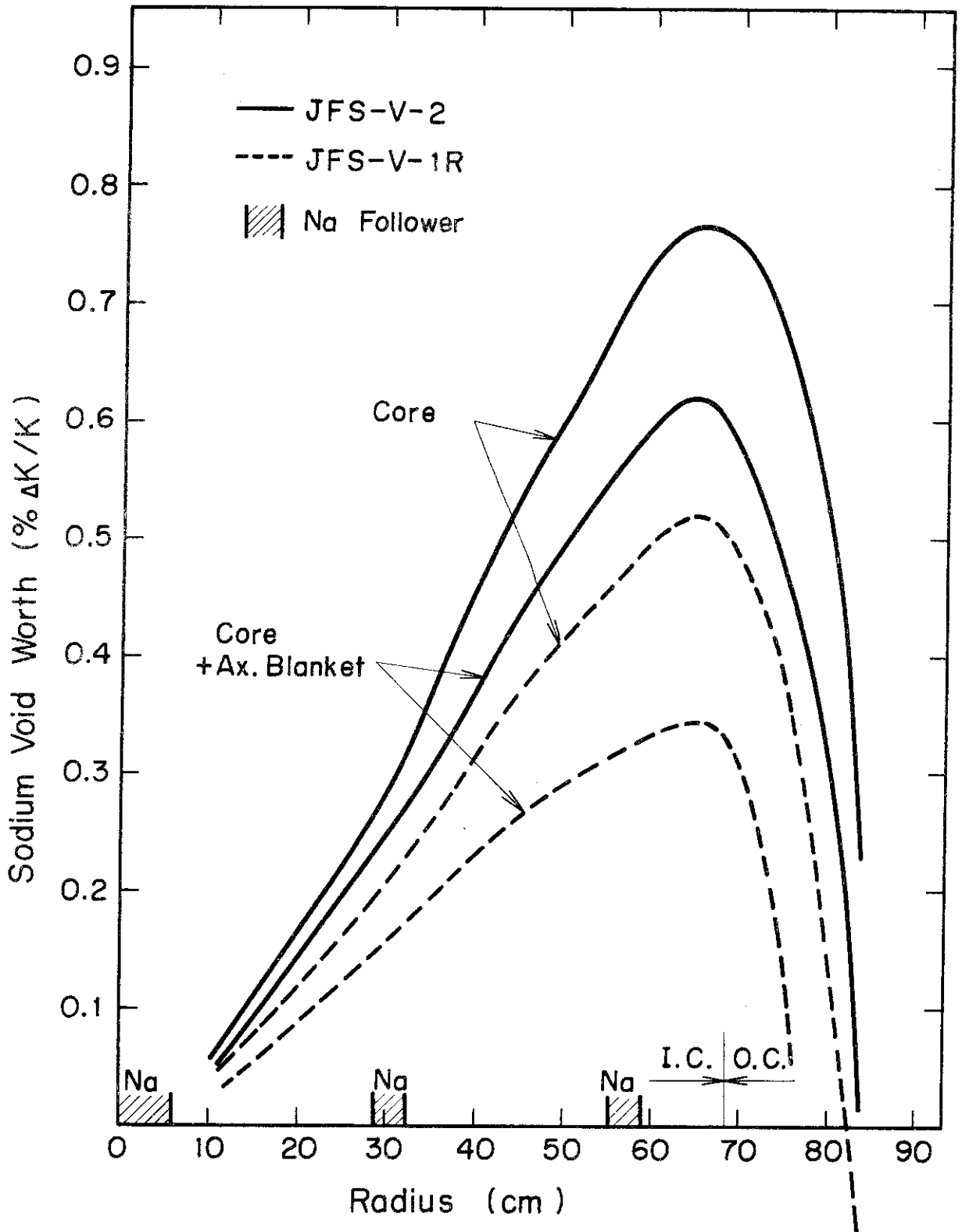


Fig.4.4.4 Cumulative net sodium void reactivity

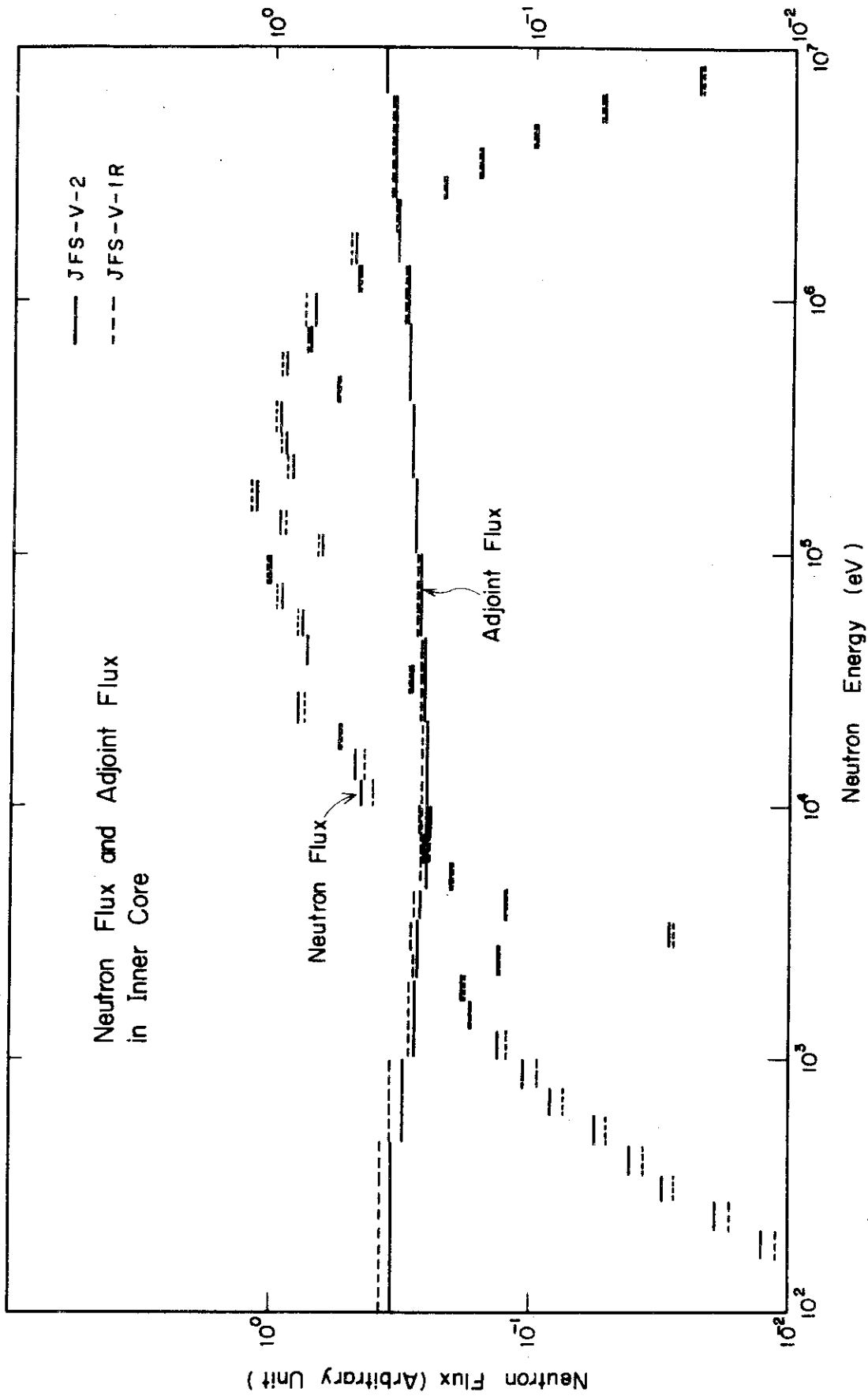


Fig.4.4.5 Comparison of real and adjoint flux between JFS-1R and JFS-V2

5. Analysis with Use of Multi-Group Cross Sections Produced by ESELEM 5

5.1 Cross Section Preparation

The sodium void worths were calculated for MZA and ZPPR assembly 2 by using ESELEM 5 described in Chapter 3. In order to keep the consistency with the calculations made by using the broad group constants set (broad group method), the similar models and methods were carefully employed in the present calculations. The main difference of the methods exists essentially in the production method of cell averaged cross sections. In the fine group method, a fundamental mode neutron spectrum is calculated at first for a heterogeneous cell or a homogeneous medium. The fine group width is 0.0084 in lethargy (2100 groups for 10.5 MeV \sim 0.25 eV). The cross sections of each region are averaged over the cell and collapsed to the broad group structure. In the present calculation, the number of broad groups is 70 and they are collapsed further to 18 groups by one-dimensional diffusion calculations in the same manner as in the broad group method. Therefore, a discrepancy observed between the results obtained by these methods will certainly arise from the difference of the production method of cell averaged cross sections. Hence, this comparison is helpful to assess the capability to predict the sodium void reactivity.

The heterogeneous cell calculations have been made in the normal and voided states by using the buckling values which give $k_{\text{eff}} = 1.0$ in the broad group method, and by using the fission source distribution obtained in the SLAROM calculation as the initial guess. When this guess is used, the source distribution sufficiently converges usually after one outer iteration. The heterogeneity effect on the resonance self-shielding was taken into account on the basis of the rational approximation in

both the methods. The anisotropy of elastic scattering is considered up to the P_1 order of the Legendre coefficients for oxygen and sodium.

The transport cross section is defined by the P_1 weighting as follows;

$$\sigma_{tr,K}^i = \frac{\sum_{j \in K} \frac{\sigma_{tr,j}^i \phi_j}{\Sigma_{tr,j}} \Delta E}{\sum_{j \in K} \frac{\phi_j}{\Sigma_{tr,j}} \Delta E},$$

$$\phi_j = \int_{\text{cell}} \phi_j^\ell dV, \quad \Sigma_{tr,j} = \frac{\sum_i \int_{\text{cell}} N_\ell^i \sigma_{tr,\ell}^i \phi_j^\ell dV}{\phi_j}$$

where j stands for fine group, K broad group, i nuclide and ℓ cell region.

In the ESELEM 5 code, the isotropic diffusion coefficient is calculated, so the neutron streaming effect is assumed to be the same as in the broad group calculations given in Chapter 4.

The fundamental mode spectra are presented in Fig.5.1 for the normal and the voided cells in the inner core of ZPPR-2. The spectrum hardening is found for the voided cell, that is, the flux increases above ~100 keV and decreases below it.

5.2 Intercomparison Calculation for MZA

The fine group method gives $k_{\text{eff}} = 1.0062$ which agrees very well with the measured value as shown in Table 4.2.1. The results of the sodium void worths are compared with the measurements in Table 5.1. The corrected and uncorrected values for the streaming effect are presented and all the measured values lie between these values. The calculations can predict the measurements with a high confidence though the uncertainty is included in the estimation of the streaming

effect. Especially, the agreement is excellent at the core center. The corrected values are slightly more positive than the measurements for the regions, C, D and A&D. The components obtained by EP calculations are intercompared in Table 5.2 between the fine and the broad group methods. It reveals that the fine group method gives consistently larger scattering components by 15 percents and smaller leakage components by 6 ~ 8 percents than the broad group method. As a result, these components cause more positive worths by about ten percents at the core center for the fine group method. Such a discrepancy is not serious under the present status of the uncertainty in cross sections and calculation methods. Therefore, the reliability of the broad group method is supported by the detailed method and the results can easily be corrected for the fine spectrum effect by using these consistent bias factors.

5.3 Intercomparison Calculation for ZPPR-2

The fine group method gives the criticality $k_{\text{eff}} = 1.0010$ for ZPPR-2 and the broad group method does 0.9979, and the difference between these methods is within the target accuracy of 0.5 %. The calculated sodium void worths are shown in Table 5.3 where the results are expressed in terms of void worth, C/E and deviation of specific worth. The calculations overpredict considerably the values to the positive side for all the voided regions. The C/E values are 1.40 ± 0.07 for the 9 ~ 93 drawers voided for ± 30.5 cm except for the 9 drawers case as mentioned in Chapter 4.3. The (C-E)/kg values are about $0.140 \times 10^{-4} \Delta k/k$ for these cases. Hence, the fine group method results in a larger discrepancy with the measurements than the broad group method. To compare the calculational results, the perturbation components are presented in

Table 5.4. We can see from the table that the scattering component by the fine group method is 12 percents larger and the leakage component is 6 ~ 8 percents smaller than the broad group method. These discrepancies are consistent with the conclusions obtained previously for MZA.

Though the difference between the fine and the broad group methods is consistent between MZA and ZPPR-2, the results by the former method show a better agreement with the measurements than those by the latter method for MZA but, on the contrary for ZPPR-2, the broad group method gives a better agreement than the fine group method. Here, we investigate other neutronics parameters in order to check an adequacy of the fine group method and the cross sections. The selected parameters are the sample worth distribution of sodium, the small sample worth at the core center and the neutron spectrum. The results are discussed below.

(1) Sample Worth Distribution of Sodium

The sample worth distribution of sodium was calculated for the model used in Chapter 4.3. The results are presented in Fig.5.2

(a) ~ (d) where the dotted line shows the fine group values and the real line does the broad group ones. We can see from the figure that:

(a) The fine group method gives more negative values by 10 ~ 15 percents than the broad group method at the core center. Such a discrepancy is consistent with the results for the large scale sodium void worths.

(b) The discrepancy tends to decrease with approaching to the outer region and is hardly found in the region beyond $r = 80$ cm, where the leakage component is dominant. (c) At the axial blanket, the measurements and the calculations agree very well (see Fig.5.2 (c)). (d) The axial traverse shows the same tendency as the radial one. Therefore, it can be concluded that the main source of discrepancy between two

calculations arises from the non-leakage components. This conclusion is consistent with that drawn for the large scale void worths.

(2) Central Sample Worth

The reactivity worths of a number of fissile, fertile, absorptive and scattering materials were measured at the center of the normal plate core and in the 93 drawers voided zone. These were made at the reactor midplane ($z = 0$) in the slot environment. The calculations were made for ^{239}Pu , ^{235}U , ^{238}U , carbon and sodium, and compared in Table 5.5 with the measured values which were corrected for the sample size. As for central reactivity worths, systematic discrepancies⁽⁶²⁾ have been found between the calculations and the measurements for ZPR and ZPPR assemblies. Therefore, to exclude the uncertainty in the measurements, the normalized values to the worth of ^{239}Pu are also presented in the table. The calculations give smaller relative sample worths for ^{235}U and ^{238}U by about ten percents than the measurements. On the other hand, the C/E values of carbon and sodium are considerably greater than unity in the reference core. From the point of view of the sodium void worth, the most interesting information lies in the change in the C/E values between the normal(N) and voided(V) states, because this relates directly to the situation of sodium voiding. The last column of Table 5.5 presents the ratio R defined as $(C^N/E^N)/(C^V/E^V)$. The R values for ^{239}Pu , ^{235}U and ^{238}U do not so much deviate from unity because they are insensitive to the spectrum hardening due to the sodium loss. However, as for ^{238}U the fission reaction is affected to some extent due to the threshold at 1 MeV, so the contribution from fission for ^{238}U increases by about 8 percents in the voided state but that for ^{239}Pu does by only 3 percents. The fact that the deviations of the R values from unity are in different directions

between ^{238}U , ^{239}Pu and ^{235}U may indicate that the fission cross section of ^{238}U should be re-evaluated. On the other hand, the R values for the scatterers, carbon and sodium, considerably deviate from unity. The result for carbon is in consistent but that for sodium has a probable error as seen from the fact that the deviation from unity is about two standard deviations. Since the worths of scatterers are sensitive to the adjoint spectrum, the calculations would have predicted an over-hardening spectrum for ZPPR-2

(3) Neutron Spectrum at Core Center

The calculated neutron spectrum was compared with the measured values at the core center for the normal state. The measurement extended over an energy range of about 2 MeV to 1 keV, which covers 93 ~ 95 percents of the total flux. Figure 5.3 presents the bunched neutron spectrum by the measurements and the calculations with use of the fine and the broad group methods. The experimental data have been averaged over 0.5 lethargy width and the calculated values are obtained in the 18 group structure with the rz model. The sum of the fluxes is normalized to 100. Both of the calculations agree fairly well with the measurements throughout the energy range. At the 2.85 keV sodium resonance, the figure indicates a slight discrepancy among them. Especially, the broad group method gives a too high value below this energy. This is caused by inadequate resonance shielding factors given in the broad group constant set. It is difficult to conclude about the source of discrepancies in the sodium void worth between the calculations and the measurements from the comparison of the neutron spectra.

The detailed analysis has been performed by Beck et. al for ZPPR2 assembly with use of MC²-2 and SDX code system. The C/E values are 1.39 for 93 drawers void and 1.36 for Na sample worth in normal core, which are similar results obtained by ESELEM5.

Table 5.1 Comparison of sodium void worth in MZA between measurement and fine group calculation

Voided region	($10^{-4} \Delta k/k$)				
	A 0 ~ 15	B 15 ~ 30	C 30 ~ 45	D 45 ~ 80	A ~ D 0 ~ 80
Experiment	3.41±.22	0.55±.20	-3.05±.17	-3.22±.16	-1.80±.43
Calculation					
EP ^a	3.43	0.51	-3.50	-3.25	-3.18
(C/E) ^a	1.01±.06	0.92±.36	1.15±.06	1.01±.05	1.77±.24
EP with streaming ^b	3.46	0.78	-2.69	-2.71	-1.46
(C/E) ^b	1.01±.06	1.41±.36	.88±.06	.84±.05	.81±.24

a Uncorrected for neutron streaming effect

b Corrected for neutron streaming effect presented in Table 4.2.2

Table 5.2 Component of exact perturbation in MZA calculated by broad and fine group method

Voided region (cm)	$(\times 10^{-4} \Delta k/k)$				
	A 0 ~ 15	B 15 ~ 30	C 30 ~ 45	D 45 ~ 80	E 0 ~ 80
Component					
Fission + absorption	0.31 0.0	0.246 -0.001	0.186 0.059	0.221 0.20	0.93 0.22
Scattering	3.44 (0.85) 4.08	2.57 (0.85) 3.04	1.44 (0.86) 1.67	1.10 (0.96) 1.14	8.65 (0.86) 10.04
Leakage	-0.688(1.06) -0.650	-2.72 (1.08) -2.52	-5.63 (1.08) -5.23	-4.87 (1.06) -4.59	-14.40 (1.07) -13.94
Total	3.06 3.43	0.097 0.509	-4.01 -3.50	-3.54 -3.25	- 4.82 - 3.18

Upper : by broad group method

Lower : by fine group method

() : ratio of broad/fine

Table 5.3 Comparison of sodium void worth in ZPPR-2 between measurement and fine group calculation

Number of drawer	Axial length	$(\cdot 10^{-4} \Delta k/k)$			
		Experiment, E	Calculation, C	C/E	(C-E)/kg
1	0 ~ 15	0.0735±.0008	0.102	1.39	0.169
	±30.5	0.247 ±.08	0.293	1.18	0.070
4	±30.5	0.896 ±.08	1.19	1.33	0.111
	±45.8	0.532 ±.08	0.906	1.70	0.094
9	±15.3	1.44 ±.08	1.87	1.30	0.145
	±30.5	1.67 ±.08	2.71	1.62	0.175
21	±30.5	4.47 ±.08	6.36	1.42	0.136
45	±30.5	9.37 ±.08	13.7	1.46	0.146
69	±30.5	14.5 ±.08	20.9	1.44	0.140
93	±30.5	19.5 ±.08	27.9	1.43	0.137

Table 5.4 Component of sodium void worth in ZPPR-2 calculated by broad and fine group exact perturbation method

$(10^{-4} \Delta k/k)$				
Number of drawers Axial length	Fission + absorption	Scattering	Leakage	Total
1	0.025	0.170(0.87)	-0.0125(1.08)	0.182
±15 cm	0.023	0.194	-0.0116	0.206
1	0.044	0.300(0.88)	-0.091 (1.09)	0.254
±30 cm	0.042	0.343	-0.083	0.302
4	0.169	1.22 (0.88)	-0.361 (1.08)	1.03
±30 cm	0.173	1.39	-0.334	1.23
4	0.217	1.54 (0.88)	-1.05 (1.08)	0.711
±45 cm	0.221	1.75	-0.968	1.01
9	0.207	1.56 (0.88)	-0.113 (1.04)	1.65
±15 cm	0.216	1.78	-0.108	1.89
9	0.367	2.77 (0.88)	-0.807 (1.08)	2.33
±30 cm	0.383	3.15	-0.748	2.79
21	0.813	6.51 (0.89)	-1.88 (1.06)	5.45
±30 cm	0.966	7.35	-1.77	6.54
45	1.64	14.1 (0.88)	-4.00 (1.06)	11.7
±30 cm	1.93	15.9	-3.78	14.1
69	2.41	21.6 (0.88)	-6.11 (1.06)	17.9
±30 cm	2.84	24.4	-5.78	21.5
93	3.17	29.3 (0.90)	-8.67 (1.11)	23.8
±30 cm	3.73	32.7	-7.78	23.7

Upper : by broad group method

Lower : by fine group method

() : ratio of broad/fine

Table 5.5 Central reactivity worth in reference and voided core of ZPPR-2

	Experiment, E ^N		Calculation, C ^N		Experiment, E ^V		Calculation, C ^V		R = $\frac{C^N/E^N}{C^V/E^V}$
	Ih/kg	Relative to ²³⁹ Pu	Ih/kg	Relative to ²³⁹ Pu	Ih/kg	Relative to ²³⁹ Pu	Ih/kg	Relative to ²³⁹ Pu	
²³⁹ Pu	118.2 ± 0.54	1.0	139.8 (1.18)	1.0	113.98 ± 0.55	1.0	137.1 (1.20)	1.0	0.98 ± 0.007
²³⁵ U	95.26 ± 0.29	0.806	101.6 (1.07)	0.727 (0.90)	87.49 ± 0.28	0.768	96.48 (1.10)	0.704 (0.92)	0.97 ± 0.005
²³⁸ U	- 7.06 ± 0.08	-0.0597	- 7.82 (1.11)	-0.0559 (0.94)	- 6.46 ± 0.13	-0.0567	- 6.94 (1.07)	-0.0506 (0.89)	1.04 ± 0.026
C	- 10.88 ± 0.65	-0.0921	- 16.8 (1.55)	-0.120 (1.31)	- 18.50 ± 0.70	-0.162	- 20.8 (1.12)	-0.152 (0.94)	1.38 ± 0.074
Na	- 4.59 ± 0.12	-0.0388	- 6.59 (1.44)	-0.0472 (1.22)	- 5.60 ± 0.31	-0.491	- 7.30 (1.30)	-0.0532 (1.08)	1.11 ± 0.061

N : reference core

V : 93 drawers voided core

(): C/E

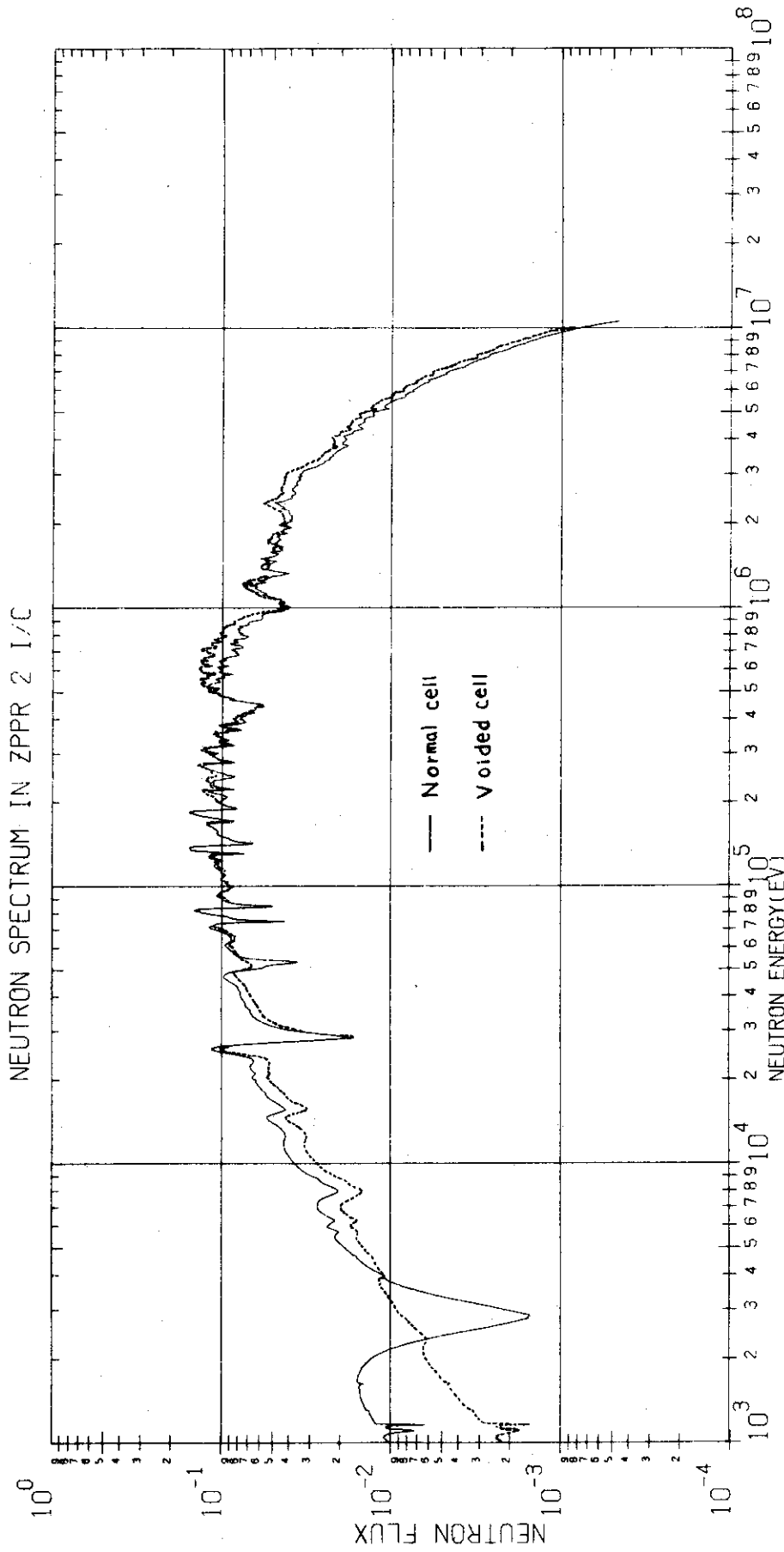
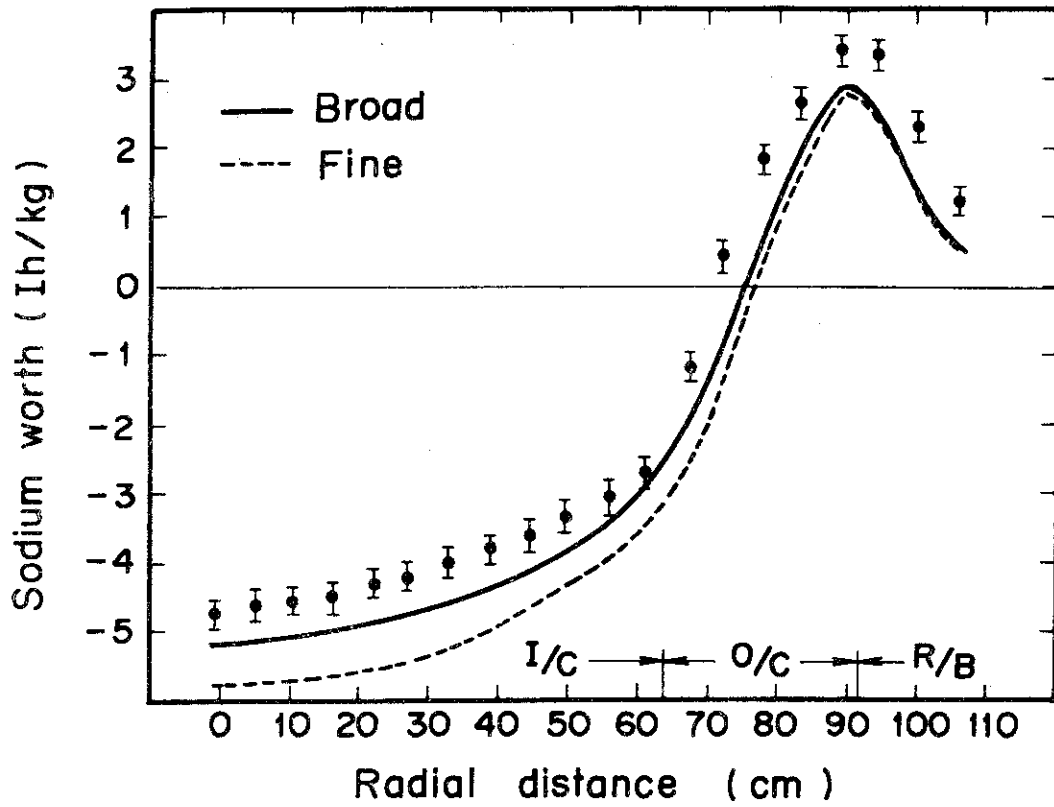
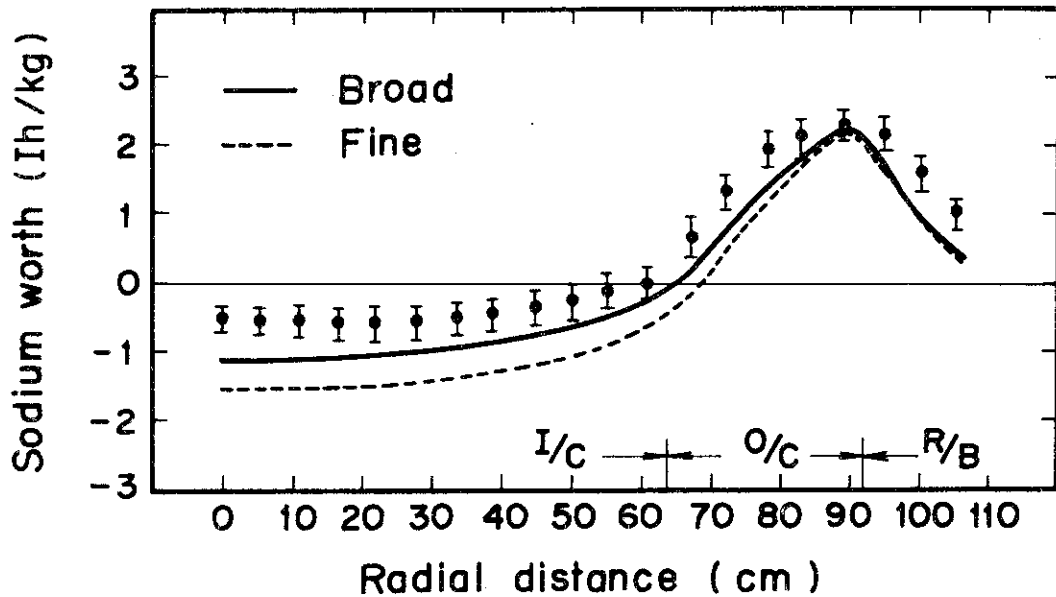


Fig.5.1 Fundamental mode neutron spectrum for normal and voided cell in inner core of ZPPR 2



(a) $Z = 7.711$ cm



(b) $Z = 28.031$ cm

Fig.5.2 Comparison of sample worth distribution of sodium in ZPPR 2

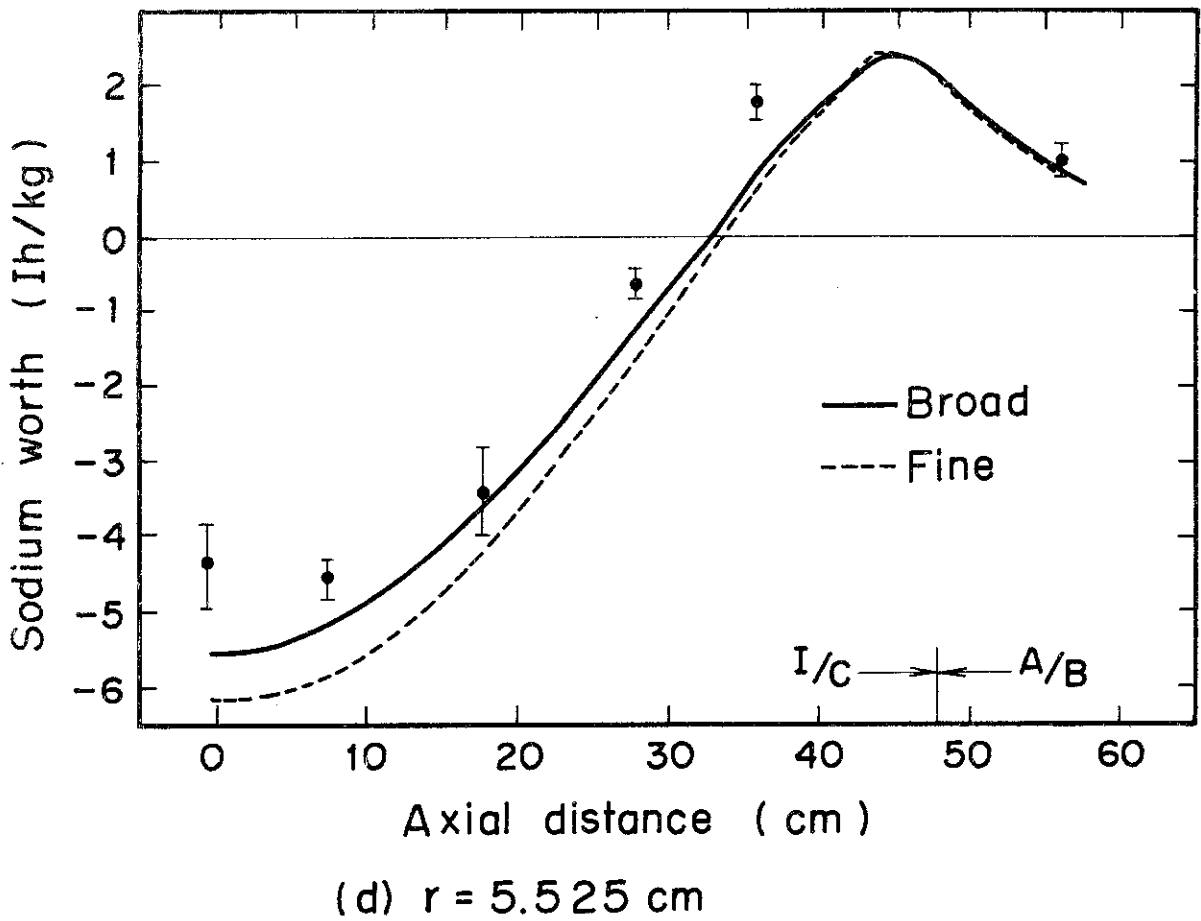
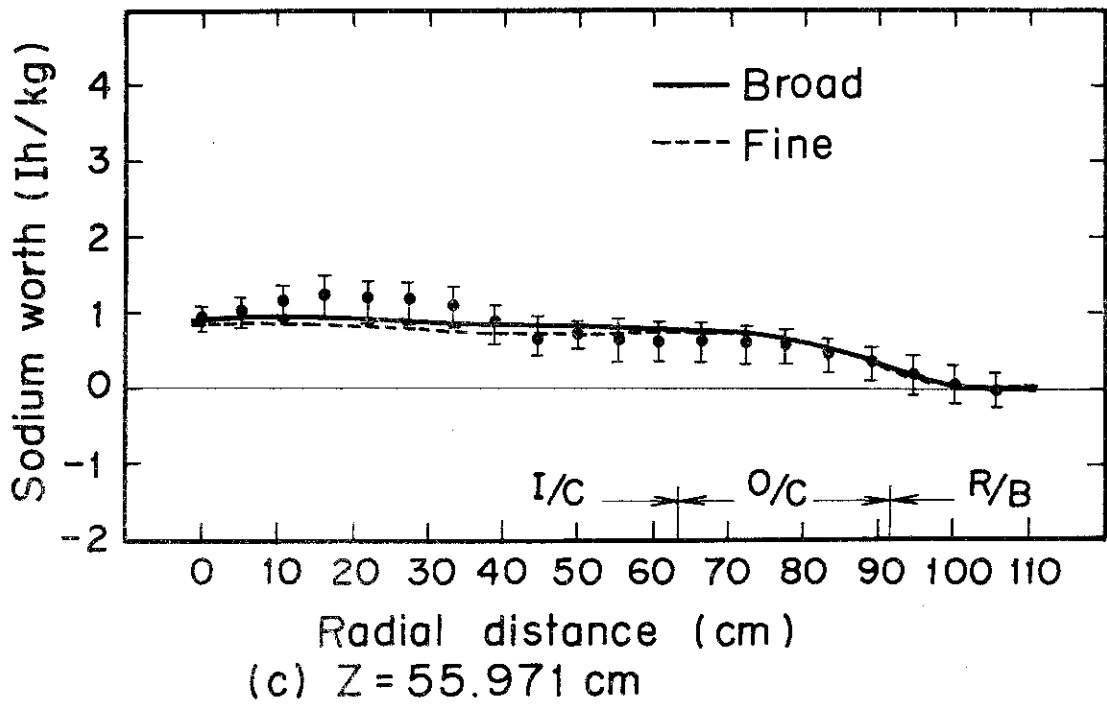


Fig.5.2 (continued)

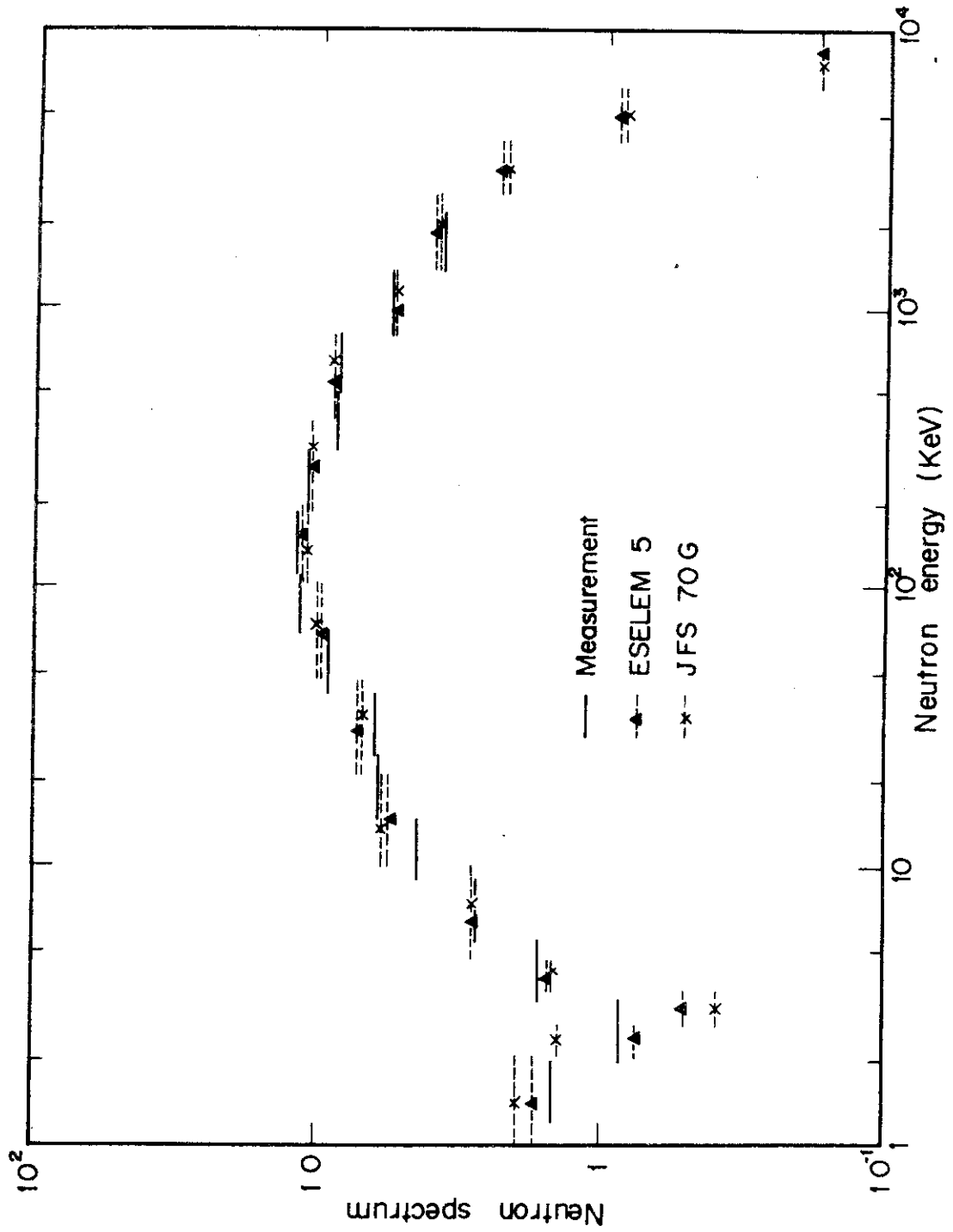


Fig.5.3 Comparison of neutron spectrum at core center of ZPPR 2

6. Improvement of Elastic Removal Cross Sections in Broad Group Constant Set

6.1 Introduction

The multi-group constants sets^{(9), (41)} have usually been used in the analysis of fast reactors. This approach has many advantages over a detailed spectrum method because of their computational economy, simplicity and existence of utility codes. There still exist, however, some inadequacies in the constants sets. One is concerned with the treatment of the elastic removal cross sections of light and medium nuclides, as pointed out in many studies.^{(23), (24)} The main reason of errors arises from using the self-shielding factor of elastic scattering cross section for that of removal cross section. This inadequacy brings an inaccuracy in the calculation of the neutron flux and reactivities due to Doppler coefficient and sodium-void worth as mentioned in Chapter 5. Hitherto, the efforts improving the elastic removal cross sections were mainly devoted to develop accurate or approximate methods in order to obtain the detailed spectrum for an individual composition as discussed in Chapter 3. Such methods will be more accurate than the group constant method, but require some additional calculations for every compositions to obtain the elastic removal cross sections. It can be said that these methods intend directly to obtain the exact or the almost exact values in order to overcome the shortcomings of conventional sets even if consuming a large computation time.

On the other hand in this chapter we intend to improve the accuracy of the elastic removal cross sections without changing the conventional concept of the group constants sets and to show that the practical improvement has been attained. Therefore the composition dependency is to be characterized by a single parameter, that is, the so-called admixture cross section, σ_o , as defined in the ABBN set.⁽⁴¹⁾

The effective elastic removal cross section was defined, in the ABBN set as

$$\langle \sigma_{er} \rangle = \frac{\langle \sigma_s \rangle \xi}{\Delta U} b, \quad (6.1)$$

where ΔU is a group width, ξ is the mean lethargy increment per collision, and b is a correction factor for spectrum, which is usually assumed to be unity based on $1/E$ spectrum. The quantity, $\langle \sigma_s \rangle$ is the effective elastic scattering cross section which is calculated from the infinitely dilute scattering cross section times the self-shielding factor, that is $\bar{\sigma}_s^\infty \cdot f_s$. This definition can not take into account the dependence of the effective cross section on the location of resonances within the group.

On the other hand, the JAERI Fast set used a little more precise definition:

$$\langle \sigma_{er,g} \rangle = \bar{\sigma}_{er,g}^\infty \cdot f_{s,g},$$

$$\bar{\sigma}_{er,g}^\infty = \frac{\int_{E_g}^{E_g/\alpha} dE' \frac{1}{E'} \int_{\alpha E'}^{E_g} \sigma_s(E' \rightarrow E) dE}{\int_{E_g}^{E_g/\alpha} \frac{1}{E} dE} = \frac{\int_{u_g}^{u_g} du' \int_{u_g}^{u'+\eta} \sigma_s(u' \rightarrow u) du}{\Delta U} \quad (6.2)$$

with

$$\alpha = \frac{(A - 1)^2}{(A + 1)^2}$$

and

$$\eta = \ln 1/\alpha \quad ,$$

$$f_{s,g} = \langle \sigma_{s,g} \rangle / \bar{\sigma}_{s,g}^{\infty} \quad ,$$

where the notation is conventional. In this representation the infinitely dilute elastic removal cross section was defined rigorously, so the location of resonances was reflected upon $\sigma_{er,g}^{\infty}$ contrary to the definition (6.1). However, the composition dependency of $\langle \sigma_{er} \rangle$ was represented through the self-shielding factor for the elastic scattering f_s which was computed by the interpolation from the tabulated values.

The effective cross sections have conventionally been obtained by using the weighting spectrum $1/(\sigma_t(u) + \sigma_0)$ based on the assumption of the constant collision density. As well-known, this assumption is not so accurate in the vicinity of strong resonances because the collision density largely deviates from the constancy assumed. Particularly, the effective elastic removal cross sections are very sensitive to the flux shape in the interval of ξ measured on the lower boundary of the group. We obtain here the weighting spectrum by solving numerically the slowing down equation with use of the recurrence formula developed by Kier.⁽⁴⁵⁾

In the higher energy region, fission spectrum and inelastic scattering contribute to the slowing down process as an additional contribution. This contribution was considered in the present work by adding a fixed source term. Moreover, anisotropy of elastic scattering becomes stronger in this energy region. Since this effect can not be accounted in the Kier's formula, the new recurrence formula derived in Chapter 3 was used to take account of the anisotropy up to the P_1 term of the Legendre expansion coefficients of the scattering angular distribution. The influence on the elastic removal cross sections was investigated for the oxygen resonance

region.

The improved self-shielding factors will be compared with the conventional ones or with the exact ones. In addition the improvement in the neutron spectra will also be shown for an iron assembly and a typical FBR.

6.2 Numerical Method

The slowing down equation can be written as follows for an infinite homogeneous medium in the energy region where the fission and inelastic sources are negligibly small:

$$\Sigma_t(u)\phi(u) = \sum_j \int_{u-\eta_j}^u \Sigma_s^j(u')\phi(u') \frac{e^{u'-u}}{(1-\alpha_j)} du' \quad , \quad (6.3)$$

where scattering is assumed to be isotropic in the center-of-mass system and j stands for nuclide.

The recurrence equation is similarly given as Eq.(3.9) by

$$\begin{aligned} \Sigma_{t,i}\phi_i &= \sum_j P_{1,j} \Sigma_{s,i-1}^j \phi_{i-1} + e^{-\Delta u} \{ S_{i-1} - \sum_j P_{L_j,j} \Sigma_{s,i-L_j-1}^j \phi_{i-L_j-1} \} \quad , \\ P_{\ell,j} &= \frac{1}{1-\alpha_j} e^{-(\ell-1)\Delta u} (1 - e^{-\Delta u}) \quad , \end{aligned} \quad (6.4)$$

where L_j is the maximum number of groups through which a neutron can be slowed down. S_{i-1} is the slowing down source into the $(i-1)$ group.

Using the flux thus obtained, we can calculate the elastic removal cross section and the self-shielding factor of a broad group ℓ by performing the following numerical integration

$$\langle \sigma_{er} \rangle_{\ell}^j = \frac{1}{1 - \alpha_j} \frac{\int_{u_{\ell} - \eta_j}^{u_{\ell}} \int_{u_{\ell}}^{u' + \eta} \sigma_s^j(u' \rightarrow u) \phi(u') du du'}{\int_{u_{\ell}}^{u_{\ell} - 1} \phi(u') du'}$$

$$f_{er, \ell}^j = \langle \sigma_{er} \rangle_{\ell}^j / \bar{\sigma}_{er, \ell}^{\infty, j} \quad (6.5)$$

The calculations have been performed by the RIFFH code⁽⁴⁶⁾ with a lethargy width of 0.0025 in the energy region from 200 to 1 keV, where is a typical resonance region of light and medium nuclides. The treatment with the strong anisotropic scattering of oxygen will be discussed later. The following assumptions were introduced for the numerical calculations.

- 1) The background nuclides have constant scattering cross sections in one group in order to preserve the concept of the self-shielding factor which depends only on the admixture cross section σ_o .
- 2) The absorption in the system is neglected.
- 3) The background nuclides are replaced, collectively, by a single imaginary nuclide.

The atomic mass \bar{A} of the imaginary nuclide is determined so as to reserve the average lethargy increment per collision, $\bar{\xi}$, of a mixture composing a typical FBR

$$\bar{\xi} = \frac{\sum_j \sum_{s,j} \xi_{s,j}}{\sum_j \sum_{s,j}} = 1 - \frac{(\bar{A} - 1)^2}{2\bar{A}} \lambda_n \frac{\bar{A} + 1}{\bar{A} - 1} \quad (6.6)$$

The \bar{A} determined in this manner is fixed for all the values of σ_o .

The accuracies of the assumptions were estimated for a sample core composition of oxygen, sodium, iron and ^{238}U . The atomic number densities are given in Table 6.1, which are similar to those of a prototype fast reactor. The assumption (1) may be supported by the fact that the strong

resonances of the nuclides under study, such as oxygen, sodium, iron, chromium and nickel, fortunately do not overlap with each other below 100 keV, so the interference effect is small between the resonances of different nuclides. However, even if the scattering cross section of one nuclide is constant, the elastic removal cross section depends on the composition via the flux distortion due to the resonances of other nuclides. The self-shielding factors for the removal cross sections are calculated for oxygen in 100 keV - 1 keV where the scattering cross section is constant, and the results are shown in Table 6.2. Though they are to be unity when the resonances of another nuclides are not taken into account, they become 0.75 at the group including the 28 keV iron resonance, and 0.64 or 1.34 at the two groups near the 2.85 keV sodium resonance. However the macroscopic removal cross sections of the medium do not get a serious error because in the resonance energy region the contributions of the resonance nuclides are very large compared with those of nuclides with constant cross sections.

The macroscopic removal cross sections obtained from the present revised method are compared in Table 6.3 with the exact values and with those from the conventional method using Eq.(6.2), for the energy region including the 28 keV iron resonance and the 2.85 keV sodium resonance. The maximum difference of the present value from the exact one is still 17 percents, but the present method is significantly improved in comparison with the conventional method.

Though the absorption cross sections of heavy elements may affect the flux gradient in an energy group, the elastic removal cross sections of light and medium nuclides were affected by only a few percents above 1 keV in our calculations when they were neglected (assumption 2). However much effects of the neglect of the absorption may appear in the

lower energy region (below 1 keV), where the resonance absorption is stronger.

When the effective group-cross section is defined in the concept of the self-shielding factors, its dependence on the masses of background nuclides is assumed to be small. The validity of this assumption was estimated for iron as shown in Table 6.4. In this case, Eq.(6.6) gives $\bar{A} = 33$. The results obtained by using the number-density-weighted atomic mass ($\bar{A} = 23$) are also given in this table. The differences of the values based on the definition (6.6) from those for the exact mass are smaller than 0.05 except the energy range 27.8 - 21.5 keV. The definition (6.6) seems superior to using the number-density-weighted \bar{A} as shown in the table. It can, therefore, be concluded that the assumption (3) based on the definition (6.6) is reasonable.

For oxygen, the important resonances are located in 400 keV ~ a few MeV region. In this energy region, some assumptions made previously become inadequate, that is, the fission and the inelastic scattering considerably contribute to the sources. Furthermore, the anisotropy of the elastic scattering is pronounced. Therefore some modifications are necessary to the slowing down equations. In this study the inelastic source was not explicitly treated but included in the fission source term and added in the right hand side of Eq.(6.4). However, the effect of this source on the elastic removal cross sections was small for the typical composition of FBR, since its distribution was fairly smooth in the group.

In the following, the anisotropic effect was investigated by comparing the case for the isotropic scattering with that taking into account up to the P_1 term of the Legendre expansion. The weighting flux was calculated with use of the ESELEM 5 code.

The effective elastic removal cross sections and self-shielding factors

of oxygen obtained by such calculations are compared in Table 6.5 in the energy range 6.5 MeV ~ 200 keV for $\sigma_0 = 0$. The effective cross sections are significantly different from each other, that is, amount to about 30 % below 0.63 MeV. On the other hand, the differences of the self-shielding factors are only 2 % at the maximum. It can be said that the self-shielding factors are hardly affected by the anisotropic effect, though the infinite dilute cross sections are considerably different. As a result the self-shielding factors for oxygen were also calculated by using Eq.(6.4) ~ (6.6) for all the values of σ_0 .

6.3 Comparison with Conventional Set

In the light of the studies made in the previous section, we have prepared the table of self-shielding factors for oxygen in the energy range, 6.5 MeV ~ 100 keV, and for sodium, aluminium, chromium, iron and nickel in the energy range, 200 keV - 1 keV, and revised the JAERI Fast set version 2 with 70 groups and 25 groups structures. These energy ranges include the important resonances of these nuclides. The present result for the self-shielding factor of sodium is compared with the old values in Fig.6.1 based on the conventional method and with the exact values which was obtained by the RIFFH code without the assumptions (1) ~ (3). The figure shows the σ_0 dependence of the self-shielding factors for the group numbers 22, 23 and 34 in the 70 groups which include large resonances. The exact values are shown for the σ_0 value corresponding to the core composition of a proto-type FBR presented in Table 6.1. It can be seen that the self-shielding factors are remarkably improved compared with the old ones in the vicinity of resonances. Since these self-shielding factors vary smoothly with the values of σ_0 , the conventional interpolation

method⁽³⁴⁾ can be easily applied to obtain the effective broad-group cross sections, with a slight modification.

With the use of the revised version, the neutron spectrum is calculated and compared with those from the old version and the fine group calculations. Figure 6.2 shows the neutron spectrum in the infinite medium of iron, where the fine group calculation has been performed by using the ESELEM 5 code with the group width of 0.0084 in lethargy. The neutron spectra are normalized at the energy range, 77.3 ~ 100 keV. The errors of removal cross sections appear sensitively in the neutron spectrum. The present version shows a very good agreement with the fine spectrum. On the other hand, the old version gives lower values than the fine spectrum, especially below 21.5 keV constantly underestimates it. Since its elastic removal cross section is fairly small compared to the present version at the energy range, 21.5 ~ 27.8 keV, the difference of slowing down source at this energy group propagates to the lower energy groups.

The fundamental mode neutron fluxes in the core of a prototype FBR are also compared in Fig.6.3, where the same buckling values were used for three cases. The present set considerably decreases the large discrepancy between the results from the old version and the fine spectrum calculation at the sodium, iron and oxygen resonances.

Some neutronics of a proto-type FBR have been calculated and compared in Table 6.6, where the results by the conventional set, the revised set and the fine spectrum method are presented. The effective multiplication factor, Doppler effect and sodium-void reactivity have slightly approached to the values by the fine spectrum method when the present set are used. The central reactivity worths for ^{238}U and iron change more than ten percents from the conventional set though the value of ^{238}U is not

necessarily improved. It will be difficult to conclude that the revised set becomes better or worse compared with the old set, at this stage. One of the causes of the discrepancies between the results obtained from the present method and the fine group calculation can be attributed to the mutual effect between the resonances of other nuclides. This discrepancy will become smaller if the removal cross sections of other nuclides are properly obtained at the resonances. Especially, the interference effects between oxygen and sodium seems to be very important in the energy range, 400 keV ~ 2 MeV and about at 3 keV. The further study will be required to introduce the interference effect between strong scattering resonances of different nuclide.

Table 6.1 Sample core composition and background cross sections

Isotope	Atomic density ($\times 10^{-24}$)	Scattering cross section (b)
O	0.01402	3.7
Na	0.00877	3.1
Fe	0.02094	11.4
^{238}U	0.00701	10.6

Table 6.2 Self-shielding factor of elastic removal cross section for oxygen

Energy range (keV)	f_r
46.5 - 36.0	0.961
36.0 - 27.8	0.746
27.8 - 21.5	1.076
21.5 - 16.6	0.979
16.6 - 12.9	0.984
12.9 - 10.0	0.974
10.0 - 7.73	0.851
7.73 - 5.98	1.018
5.98 - 4.65	0.958
4.65 - 3.60	0.888
3.60 - 2.78	0.637
2.78 - 2.15	1.338
2.15 - 1.66	1.067

The composition is given in Table 6.1.

Table 6.3 Comparison of macroscopic elastic removal cross section (cm^{-1})

Energy range (keV)	Exact Σ_{er}^E	Conventional		Revised	
		Σ_{er}^C	$(\Sigma_{er}^C / \Sigma_{er}^E)$	Σ_{er}^R	$(\Sigma_{er}^R / \Sigma_{er}^E)$
46.5 - 36.0	0.05372	0.05764	(1.07)	0.05600	(1.04)
36.0 - 27.8	0.0925	0.1678	(1.81)	0.1034	(1.12)
4.65 - 3.60	0.1058	0.1269	(1.20)	0.1191	(1.13)
3.60 - 2.78	0.3352	0.5485	(1.64)	0.3924	(1.17)
2.78 - 2.15	0.2248	0.1230	(0.55)	0.1950	(0.87)

Table 6.4 Comparison of self-shielding factor of iron obtained from various background masses

Energy range (keV)	Exact calc.	$\bar{A} = 33$	$\bar{A} = 23$
77.3 - 59.8	0.975	1.005	1.014
59.8 - 46.5	1.068	1.033	1.038
46.5 - 36.0	0.927	0.931	0.943
36.0 - 27.8	0.345	0.359	0.387
27.8 - 21.5	0.978	1.137	1.104
21.5 - 16.6	0.965	0.969	0.978
16.6 - 12.9	0.973	0.973	0.980
1.29 - 10.0	0.942	0.946	0.956
10.0 - 7.73	0.628	0.645	0.684
7.73 - 5.98	0.958	1.008	0.981
5.98 - 4.65	0.953	0.981	0.971
4.65 - 3.60	1.064	1.035	1.052
3.60 - 2.78	0.980	0.984	0.986
2.78 - 2.15	0.946	0.946	0.960
2.15 - 1.66	0.944	0.950	0.954

Table 6.5 Anisotropic effect on elastic removal cross section of oxygen

Energy range (MeV)	$\langle \sigma_{er} \rangle_0$	$\langle \sigma_{er} \rangle_1$	f_{r0}^*	f_{r1}^{**}
6.5 ~ 5.1	0.7510	0.5989	0.980	0.985
5.1 ~ 4.0	0.8758	0.6403	0.983	0.988
4.0 ~ 3.1	1.3540	0.9862	1.005	1.014
3.1 ~ 2.5	0.6356	0.5377	1.000	0.995
2.5 ~ 1.9	0.7800	0.7810	0.917	0.921
1.9 ~ 1.4	0.9065	0.9420	1.014	1.002
1.4 ~ 1.1	1.649	1.526	1.006	1.011
1.1 ~ 0.8	1.294	1.308	1.082	1.105
0.8 ~ 0.63	1.540	1.464	0.973	0.979
0.63 ~ 0.5	1.999	1.581	0.948	0.965
0.5 ~ 0.4	5.423	3.783	0.920	0.932
0.4 ~ 0.31	1.860	2.341	1.036	1.020
0.31 ~ 0.25	1.889	2.306	1.018	1.016
0.25 ~ 0.2	1.821	2.115	1.003	1.007

$$* f_{r0} = \langle \sigma_{er} \rangle_0 / \sigma_{er,0}^{\infty}$$

$$** f_{r1} = \langle \sigma_{er} \rangle_1 / \sigma_{er,1}^{\infty}$$

Suffices 0 and 1 mean the P_0 component and the P_0 plus P_1 components of elastic scattering cross section, respectively.

The composition is given in Table 6.1.

Table 6.6 Comparison of multiplication factor, Doppler effect, sodium void reactivity and central reactivity worth in Prototype FBR

	Conventional set	Revised set	Fine spectrum method
k_{eff}	1.0257	1.0242	1.0211
Doppler effect of I/C	-5.11-3*	-4.93-3	-4.21-3
Sodium void reactivity of I/C	1.29-2	1.32-2	1.50-2
Central reactivity worth			
^{239}Pu	5.22-4	5.12-4	5.24-4
^{238}U	-3.43-5	-3.08-5	-3.27-5
Fe	-3.21-6	-3.55-6	-3.46-6
Na	-2.70-6	-2.91-6	-2.79-6

* Read as $-5.11 \times 10^{-3} \Delta k/k$.

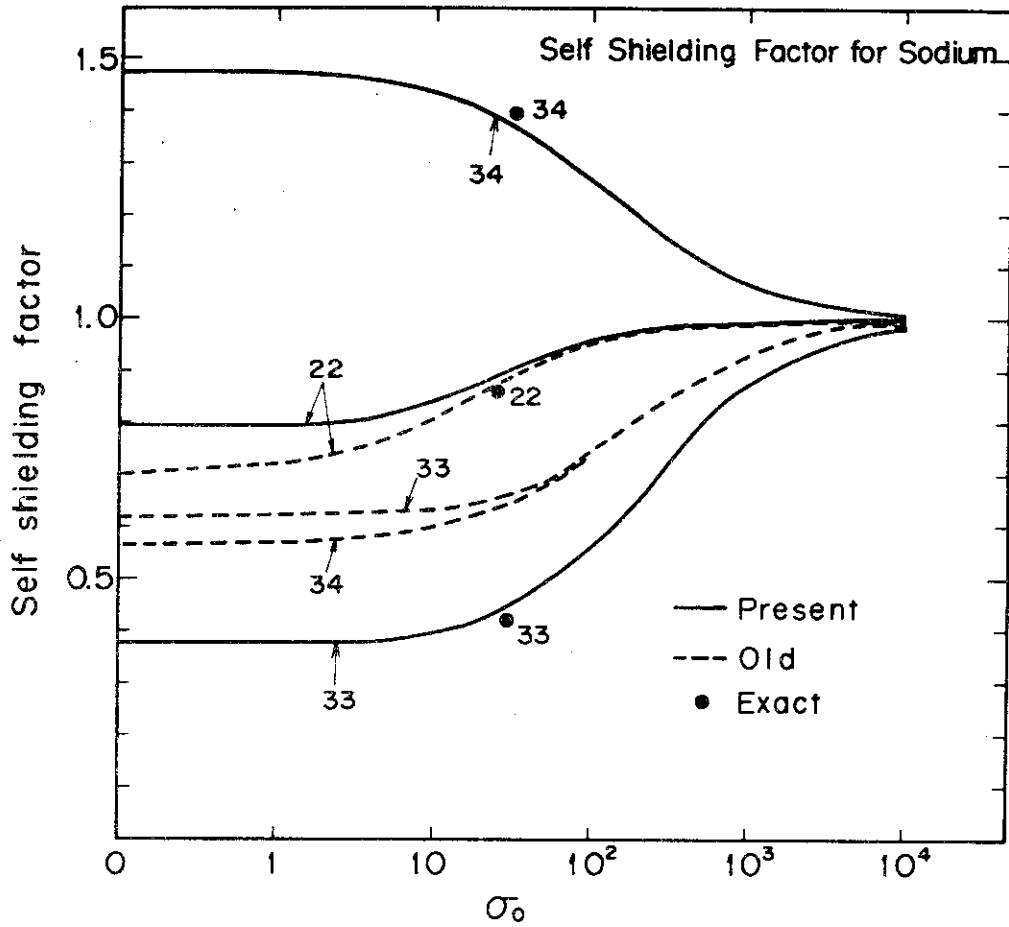


Fig.6.1 Self-shielding factor for sodium in 22, 23, 33 and 34 groups

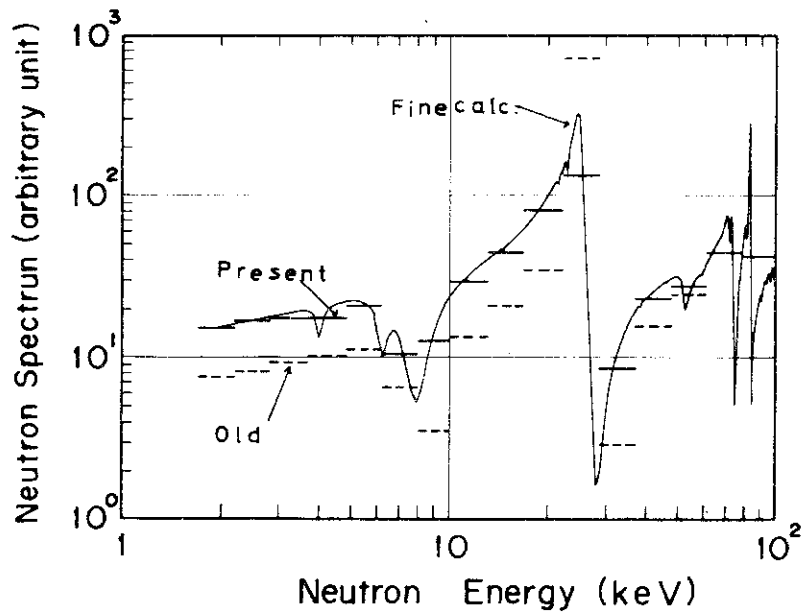


Fig.6.2 Comparison of neutron spectrum in iron

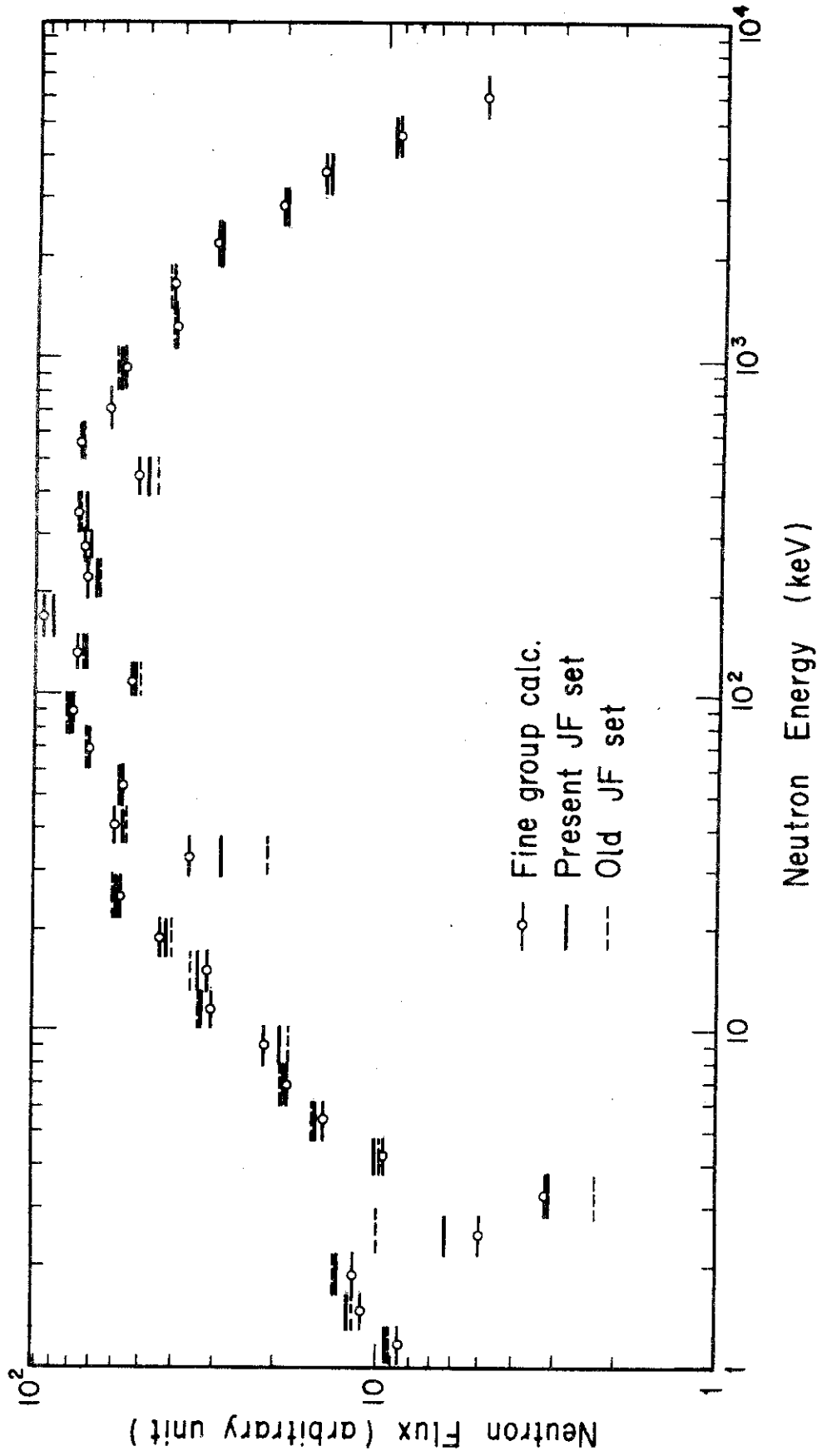


Fig.6.3 Comparison of fundamental mode neutron flux in core of FBR

7. Summary and Conclusions

The main purposes of the present work are to develop numerical methods to analyse accurately the neutronics parameters of fast neutron facilities with heterogeneous arrangements of cells, and to apply these methods for the analysis of the experiments for the sodium void reactivity. At first, the analysis has been made by using the broad group constants set, JAERI Fast set, and by using the SLAROM code newly developed to perform the heterogeneity calculations. In addition, the fine group spectrum and multi-group cross section calculation code, ESELEM 5, has been developed to investigate the adequacy of the broad group constant method and also to make detailed analysis. The sodium void reactivity worths have been calculated on the basis of the first order and the exact perturbation theories by using the CIPER code.

The main results obtained in each Chapter are summarized as follows. In Chapter 2, the solution method for the multi-group integral transport equations has been derived on the basis of the collision probability method. The heterogeneity effect on resonance shielding factors is taken into account based on the rational approximation in which the Dancoff factor is defined for a multi-region cell. The critical buckling value can be searched iteratively to obtain the fundamental mode flux by treating the leakage from a cell as a pseudo-absorption term. In addition, the SLAROM code can obtain the anisotropic diffusion coefficient with use of the directional collision probability. In this code, some devices have been incorporated to decrease significantly intermediate hand works of users.

In Chapter 3, the fine group spectrum and multi-group cross section calculation method has been developed.

In this method, the heterogeneity effect can be taken into account explicitly in the stage of a fine group structure. The main characteristics of the method adopted in ESELEM 5 are as follows: 1) Heterogeneous flux distribution is obtained by the collision probability method for the fine group. 2) The slowing down sources due to elastic scatterings can be calculated by using the recurrence formula which can take account of the anisotropy up to the P_1 component of the Legendre coefficients. 3) The sources from inelastic scatterings and $(n, 2n)$ reactions can be obtained also by using the recurrence relations, so the computation time and the computer core storage are significantly saved. 4) The transport cross section is defined by the P_1 weighting. 5) the heterogeneity effect on resonance shielding factors is considered by the consistent method used in SLAROM.

The data library has been produced from the JFS-V2 nuclear data library. The PRESM code has been developed to produce the library of ESELEM 5 from the ENDF/A or /B type files.

In Chapter 4, the sodium void reactivity worths and related neutronics parameters have been extensively calculated and compared with the experiments performed in FCA V-1, MZA, MZB, ZPPR-2 and ZPPR-3 assemblies. Through the analysis of the sodium void worths measured in FCA V-1 assembly, it has been seen that the heterogeneity effect and the neutron streaming effect are very significant and by taking into account them the calculations can predict satisfactorily the channel- and the large zone-voided cases ($C/E = 0.92 \pm 0.04$). The spatial heterogeneity effect shifts the sodium void worths to the negative side by 10 ~ 20 percents for the central void case.

The sodium void worths measured at the central regions of MZA have been calculated within the experimental uncertainties except for the

element voided case. The JFS-V2 gives slightly more negative values than the measurements throughout the core. The sodium void worths measured in MZB have been calculated by using JFS-V1, -1R, -N and -V2 sets for the central regions in the plate and pin configurations. The new evaluation of sodium cross sections has resulted in the revision of JFS-1R set. Through a comparison of the results by each version, it has been found that JFS-V2 gives the best agreement with the measurements throughout all the voided locations. The C/E values at the center are 0.98 for the plate and 1.03 for the pin environments. The deviations of the specific worths are almost constant for all the cases. The other versions has considerably under-predicted the void worths. The corrections due to the neutron streaming effect are positive and increase with approaching to the core boundary for both the assemblies. They amount to several times of the uncertainties of experiments. It has been shown however, that the streaming effect is not so significant for the pin cell compared with the plate cell.

In ZPPR-2, the sample worth distribution of sodium has been calculated by FOP method in xyz geometry. The calculated values are consistently more negative by 10 ~ 20 percents than the measurements in the core but in a good agreement with them in the blanket regions. The sodium void worths measured for the central regions with 1 ~ 93 voided drawers have been calculated in rz geometry. The C/E values are 1.10 ~ 1.20 and the deviations of the specific worths are $\sim 6.0 \times 10^{-6} \Delta k/k$ for the regions voided over ± 30.5 cm. These discrepancies are consistent with the results for the sample worth distribution. Since ZPPR-3 has a complex configuration with many CRs and CRPs, the calculations have been made for the three-dimensional model. It has been seen that the rz model is inadequate to treat the CRs and CRPs at the off-central

positions. The calculations predict well the sample worth distribution of sodium in the inner core but slightly underpredict it in the outer core. The C/E values of the sodium void worths for each voiding step are 0.8 ~ 0.9 in the inner core, and those for the cumulative voiding worths are 0.84 ~ 0.93 in the inner core and 0.74 ~ 0.86 in the outer core. The deviations of the specific worths are constantly about $-4.0 \times 10^{-6} \Delta k/k$ for all the cumulative voiding cases. The influences of CR and CRP on the sodium void worths have been investigated in detail for the inner and outer rings of CRs and CRPs. They may cause the change of the sodium void worth by several tens of percents at their neighbouring fuel regions. It has been found further that CR has a large positive sodium void worth.

The sodium void worth distribution has been calculated for a real proto-type fast breeder reactor. The calculations have been made with use of JFS-1R and JFS-V2. The maximum void worth is 1 % $\Delta k/k$ (~3.4 dollars) which is attained for the void region composed of the regions of 0 ~ 31 cm in the inner and 0 ~ 15.5 cm in the outer cores. The JFS-1R gives a smaller reactivity by 12 percents than JFS-V2, in which the difference arises mainly from the scattering components.

Through the analyses of the sodium void experiments, it has been concluded that JFS-V2 gives a better agreement with the measured values than any other versions, so the revision work on the JAERI Fast set has been successfully proceeded.

In Chapter 5, the fine group method has been used to examine the adequacy of the conventional broad group method. The multi-group cross sections have been produced by ESELEM 5 for the normal and voided cells. The sodium void worths have been compared for MZA and ZPPR-2. The fine group method gives more positive worths by about ten percents for MZA

and by about 20 percents for ZPPR-2 than the broad group method. The perturbation calculations indicate that the fine group method gives larger scattering components by 12 ~ 15 percents and smaller leakage components by 6 ~ 8 percents than the broad group method. It is emphasized that these discrepancies are consistent between both the assemblies. In ZPPR-2, however, the fine group method overpredicts still more than the broad group method. To examine the adequacy of the fine group calculations and the cross sections, the sample worth distribution of sodium, central reactivity worth, neutron spectrum have been calculated. The sample worth distribution shows a consistent result with the large scale sodium void worths. The results for the central reactivity worths of ^{235}U , ^{238}U , ^{239}Pu , C and Na indicate that the fission cross section of ^{238}U should be re-evaluated and the spectrum hardening caused by the sodium removal would be over-predicted. The neutron spectrum at the core center agrees fairly well between the measurement and the calculations except for the fact that the broad group method over-predicts it below the 2.85 keV sodium resonance. As a result, we can say that the broad group method can predict the sodium void reactivity worth with a high confidence and their results can be easily corrected for the fine group effect.

Chapter 6 has been devoted to improve the accuracy of elastic removal cross sections without changing the conventional concept of group constants. The self-shielding factors for elastic removal cross sections have been obtained and tabulated as a function of σ_0 . It has been shown moreover that the anisotropy of elastic scattering hardly influences the self-shielding factors although they are significant to the elastic removal cross sections. The neutron spectrum obtained by the revised set shows a better agreement with the fine spectrum calculations

than the conventional set. It is expect to take account of the mutual interference effect between different nuclei in future works.

Appendix 1. SLAROM Code

The SLAROM code⁽³⁰⁾ has been developed to analyse neutronics in fast facilities consisting of heterogeneous cells. The code was programmed to decrease intermediate handworks in the course of analysis. The calculation starts with the broad group constant set and geometrical informations. At present, the JAERI Fast set version 1 and version 2 are prepared as a standard library. The effective cross sections for each region in a unit cell are obtained with use of self-shielding factors as used in EXPANDA-4.⁽³⁴⁾ To take account of the heterogeneity effect on resonance self-shielding, some subroutines have been extended. The subroutines to calculate collision probability, to solve integral transport equation and to edit cell averaged cross sections are substantially based on the programmes used in the LAMP code⁽³²⁾ developed by Tsuchihashi. These subroutines have been modified to take account of the leakage from the cell in the form of the pseudo-absorption. The function of buckling search is also provided.

The I/O of SLAROM is devised to decrease a trouble of user. The free format input is quite helpful to decrease input errors. The cell averaged cross sections obtained are saved in PDS file and can easily be called later by identifying their member names. Some parts of the subroutines, RWPDSF and PDSERR are written in the assembler language of FACOM 230/75. These I/O subroutines have been developed at JAERI computing center.⁽⁶³⁾⁽⁶⁴⁾

The contents of the output are listed in the following.

1) PREP routine

Title, input data list, effective cross sections for homogeneous media and their member name in PDS file.

2) PATH routine

Input data list, volumes of regions, collision probability.

3) PIJF routine

Input data list, effective cross sections of regions, monitor print of buckling search and outer iteration, converged eigenvalue and its relative error, neutron fluxes in regions and in groups, cell averaged neutron fluxes, normal diffusion coefficients, effective cross sections for each reaction type.

4) EDIT routine

Control data list, anisotropic diffusion coefficients, cell averaged effective cross sections and their member name in PDS file.

5) EIND routine

Input data list, macroscopic cross sections in regions, converged eigenvalue, source distributions, point-wise and/or integrated neutron fluxes, collapsed cross sections, results of perturbation calculation.

The SLAROM consists of about 9000 cards subdivided into 63 subroutines. The programme utilizes eight segments overlay structure. The recommended overlay structure is shown in Fig.A.1.

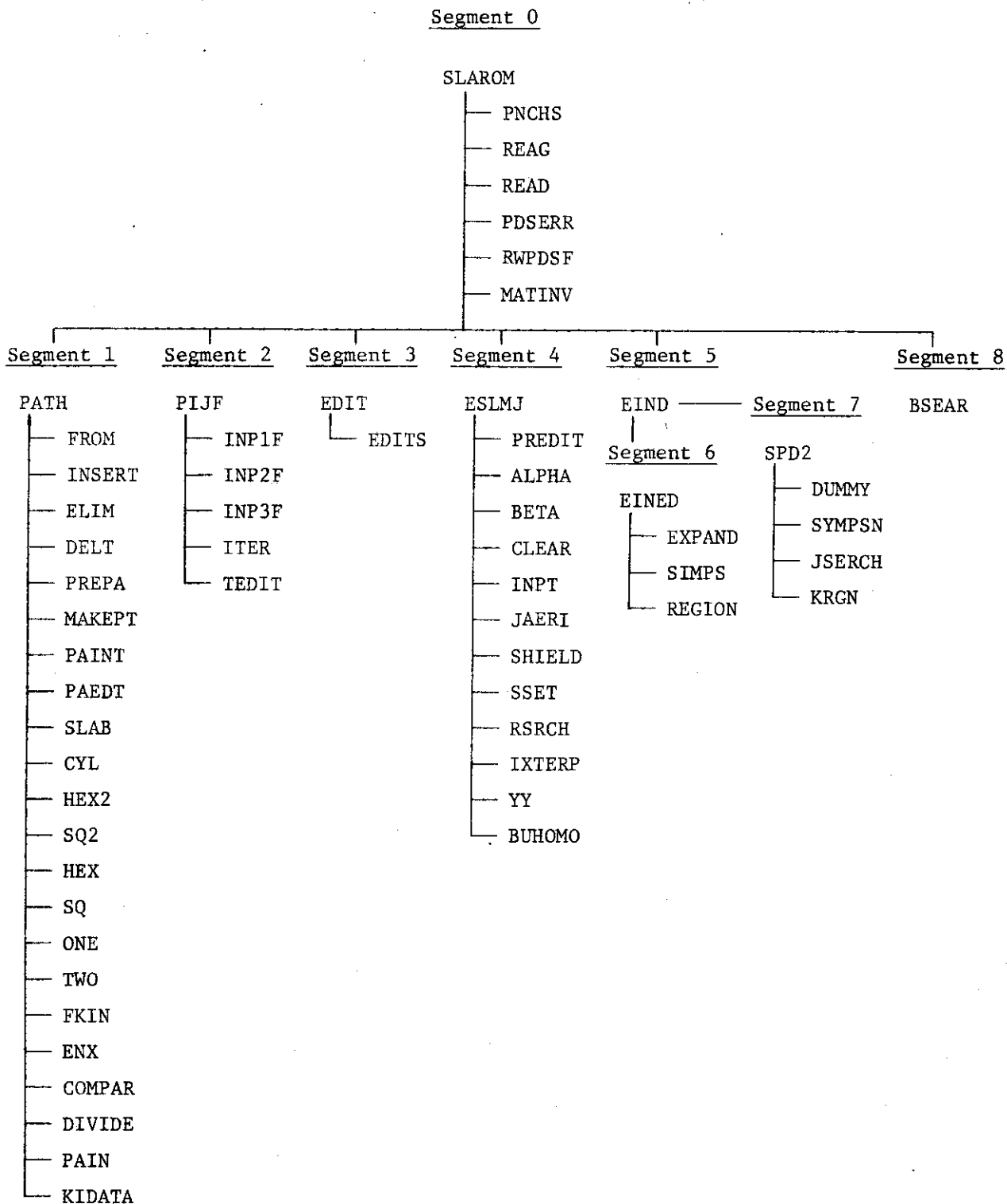


Fig.A.1 Overlay structure of SLAROM

Appendix 2. ESELEM 5 Code

1. Calculation Flow

The brief calculation flow of ESELEM 5 is shown in Fig.A.2. The first locations of variable arrays are defined in the subroutine SSET which consists of four entries. The locations are determined at four stages of the calculation in order to save core memories. For the case where the resonance shielding effect of heavy elements is not necessary to take into consideration, the routine to calculate the shielding factors is bypassed. If it is required, the JAERI Fast set with 70 group structure is read in. The library data consist of three files, the JAERI Fast set, the fine group cross section data and the Legendre coefficients for anisotropic elastic scattering. The second file is read at every fine group from the temporary file. The third file is stored in the fast core memory and used in the calculation of elastic slowing down source.

In the ESELEM 4 code, the broad group treatment was adopted above 2 MeV in order to save the computation time. However, ESELEM 5 uses the fine group structure throughout all the groups. By this revision the accuracy is improved and the preparation of broad group library can be suppressed. The subroutines to compute the averaged ν value and fission spectrum are called at every fine group energy point. Then, the slowing down sources from upper groups are computed on the basis of the recurrence relations. The slowing down sources due to inelastic continuum levels and $(n, 2n)$ reactions can be stored either in the core memory or in a temporary disk file. In the latter case, the direct access I/O is used. Then, the required core memory is significantly saved but the computation time is increased about a few tens of percents.

The initial fission source distribution can be given by input, and otherwise the flat source distribution is internally set. From a viewpoint of computation economy, it will be helpful to use the SLAROM code to obtain the critical buckling value and the fission source distribution to be used as the guess. Usually one iteration is sufficient to obtain the converged eigenvalue if such a guess is input.

After each outer iteration, the multiplication factor is calculated and the convergence test is performed. If the outer iteration is converged, the edit routine is called from the main program. The plotter routine can be used to draw the neutron spectrum.

2. Description of ESELEM 5

The ESELEM 5 code consists of eight overlay segments with 40 sub-routines. The structure of overlay is shown in Fig.A.3. The ESELEM 5 is written in FORTRAN IV for using on CDC 6600 and FACOM 230/75 computers with H level-compiler. Since important variables are stored in the block with an adjustable size, the required core memory depends on the problem type to be solved. It is printed in the subroutine SSET after setting the locations of variables. If the slowing down sources due to the inelastic continuum levels and the (n, 2n) reactions are kept in the core memory, the following core storage in words are required in the subroutine ECSR:

$$M = NMS * 1450 * JJB ,$$

where NMS and JJB stand respectively for the numbers of meshes and elements.

3. Library Preparation Code : PRESM

The PRESM code produces the data library for the ESELEM 5 code from the ENDF/A⁽⁶⁵⁾ or ENDF/B⁽⁶⁶⁾ format nuclear data file. The file is fed in the BCD mode. The ENDF/B type file is converted at first to the ENDF/A format by using the CORBA code.⁽⁶⁷⁾ All the cross sections should be given in the file 3 type of the point-wise data. When a nuclide is assigned in input, PRESM reads its elastic and inelastic scattering, fission, capture and (n, 2n) cross sections. The capture cross section is produced as the sum of (n, γ), (n, p) and (n, α) cross sections. At first, the point-wise cross sections are produced at the same energy points as for the elastic scattering cross section. If such energy points are not given in other reactions, the cross sections are interpolated to those energy points. Then, the fine group data are produced by averaging them with 1/E spectrum over the lethargy width of 0.0084. The maximum number of inelastic scattering levels is limited to 25 discrete levels and one continuum level for each nuclide. The Legendre coefficients of anisotropic elastic scattering are prepared up to P_1 term in another file.

The structure of PRESM is shown in Fig.A.4. The present library was produced from the JAERI Fast set version 2 data file. The nuclide and the energy region of available resonance self-shielding factors are presented in Table A.1. In the resonance energy region of heavy elements, the standard JAERI fast set library should be loaded if the option to use the self-shielding factors is selected.

Table A.1 Nuclide in JAERI Fast version 2 library

Sequence	Nuclide	Fission spectrum	Upper energy of resonance region
1	^{10}B		
2	^{11}B		
3	C		
4	O		
5	Na		
6	Al		
7	Cr		
8	Mn		
9	Fe		
10	Ni		
11	Mo		
12	^{235}U	yes	10 keV
13	^{238}U		46.5 keV
14	^{239}Pu	yes	21.5 keV
15	^{240}Pu		10 keV
16	^{241}Pu		
17	^{242}Pu		

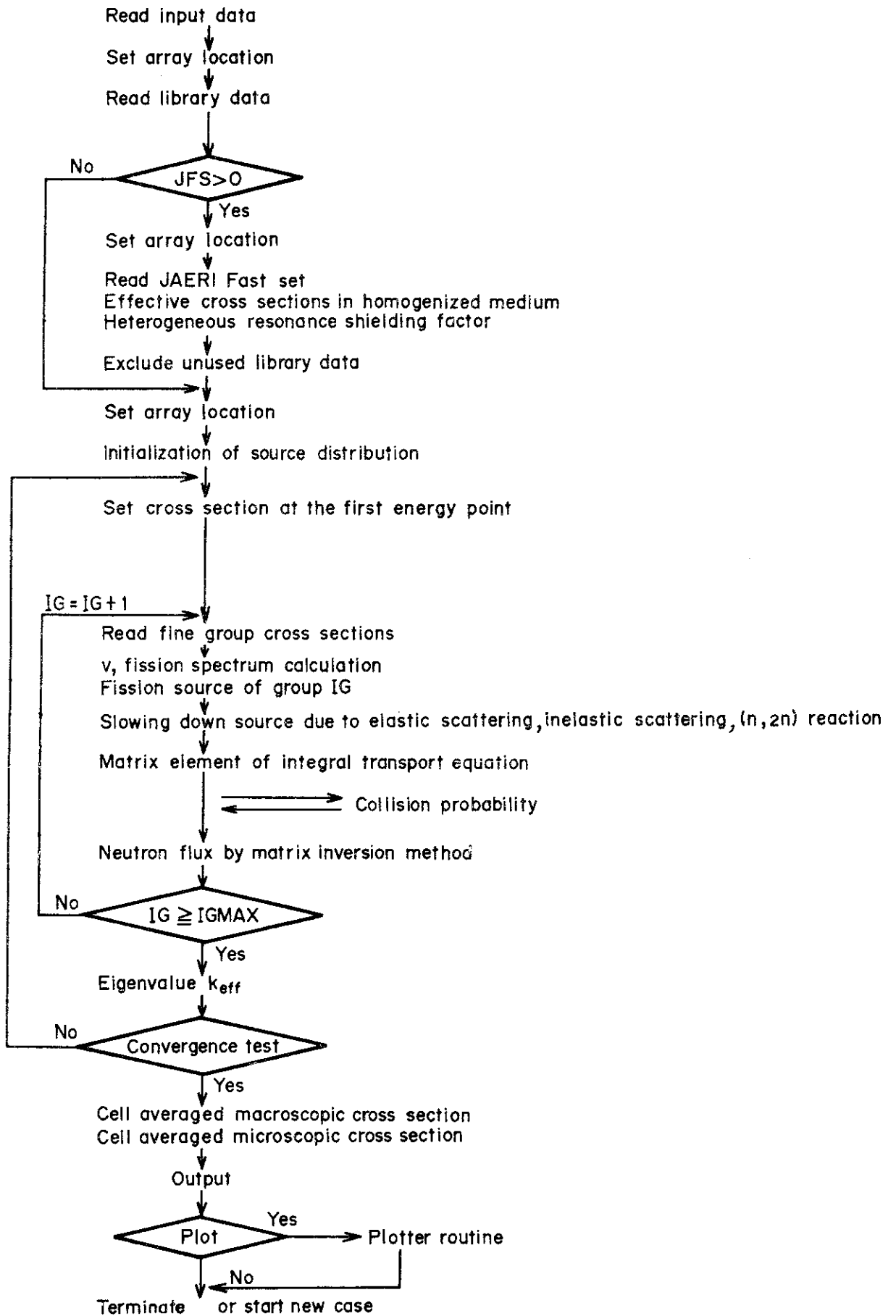


Fig. A.2 Calculation flow of ESELEM 5

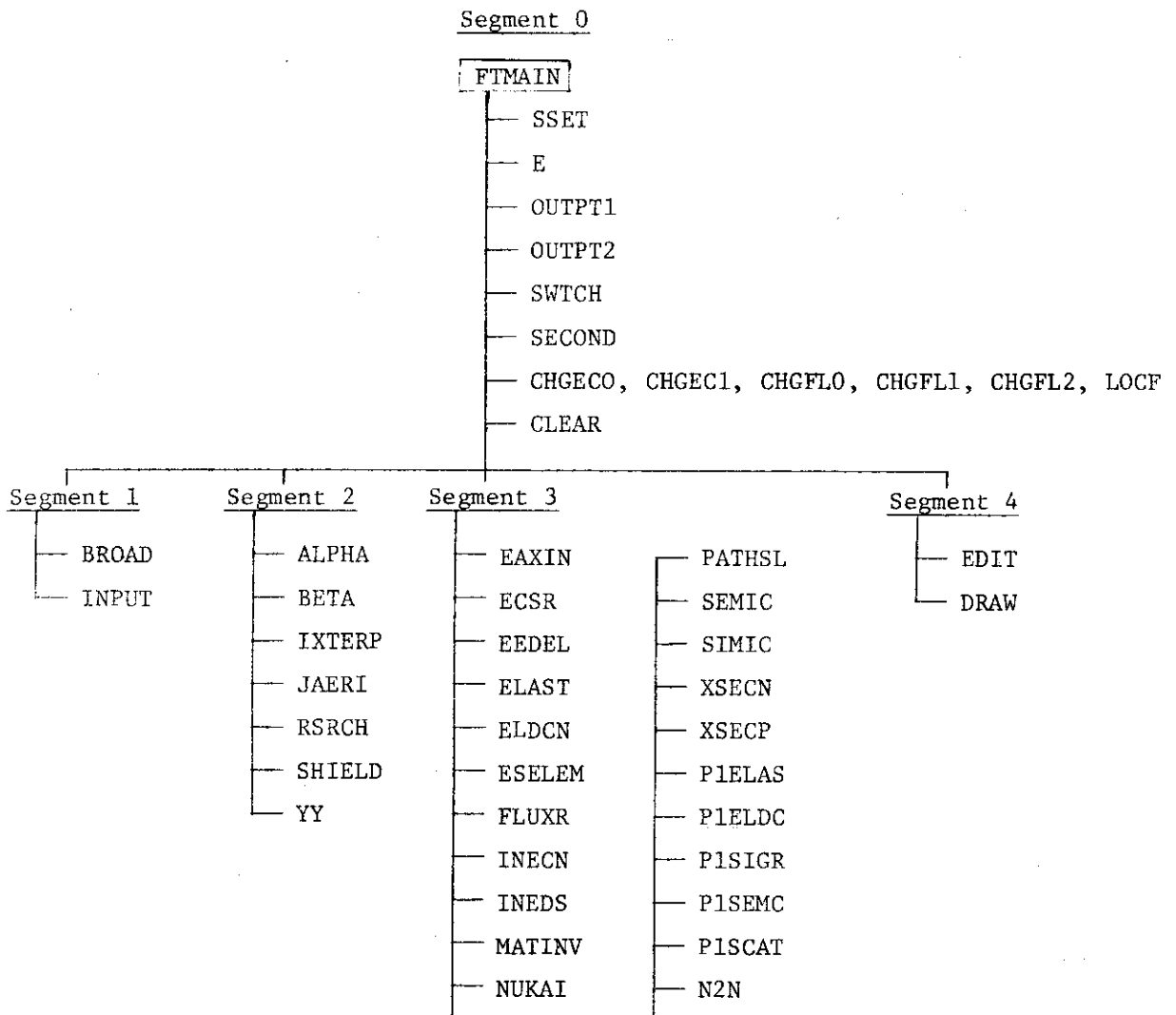


Fig.A.3 Overlay structure of ESELEM 5

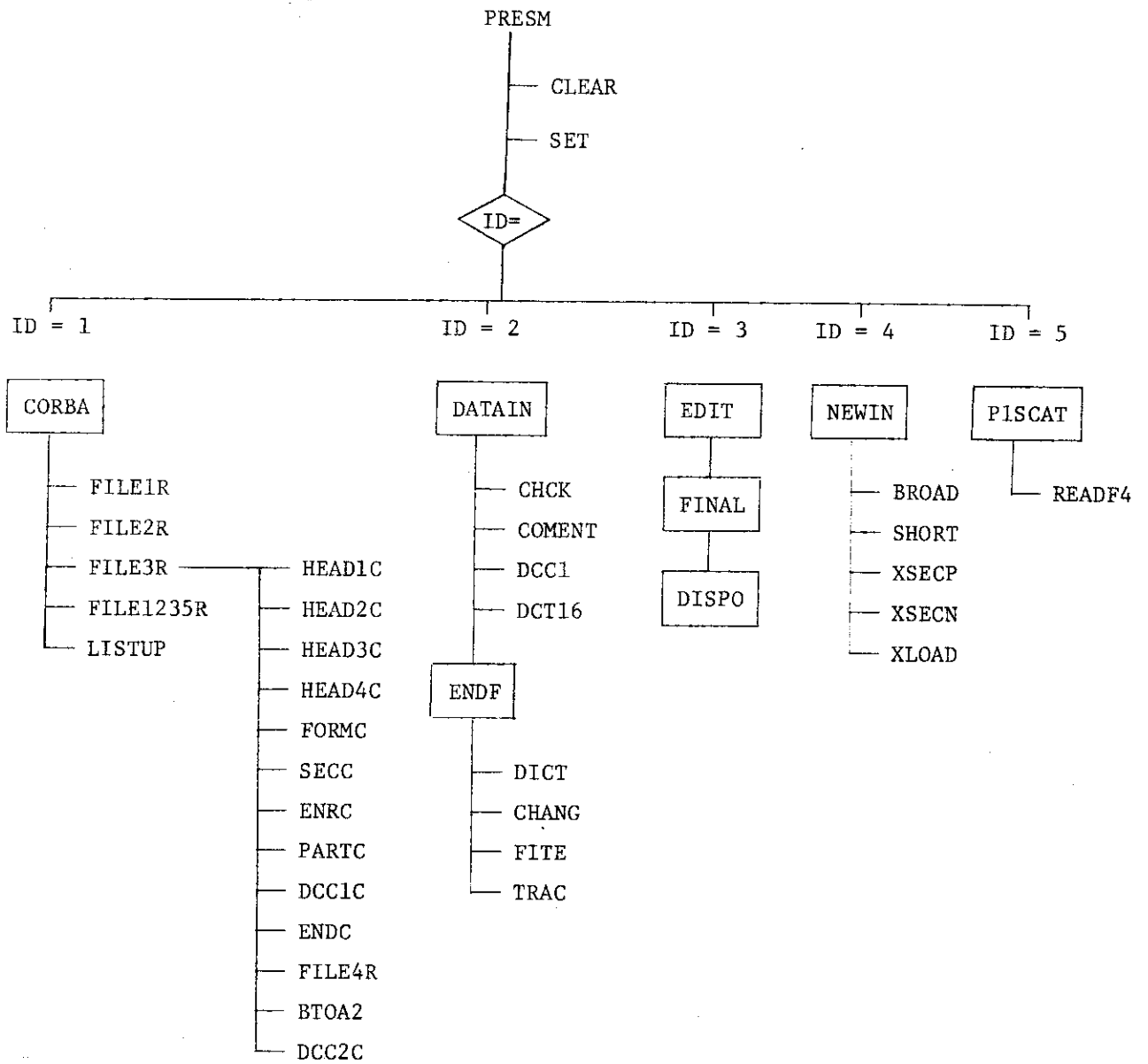


Fig.A.4 Structure of PRESM

ACKNOWLEDGMENTS

I would like to thank Dr. Takumi Asaoka for his encouragement and useful advices. I am indebted to Drs. Satoru Katsuragi and Yukio Ishiguro for their most helpful discussions during the course of this work.

I wish to express my grateful thanks to Professor Jiro Wakabayashi for his valuable comments and criticism. Thanks are also due to Professor Hiroshi Nishihara for his continuous encouragement.

I wish to acknowledge Mr. Hideki Takano, Mr. Akira Hasegawa and Dr. Tomoo Suzuki for their valuable discussions. I also thank to Mr. Yukio Tokuno for his assistance with computations.

REFERENCES

- 1) Nims J. B. and Zweifel P. F. : APDA-135, "Preliminary Report on Sodium Temperature Coefficients in Large Fast Reactors", (1959)
- 2) Ohta M. and Nishihara H. : J. Nucl. Sci. Technol. 2, 340 (1965)
- 3) Honeck H. C. : BNL-5826, "A Thermalization Transport Theory Code for Reactor Lattice Calculation", (1961)
- 4) Tsuchihashi K. : JAERI-1196, "CLUP77 A Fortran Program of Collision Probabilities for Square Clustered Assembly", (1971)
- 5) Storrer F. et al. : Nucl. Sci. Eng. 24, 153 (1966)
- 6) Benoist P., : CEA-R2278, "Théorie du Coefficient de Diffusion des Neutrons Dans un Réseau Comportant des Cavités", (1964)
- 7) Nakagawa M., Takano H. and Katsuragi S. : J. Nucl. Sci. Technol. 10, 419 (1973)
- 8) Nakagawa M. and Tokuno Y. : JAERI-M6722, "CIPER, A Two-and Three-Dimensional Perturbation Code Based on Diffusion Theory", (1976) (in Japanese)
- 9) Katsuragi S., Tone T. and Hasegawa A. : JAERI-1195, "JAERI Fast Reactor Group Constants Systems Part I", (1970)
- 10) Katsuragi S., Ishiguro Y., Takano H. and Nakagawa M. : JAERI-1199, *ibid* Part-II (1970)
- 11) MIMURA Y. et al. : Preprint 1971 Ann. Meeting At. Energy Soc. Japan, B29 (1971)
- 12) Inoue T. et al. : J. At. Energy Soc. Japan, 18, 554 (1976)
- 13) Cambell C. G. et al. : "Proc. Int. Symp. Physics of Fast Reactors, Tokyo", A14 (1973)
- 14) Zukeran A. et al. : J. At. Energy Soc. Japan, 18, 672 (1976)
- 15) Davey W. G. et al. : ANL-7961, "Rod and Plate Heterogeneity Studies in ZPPR-2", (1974)
- 16) Mcfarlane H. F. et al. : "Conf. on Advanced Reactor Physics Designe and Economics", Atlanta (1974)

- 17) Greebler P. and Pflasterer G. R. : "Doppler and Sodium Void Reactivity Effects in Fast Reactors", in Reactor Physics in the Resonance and Thermal Regions, Vol. II, M.I.T. Press, Cambridge (1966)
- 18) Hummel H. H. and Okrent D. : "Reactivity Coefficients in Large Fast Power Reactors", ANS (1970)
- 19) Pitterle T. A., Page E. M. and Yamamoto M. : APDA-216, "Analysis of Sodium Reactivity Measurements Vol. 1 and 2" (1968)
- 20) Toppel B. J., Rago A. L. and O'Shea D. M. : ANL-7318, "MC², A Code to Calculate Multi-group Cross Sections" (1967)
- 21) Stevenson J. M. et al. : "Proc. Int. Symp. Physics on Fast Reactors, Tokyo", A19 (1973)
- 22) Davey W. G. et al. : ANL-7962, "Sodium Voiding Studies in a Plutonium-Fueled Fast Assembly (ZPPR-2) of Demonstration Reactor Size, Composition and Geometry", (1974)
- 23) Tone T. : J. Nucl. Sci. Technol., 5, 538 (1968)
- 24) Stacey W. M. : Nucl. Sci. Eng., 47, 29 (1972)
- 25) Stacey W. M. : "Proc. Int. Symp. Physics on Fast Reactors, Tokyo", A31 (1973)
- 26) Macdougall J. : ibid, A32 (1973)
- 27) Katsuragi S., Ishiguro Y. and Katho H. : JAERI 1109, "Group Constants for a Fast Reactor and Sodium Void Effects", (1966)
- 28) Nakagawa M. and Zukeran A. : "An International Comparison Calculation of a Large Sodium Cooled Fast Breeder Reactor" to be published
- 29) Till C. E. : NEACRP-A-272 (1976)
- 30) Nakagawa M. and Tsuchihashi K. : JAERI-M 5916, "SLAROM, A Code for Calculation of Heterogeneous Core in Fast Reactors" (1974)
(in Japanese)

- 31) Nakagawa M. Katsuragi S. and Narita H. : JAERI 1245, "ESELEM4, A Code for Calculating Fine Neutron Spectrum and Multi-group Cross Sections in Plate Lattice" (1976)
- 32) Tsuchihashi K. : To be published in JAERI report
- 33) Honeck H. C. : Nucl. Sci. Eng. 8, 193 (1960)
- 34) Suzuki T. : JAERI-memo 3660, "EXPANDA-4, The One-Dimensional Diffusion Equation Code for Fast Reactors Using the JAERI-Fast Set", (1969) (in Japanese)
- 35) Ishiguro Y. : Nucl. Sci. Eng. 51, 441 (1973) and 55, 349 (1974)
- 36) Meneghetti D. : ANL-7320, 377 (1966)
- 37) Bell G. I. : LA-2322, "Theory of Effective Cross Sections" (1959)
- 38) Fowler T. B. et al. : ORNL-4078, "EXTERMINATOR-2 : A Fortran IV Code for Solving Multi-group Neutron Diffusion Equations in Two Dimensions" (1967)
- 39) Folwer T. B. and Vondy D. R. : ORNL-TM-2496, Rev.2 "Nuclear Reactor Core Analysis Code : CITATION" (1971)
- 40) Yiftah S., Okrent D. and Moldauer P. A. : "Fast Neutron Cross Sections", Pergamon Press, London (1960)
- 41) Abagian L. P. et al. : "Group Constants for Nuclear Reactor Calculations", Consultants Bureau, New York (1964)
- 42) Kikuchi Y. et al. : JAERI 1239, "EXPANDA-75, One Dimensional Diffusion Code for Multi-Region Plate Lattice Heterogeneous System", (1975)
- 43) Rago A. L. and Hummel H. H. : ANL-6805, "ELMOE, An IBM-704 Program Treating Elastic Scattering Resonance in Fast Reactors" (1964)
- 44) Kuroi H. and Tone T. : JAERI 1230, "Cross Section Data and Specifications of AGLI/0 for Fast Reactor Analysis" (1973)
- 45) Kier P. H. and Robba A. A. : ANL-7326, "RABBLE, A Program for Computation of Resonance Absorption in Multiregion Reactor Cells" (1967)

- 46) Nakagawa M. and Katsuragi S. : unpublished
- 47) Palmedo P. F. : BNL-15746, "Compilation of Fast Reactor Experiments, Vol.I, II" (1971)
- 48) Wardleworth D. and Ingram G. : "Proc. IAEA Conf. Fast Reactor Physics, Karlsruhe", Vol.II, 343 (1967)
- 49) Hasegawa A. et al. : JAERI-M4953, "A One-Dimensional Diffusion Code for Multi-groups Criticality and Perturbation Calculation with JAERI-Fast Set of 70-Group Structure : EXPANDA-70D" (1972) (in Japanese)
- 50) Iijima S. et al. : Preprint 1971 Fall Meeting At. Energy Soc. Japan, B11 (1971)
- 51) Takano H. et al. : JAERI 1255 "JAERI Fast Reactor Group Constants Set, Version II" (1978)
- 52) Takano H., Hasegawa A, and Katsuragi S. : "Proc. AESJ 1973 Topical Meeting on Fast Reactor Physics", 19 (1973) (in Japanese)
- 53) Moxon M. C. : AERE-R6074 (1969)
- 54) Norton S. and Story J. S. : AEEW-M802 "UKAEA Nuclear Data Library 1967" (1967)
- 55) Garber D. et al. : "ENDF-102 Data Formats and Procedures for the Evaluated Nuclear Data File ENDF", BNC-NCS-50496, National Neutron Cross Section Center (1975)
- 56) Parker K. : AWRE O-70/63 (1972)
- 57) Woll D. : KFK 880
- 58) Hibdon C. T. : Phys. Rev. 118, 514 (1960)
- 59) Amundson P. I et al. : CONF-72091, "Spatially Dependent Benchmark Parameters in the Initial Demonstration Plant Critical Assembly", 809 (1972)
- 60) Seki Y. et al. : Preprint 1975 Fall Meeting At. Energy Soc. Japan, B30, B31 (1975)
- 61) Tone T. and Nakagawa M. : J. Nucl. Sci. Technol. 6, 295 (1969)

- 62) Bohn E. M. : ANL-75-14, "The Central Worth Discrepancy in Three Fast Reactor Benchmark Critical Assemblies" (1975)
- 63) Asai K. and Tsuchihashi K. : JAERI-meno 4458, "A Subroutine Reading Data in Free Format" (1971) (in Japanese)
- 64) Asai K. : Private communication
- 65) Honeck H. C. : BNL-8381, "ENDF Evaluated Nuclear Data File Description and Specification" (1965)
- 66) Drake M. K. : BNL-50274 (T-601) (1970)
- 67) Shibuya K. and Katsuragi S. : unpublished